Continental Rift Dynamics Across the Scales – Numerical Modelling of Localisation Processes

---

Maximilian Jacob Enzo Amandus Richter
(geb. Döhmann)

Kumulative Dissertation
zur Erlangung des akademischen Grades
"doctor rerum naturalium"
(Dr. rer. nat.)
in der Wissenschaftsdisziplin Geophysik

eingereicht an der
Mathematisch-Naturwissenschaftlichen Fakultät
der Universität Potsdam

Potsdam, den 23.11.2021

Erstbetreuer: Prof. Dr. Stephan V. Sobolev
Zweitbetreuer: Priv. Doz. Dr. Sascha Brune
Mentor: Prof. Dr. Georg Dresen
Gutachter: Prof. Dr. Thibault Duretz

Published online on the
Publication Server of the University of Potsdam:
https://doi.org/10.25932/publishup-55060
https://nbn-resolving.org/urn:nbn:de:kobv:517-opus4-550606

Abstract

Localisation of deformation is a ubiquitous feature in continental rift dynamics and observed across drastically different time and length scales. This thesis comprises one experimental and two numerical modelling studies investigating strain localisation in (1) a ductile shear zone induced by a material heterogeneity and (2) in an active continental rift setting. The studies are related by the fact that the weakening mechanisms on the crystallographic and grain size scale enable bulk rock weakening, which fundamentally enables the formation of shear zones, continental rifts and hence plate tectonics.

Aiming to investigate the controlling mechanisms on initiation and evolution of a shear zone, the torsion experiments of the experimental study were conducted in a Patterson type apparatus with strong Carrara marble cylinders with a weak, planar Solnhofen limestone inclusion. Using state-of-the-art numerical modelling software, the torsion experiments were simulated to answer questions regarding localisation procedure like stress distribution or the impact of rheological weakening. 2D numerical models were also employed to integrate geophysical and geological data to explain characteristic tectonic evolution of the Southern and Central Kenya Rift. Key elements of the numerical tools are a randomized initial strain distribution and the usage of strain softening.

During the torsion experiments, deformation begins to localise at the limestone inclusion tips in a process zone, which propagates into the marble matrix with increasing deformation until a ductile shear zone is established. Minor indicators for coexisting brittle deformation are found close to the inclusion tip and presumed to slightly facilitate strain localisation besides the dominant ductile deformation processes. The 2D numerical model of the torsion experiment successfully predicts local stress concentration and strain rate amplification ahead of the inclusion in first order agreement with the experimental results. A simple linear parametrization of strain weaking enables high accuracy reproduction of phenomenological aspects of the observed weakening. The torsion experiments suggest that loading conditions do not affect strain localisation during high temperature deformation of multiphase material with high viscosity contrasts. A numerical simulation can provide a way of analysing the process zone evolution virtually and extend the examinable frame. Furthermore, the nested structure and anastomosing shape of an ultramylonite band was mimicked with an additional second softening step. Rheological weakening is necessary to establish a shear zone in a strong matrix around a weak inclusion and for ultramylonite formation.

Such strain weakening laws are also incorporated into the numerical models of the Southern and Central Kenya Rift that capture the characteristic tectonic evolution. A three-stage early rift evolution is suggested that starts with (1) the accommodation of strain by a single border fault and flexure of the hanging-wall crust, after which (2) faulting in the hanging-wall and the basin centre increases before (3) the early-stage

asymmetry is lost and basinward localisation of deformation occurs. Along-strike variability of rifts can be produced by modifying the initial random noise distribution.

In summary, the three studies address selected aspects of the broad range of mechanisms and processes that fundamentally enable the deformation of rock and govern the localisation patterns across the scales. In addition to the aforementioned results, the first and second manuscripts combined, demonstrate a procedure to find new or improve on existing numerical formulations for specific rheologies and their dynamic weakening. These formulations are essential in addressing rock deformation from the grain to the global scale. As within the third study of this thesis, where geodynamic controls on the evolution of a rift were examined and acquired by the integration of geological and geophysical data into a numerical model.

Zusammenfassung

Die Lokalisierung von Deformation ist ein allgegenwärtiges Merkmal in der Dynamik von Grabenbrüchen bzw. Riftzonen und wird über verschiedene Zeit- und Längenskalen beobachtet. Diese Arbeit umfasst eine experimentelle und zwei numerische Studien zur Untersuchung der Lokalisierung von Deformation in (1) einer durch eine Materialheterogenität induzierten duktilen Scherzone und (2) in einem aktiven Kontinentalgraben. Die Studien verbindet, dass die Schwächungsmechanismen auf der kristallographischen Skala und der Korngrößenskala eine Enthärtung eines Gesteinkörpers ermöglicht, was im Wesentlichen die Bildung von Scherzonen, Grabenbrüchen und damit Plattentektonik ermöglicht.

Um die Kontrollmechanismen für die Initiierung und Entwicklung einer Scherzone zu untersuchen, wurden die Torsionsexperimente der experimentellen Studie in einem Patterson-Gerät an starken Carrara-Marmorzylinder mit einer schwachen, planaren Solnhofen-Kalksteineinschluss durchgeführt. Mit modernster numerischer Modellierungssoftware wurden die Torsionsexperimente simuliert, um weitere Fragen zum Lokalisierungsablauf wie die Verteilung der Spannung oder den Einfluss rheologischer Schwächung zu beantworten. Numerische 2D-Modelle wurden auch verwendet, um geophysikalische und geologische Daten zu kombinieren, um die charakteristische tektonische Entwicklung des südlichen und zentralen Kenia-Rifts zu erklären. Schlüsselelemente der verwendeten numerischen Werkzeuge sind eine randomisierte Anfangsverteilung des Strain und der Einsatz von Strain basierter Enthärtung.

Während der Torsionsversuche lokalisiert die Deformation zunächst an den Kalksteineinschlussspitzen in einer Prozesszone, die sich mit zunehmender Deformation in die Marmormatrix ausbreitet bis sich eine duktile Scherzone einstellt. Neben den dominierenden duktilen Verformungsprozessen werden geringfügige Indikatoren für eine koexistierende spröde Verformung nahe der Einschlussspitzen gefunden und es wird angenommen, dass diese die Lokalisierung der Deformation geringfügig erleichtern. In erster Ordnung sagt das numerische 2D-Modell des Torsionsexperiments erfolgreich lokale Spannungskonzentration und Strainratenverstärkung vor der Inklusion in Übereinstimmung mit den experimentellen Ergebnissen vorher. Eine einfache lineare Parametrisierung der Enthärtung durch Strain ermöglicht eine genaue Reproduktion phänomenologischer Aspekte der beobachteten Schwächung. Die Torsionsexperimente legen nahe, dass die Randbedingungen die Lokalisierung des Strain während der Hochtemperaturverformung von Mehrphasenmaterial mit hohen Viskositätskontrasten nicht beeinflussen. Die numerische Simulation ermöglicht es, die Entwicklung der Prozesszone virtuell zu analysieren und den Untersuchungsrahmen zu erweitern. Darüber hinaus wurde die verschachtelte Struktur und anastomosierende Form eines Ultramylonitbandes mit einem zusätzlichen zweiten Enthärtungsschritt nachgeahmt. Die

rheologische Schwächung ist notwendig, um eine Scherzone in einer starken Matrix um einen schwachen Einschluss herum und für die Ultramylonitbildung zu etablieren.

Solche Schwächungsgesetze, die auf Strain basieren, fließen auch in die numerischen Modelle des südlichen und zentralen Kenia-Rifts ein, die die charakteristische tektonische Entwicklung erfassen. Es wird eine dreistufige frühe Riftentwicklung vorgeschlagen, die mit (1) der Anpassung von Spannungen durch eine einzelne Grenzstörung und Biegung der hangenden Kruste beginnt, wonach (2) die Verwerfung im Hangenden und im Beckenzentrum zunimmt, bevor (3) die Asymmetrie des Frühstadiums verloren geht und es zu einer beckenseitigen Deformationslokalisierung kommt. Die Variabilität von Rissen entlang des Rifts kann durch Modifizieren der anfänglichen zufälligen Rauschverteilung erzeugt werden.

Zusammenfassend befassen sich die drei Studien mit ausgewählten Aspekten der breiten Palette von Mechanismen und Prozessen, die die Deformation von Gestein grundlegend ermöglichen und die Lokalisierungsmuster über die Skalen bestimmen. Zusätzlich zu den oben genannten Ergebnissen demonstrieren das erste und zweite Manuskript in Kombination ein Verfahren, um neue oder bestehende numerische Formulierungen für spezifische Rheologien und deren dynamische Schwächung zu finden oder zu verbessern. Diese Formulierungen sind essenziell, um Gesteinsverformung von der Korngrößen bis zur globalen Skala zu untersuchen. Wie in der dritten Studie dieser Dissertation, in der geodynamische Kontrollen auf die Entwicklung eines Grabenbruchs durch die Integration geologischer und geophysikalischer Daten in ein numerisches Modell untersucht und erfasst wurden.

Contents

1 Introduction

1.1 Strain localisation: from plate tectonics over shear zones to micromechanics

Localisation of deformation within rocks not only defines where plate boundaries develop or where earthquakes happen, it effectively shapes the Earth's surface. With increasing computational power, existing theories and models can be expanded and build on and new studies become feasible. Within this work, computational tools are utilized to investigate the controls on strain localisation, while the scale is varied from grain to lithosphere. Going down the scale from plate tectonics to micromechanics, this introduction addresses some aspects regarding localisation of deformation like the main acting forces, physical principles, and modelling techniques. Although the scale differs in order of magnitudes, some problems can be tackled with the same (numerical) approaches since the underlying physics remain identical.

Deformation of material is a ubiquitous process not restricted to geosciences and goes from bending of steel over breaking of glass to continental breakup or ductile flow in the mantle. When forces induce stress to a material, that material reacts by distributing the stress internally and/or transferring it to adjacent material. The internal distribution or partial dissipation of stress may lead to (ir)reversible deformation, called strain. The effects on a specific material depend on its properties. For rocks these effects encompass but are not limited to faulting and folding, as easy to recognize features in the field, brittle faults, ductile shear zones, crystallographic preferred orientations and many more. These features have in common that the affected material is altered in areally limited zones. The procedure of a deforming material body to store strain locally is depicted by the term *strain localisation*. How this is expressed and represented on the different scales will be discussed in the following chapters. On a further note, localisation is always relative to the governing scale. From a plate tectonic perspective, deformation localises for example in continental rifts, while on the grain-scale, it may be described by a change of crystallographic features. Examples for strain localisation structures on different scales are depicted in Figure 1.

Cross-scale aspects play a decisive role in geodynamics, which I would like to exemplify in the rift context. During the physical process of dislocation creep induced by external forces, crystallographic dislocations move through a crystal (e.g. Hirth & Tullis, 1992). Albeit this is not the fastest of geological deformation processes e.g., in terms of displacement over time, it still leads to plastic deformation of the (solid) crystal. When this solid-state creep occurs in larger volume of rock, like in the deep lithosphere, ductile shear zones may form that localise deformation induced by plate tectonic forces (e.g. Pennacchioni & Mancktelow, 2007). Necking of the mantle lithosphere is a feature in continental rifts that is again a result of the deformation of the deep lithosphere and leads

to a strength loss of the rift system (Artemjev & Artyushkov, 1971). This may finally lead to an acceleration of entire tectonic plates, a rift intrinsic feedback of residual strength and velocity (Brune et al., 2016). This example demonstrates the connection between and dependency of processes across the scales.

In the following chapters I will give some background about the plate tectonic system, underlying rheological principles and the simulation of these with numerical tools, before highlighting some research questions that are going to be answered within this thesis.

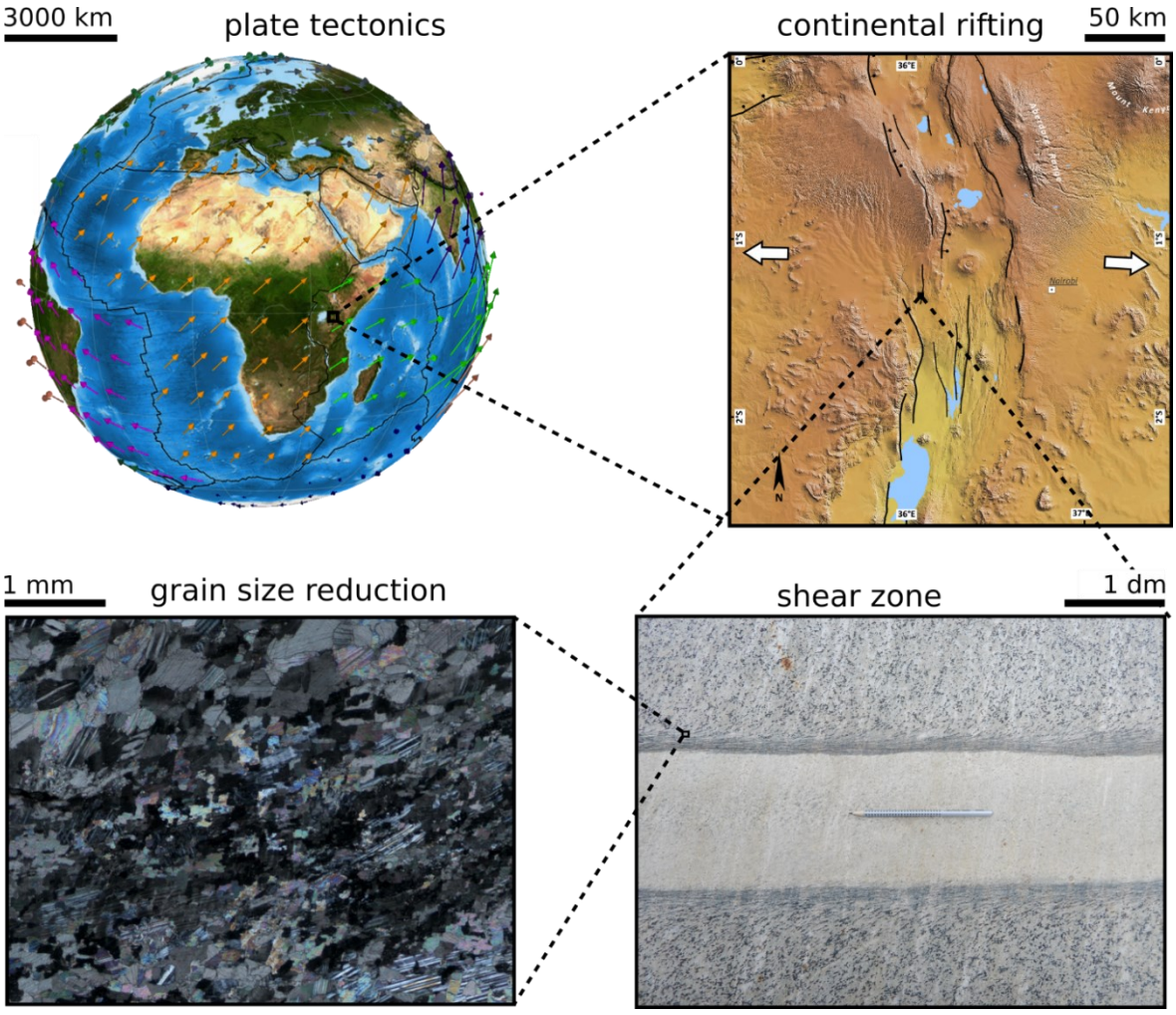

Figure 1: Strain localisation across the scales. From a plate tectonic perspective, deformation localises at plate boundaries like continental rifts. On the rift scale, localisation happens at faults or shear zones, wherein, bands of reduced grain sizes may be observed. This figure could even be extended to a smaller scale with crystallographic processes.

1.2 Plate tectonics, continental rifts, and shear zones

The plate tectonic system consists of individual tectonic plates that move on top of a weaker mantle. An individual plate can be divided into a strong plate interior and weak, strongly localised plate boundaries. These boundaries form by means of strain localisation, which is one major aspect of rift dynamics and mainly induced by plate tectonic forces on the lithospheric scale. Viscous drag (also known as basal or mantle drag), slab pull and gravitational sliding (also known as ridge push) are the main driving forces (Grotzinger & Jordan, 2010). Since its formulation and with its steady evolution, the theory of plate tectonics has greatly enhanced our understanding of the Earth. One challenge the theory has faced and that is related to the subject of this thesis, is the *tectonic force paradox*, which in principle states that the yield strength of intact continental lithosphere is too high to be overcome by mantle convection forces e.g. (Cloetingh et al., 1989; Solomatov, 1995; Buck, 2004). A combination of processes and factors is presumed to affect and reduce the lithospheric strength for it to deform significantly and rift apart. These include 1) dynamic weakening mechanisms mainly acting on the grain-scale (see below), 2) inherited weaknesses in some parts of the lithosphere like zones of past tectonic activity, 3) along strike propagation of a rift (Torsvik et al., 2009) and 4) high magmatic intrusion rates heating the lithosphere (Bialas et al., 2010; Daniels et al., 2014). For a more comprehensive synthesis of continental rift dynamics and the modelling perspective see Brune (2019).

Whether a rift may develop or not is strongly depending on the absolute thickness or the bulk strength of the lithosphere. The characteristics of a rift like its width or the depth of the main tectonic activity, however, is strongly influenced by the relative thicknesses of the distinct lithospheric layers. Principally, the lithosphere can be subdivided and described by several layers, each with their own characteristic localisation phenomena (see Figure 2). In the following, the layers are described regarding their dominant mechanical localisation behaviour. The average upper crust consists of predominantly felsic rocks that show mostly brittle behaviour at the given temperatures and pressures. Although the mineralogy of the lower crust differs from the upper crust by being more mafic, the mechanical behaviour is similar due to a generally high bulk strength. A special role in this regard has the relatively low strength middle crust, where ductile processes play a bigger role than in the upper and lower crust. Mineralogically, the middle crust is like the upper crust, but the mechanical behaviour features a strong ductile proportion mainly due to the geothermal gradient. If this weaker middle layer is thick, deformation is distributed across many and less-localised shear zones, resulting in wider rift types (Buck, 1991). While on the other hand, with a lower thickness of the mid-crust, the strongly localised faults from the upper and lower layers define the rift morphology, which tends to be of a narrow type. The ductile upper mantle as a part of the lithosphere deforms jointly with the crustal layers and localises deformation as well. This characteristic also distinguishes it from the asthenosphere, where deformation is distributed.

On the lithospheric scale, ongoing strain localisation is manifested for example in continental rift zones like the Baikal or the Kenya rift, where tectonic forces pull a continent apart. Shear zones are the most prominent characteristic that constitute such a rift and they accumulate the vast majority of strain in the lithosphere (Fossen & Cavalcante, 2017). On the surface and below down to the brittle-ductile transition, these shear zones mainly deform by means of brittle processes. Shallow earthquakes due to the rupturing of rocks are the most prominent manifestation of brittle deformation and the resulting primary slip zones are one of the most localised features in terms of deformation (Schuck et al., 2020). With increasing temperature, pressure or changing mineralogy, the main deformation mechanism of the rocks transitions into ductile deformation with several crossover states of deformation, where brittle and ductile behaviour may even coexist. In comparison to brittle fracture zones, ductile shear zones tend to be wider, but they are still a strongly localised feature. Ductile shear zone generation and progressive weakening are controlled by pre-existing heterogeneities (e.g. Duretz et al., 2016; Mazzotti & Gueydan, 2017), thermal softening (e.g. Kiss et al., 2019) and self-enhancing softening due to ongoing uptake of deformation or strain (e.g. Gardner et al., 2017; Döhmann et al., 2019). In the following chapter, I will give an overview about the physical background that enables localisation in brittle and ductile regimes.

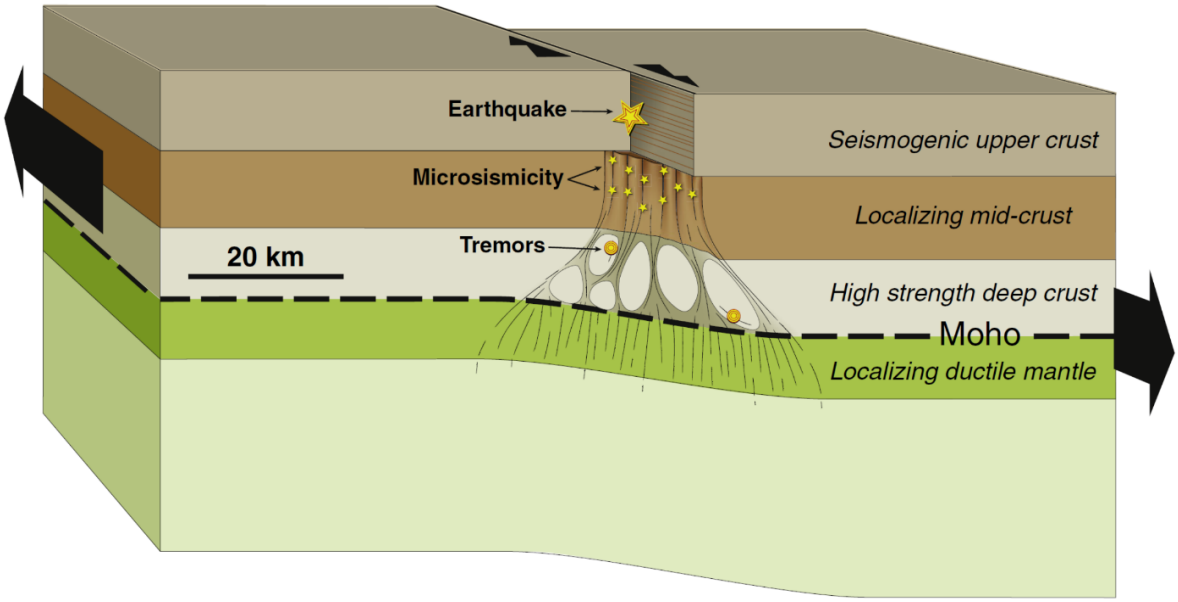

Figure 2: Schematic visualisation of preferred localisation mechanisms on the lithospheric scale in a strike-slip plate boundary setting. The layers consist of 1) a strong, brittle upper crust, 2) a weak, ductile middle crust, 3) a strong lower crust and 4) a weak, ductile but localising upper mantle. (from Gueydan et al., 2014)

1.3 Rheology and micromechanics

The physics of rocks are at the heart of tectonic processes. They are condensed in the term rheology and related to e.g., mineralogical composition, crystallography and fluid content and composition, while strongly being controlled by temperature and pressure conditions. Parameters and mechanisms are of varying importance in different geological settings. Most of the brittle tectonic deformation takes place in settings of relatively low pressures and temperatures like the uppermost kilometres of continental crust. In brittle regimes, localisation and deformation is mainly controlled by pressure-dependent frictional sliding and takes place along discontinuities when the applied stress exceeds the strength of the material. This is described by the Mohr–Coulomb failure criterion, which is also applied in numerical simulations of deformation and goes back to the combined ideas of Mohr (1900) and Coulomb (1776).

Dislocation creep and diffusion creep are the principal mechanisms of ductile deformation and are prevalent in deeper crustal regions. During the temperature-dependent viscous flow, self-enhancing strain-softening mechanisms are responsible for strain localisation in the ductile regime. For example, a switch from dislocation creep to grain-size sensitive diffusion creep as is observed in high strain rocks, and grain-size evolution are two important of many suggested mechanisms (Burlini & Bruhn, 2005). Grain-size evolution can be described as a cycle of the competing processes of grain-growth and dynamic recrystallization (Mulyukova & Bercovici, 2019). During the latter, individual crystals of a rock subdivide, e.g., by sub-grain-rotation, leading to smaller grain-sizes often resulting in weakening of the bulk material, while grain-growth through healing for example has the opposite effect. This grain-size reduction by dynamic recrystallisation is interpretated to be one of the major contributors to lithospheric weakening in the ductile regime (Platt & Behr, 2011). Whether a bulk material deforms by ductile means can be described by the pressure dependent Drucker–Prager yield criterion.

Besides the failure criterions that describe the plastic deformation, constitutive laws based on rock experiments were developed to predict the bulk behaviour and deformation of minerals and rocks or mineral assemblages at high temperatures and pressures. Especially for the major minerals of the continental crust (quartz, feldspar, and pyroxene) as well as for these of the upper mantle (olivine and pyroxene) a considerable effort was carried on assessing their high temperature creep behaviour (Rybacki & Dresen, 2000; Bystricky & Mackwell, 2001; Hirth & Kohlstedt, 2004; Rutter & Brodie, 2004; Dimanov & Dresen, 2005; Rybacki et al., 2006, 2014). Although assumptions incorporated into the constitutive laws are not entirely realistic, they give a solid basis as a description of rock material flow.

Integrating rheological properties, yield strength envelopes for the whole lithosphere can be defined. Since the early definitions from Goetze & Evans (1979) for crustal material, several models were developed to estimate and describe the lithospheric strength. Since

geological settings are quite distinct due to varying thickness, composition and structure, a single model is not sufficient to describe lithospheric strength around the Earth. Nonetheless, major models were developed, where the so called *jelly-sandwich model* is now a classic description of the lithospheric strength (Bürgmann & Dresen, 2008). It follows the scheme of Figure 2 (from Gueydan et al., 2014) with a weak layer sandwiched between stronger layers, but the crust is divided only into two layers, the lower of which is weak.

1.4 Numerical modelling of lithosphere deformation

Tackling physical problems with numerical methods has always been a part of scientific practice. The invention and construction of computers enabled new tools for solving numerical problems and with the ongoing advances in computational power, a steadily increasing complexity can be achieved and implemented. However, every numerical model is adjusted to the governing purpose and appropriate simplifications are used and not all physical properties constrained previously are necessarily implemented (e.g. Sobolev & Brown, 2019). Despite the reduced complexity of models compared to nature, they are a great tool to investigate the impact of a multitude of individual processes (Brune, 2016).

The foundation for the geodynamical modelling approaches within this thesis are the three conservation equations of mass, momentum, and energy as well as the rheology of the material (see Figure 3 from van Zelst et al. (2021)). Two different software packages were used, but both are based on these governing equations and assumptions. SLIM3D (Semi-Lagrangian Implicit Model for 3 Dimensions) developed by Popov & Sobolev (2008) was used for modelling of the torsion experiments and ASPECT (Advanced Solver for Problems in Earth's ConvecTion) (Kronbichler et al., 2012; Heister et al., 2017; Bangerth et al., 2018, 2019) was used to model the continental rift setting due to its high efficiency and parallelisation. Details regarding their implementation and limitations are discussed within Chapter 3 and 4, respectively. SLIM3D has mainly been used to investigate divergent, convergent and transform plate boundary systems. References are given in chapter 3.1. Beyond these lithospheric scale settings, centimetre-scale models on the localisation processes in ice were also successfully conducted with SLIM3D (Cyprych et al., 2016), proving the applicability for the smaller scale. ASPECT on the other hand was originally designed to model convection in the Earth’s mantle but was and still is continuously extended. It has since been used to investigate a variety of geodynamic topics, ranging from mantle convection (Faccenna et al., 2021) and plumes (Bredow & Steinberger, 2021) to plate boundaries (Barrionuevo et al., 2021; Heckenbach et al., 2021; Sandiford et al., 2021) just to name some recent applications of the software.

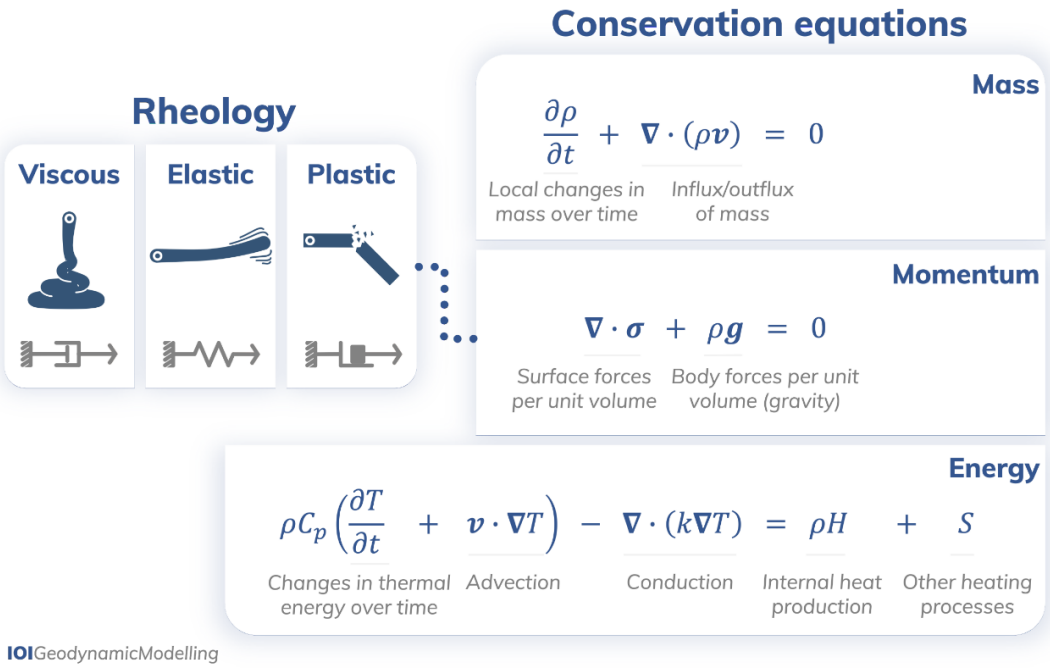

Figure 3: The governing equations: conservation of mass, conservation of momentum, and conservation of energy with different types of rheology. ρ is the density, t is time, v the velocity vector, σ the stress tensor, g the gravitational acceleration vector, C_p the heat capacity, T the temperature, k the thermal conductivity, H a volumetric heat production term (e.g., due to radioactive decay) and the term S = S1 +S2 +S3 accounts for friction heating, adiabatic heating, and the release or consumption of latent heat (e.g., associated with phase changes), respectively. Note that the plastic rheology depicted here is the geodynamic approximation of brittle failure. (from van Zelst et al., 2021)

1.5 Research topics

Many studies exist that investigate the rheology of minerals, mineral assemblages and natural rocks based on laboratory experiments (e.g. Schmid et al., 1980; Pieri et al., 2001; Hirth & Kohlstedt, 2003; Rutter & Brodie, 2004; Burlini & Bruhn, 2005; Dimanov & Dresen, 2005; Rybacki et al., 2006, 2014; Tasaka et al., 2017). From these laboratory conditions, rheological laws or flow laws are formulated that can be extrapolated to the temperatures and pressure prevalent in the Earth's interior. These flow laws are often used in studies that employ numerical methods to investigate for example the plate tectonic system or continental rifts by means of dynamic flow models (e.g. Sobolev et al., 2011; Osei Tutu et al., 2018; Salazar-Mora et al., 2018; Jammes & Lavier, 2019; Barrionuevo et al., 2021). Hence, quite a lot of studies depend on the quality and validity of these experiments. Within the first two papers of this thesis, such rheological experiments were performed in the laboratory and implemented numerically to investigate the initiation of a shear zone and the numerical softening parameters. The numerical models were validated by and complemented the laboratory experiments and expanded the investigable frame as a virtual way of analysing viscous process zone evolution. The rheological experiments within chapter 2 and 3 tackle the following questions:

- How are loading conditions affecting shear zone initiation?
- How does a viscous shear zone evolve?
- Which weakening processes are prevalent?
- What weakening law captures the behaviour of the twisted Carrara marble?

With a switch to a larger scale, where weakening processes based on chapter 2 and 3 are incorporated into the numerical simulations, the focus lays on the initiation and early evolution of continental rifts on the example of the Southern and Central Kenya Rifts. By reproducing major aspects of the two rifts regarding geological and geophysical data, a reference model is established. Recently, the importance of inherited structures on the style of continental deformation and rift evolution has been emphasised (e.g. Hodge et al., 2018; Jammes & Lavier, 2019; Duclaux et al., 2020). Randomly distributed minor flaws are used as a weak seed for the numerical models within this work. From the reference model as a base, the study is extended to investigate the range of possible rift geometries within these specific geological setting and to look at the following issues:

- How and why does an asymmetric, narrow rift form in this setting?
- Does a purely tectonic model suffice to model the Southern and Central Kenya rift?
- What range of rift geometries can be produced within the given tectonic setting?

1.6 Manuscript Overview and Author Contributions

The three main chapters of this thesis consist of manuscripts that have been submitted to and published in peer-reviewed scientific journals. At the timing of writing, all three manuscripts have been published.

Chapter 2, 1. Manuscript: High-temperature shear zone formation in Carrara marble: The effect of loading conditions

Authors: Livia Nardini, Erik Rybacki, Maximilian J. E. A. Döhmann (now: Richter), Luiz F. G. Morales, Sascha Brune, Georg Dresen

https://doi.org/10.1016/j.tecto.2018.10.022

Besides co-authoring and revising the first manuscript, I contributed by conducting numerical models to gain further insight into the evolution of the experiment and the localisation pattern, by interpreting and discussing the results regarding the geodynamic context and by producing Figure 16 of the manuscript. The manuscript was mainly authored by Livia Nardini.

Chapter 3, 2. Manuscript: Strain localization and weakening processes in viscously deforming rocks: Numerical modeling based on laboratory torsion experiments

Authors: Maximilian J. E. A. Döhmann (now: Richter), Sascha Brune, Livia Nardini, Erik Rybacki, Georg Dresen

https://doi.org/10.1029/2018JB016917

The second manuscript was mainly authored by me, while the revisions made by the co-authors helped to improve the paper. I conducted the numerical models and produced the Figures.

Chapter 4, 3. Manuscript: Controls on Asymmetric Rift Dynamics: Numerical Modeling of Strain Localization and Fault Evolution in the Kenya Rift

Authors: Maximilian J. E. A. Richter (geb. Döhmann), Sascha Brune, Simon Riedl, Anne Glerum, Derek Neuharth, Manfred R. Strecker

https://doi.org/10.1029/2020TC006553

The second manuscript was mainly authored by me, and the revisions made by the co-authors helped to improve the paper. Simon Riedl mainly authored the chapter 2. I conducted the numerical models and produced the Figures, except Figure 1, which was made by Simon Riedl.

2 High-temperature shear zone formation in Carrara marble: The effect of loading conditions

Nardini, L., Rybacki, E., Döhmann, M. J. E. A., Morales, L. F., Brune, S., & Dresen, G.

2018

Tectonophysics, *749*, 120-139

https://doi.org/10.1016/j.tecto.2018.10.022

Keywords:

- Shear zones
- Localization
- Marble
- Torsion
- Loading conditions

Abstract

Rock deformation at depths in the Earth's crust is often localized in high temperature shear zones occurring at different scales in a variety of lithologies. The presence of material heterogeneities is known to trigger shear zone development, but the mechanisms controlling initiation and evolution of localization are not fully understood.

To investigate the effect of loading conditions on shear zone nucleation along heterogeneities, we performed torsion experiments under constant twist rate (CTR) and constant torque (CT) conditions in a Paterson-type deformation apparatus. The sample assemblage consisted of cylindrical Carrara marble specimens containing a thin plate of Solnhofen limestone perpendicular to the cylinder's longitudinal axis. Under experimental conditions (900 °C, 400 MPa confining pressure), samples were plastically deformed and limestone is about 9 times weaker than marble, acting as a weak inclusion in a strong matrix. CTR experiments were performed at maximum bulk shear strain rates of ~ $2*10^{-4}$ s^{-1}, yielding peak shear stresses of ~ 20 MPa. CT tests were conducted at shear stresses of ~ 20 MPa resulting in bulk shear strain rates of 1–$4*10^{-4}$ s^{-1}. Experiments were terminated at maximum bulk shear strains of ~ 0.3 and 1.0.

Strain was localized within the Carrara marble in front of the inclusion in an area of strongly deformed grains and intense grain size reduction. Locally, evidence for coexisting brittle deformation is also observed regardless of the imposed loading conditions. The local shear strain at the inclusion tip is up to 30 times higher than the strain in the adjacent host rock, rapidly dropping to 5 times higher at larger distance from the inclusion. At both bulk strains, the evolution of microstructural and textural parameters is independent of loading conditions. Our results suggest that loading conditions do not significantly affect material heterogeneity-induced strain localization during its nucleation and transient stages.

2.1 Introduction

Localization of deformation in the deep crust and mantle is a key mechanism involved in the formation of tectonic plates and mountain belts on our planet (Tackley, 2000; Schubert et al., 2001; Bercovici and Karato, 2002; Bercovici, 2003; Regenauer-Lieb & Yuen, 2003; Regenauer-Lieb and Yuen, 2004). Therefore, the knowledge of how deformation is accommodated at plate boundaries and orogenic belts requires the understanding of physical processes that govern localized deformation in the ductile regime and its persistence over geological times.

A multitude of mechanisms have been proposed to be responsible for nucleation of localized deformation in the middle to lower crust, under the generally accepted premise that a dynamic (positive) feedback mechanism is required to induce thermo-mechanical perturbances in otherwise homogeneously deforming mediums (Bercovici, 1996, 1998; Bercovici and Karato, 2002; Regenauer-Lieb & Yuen, 2003). Grain size reduction by

dynamic recrystallization (e.g. Montési & Hirth, 2003; Kilian et al., 2011; Platt & Behr, 2011b), fluid influx inducing metamorphic reactions (e.g. Fusseis & Handy, 2008), development or pre-existence of a crystallographic preferred orientation (e.g. Michibayashi & Mainprice, 2004; Tommasi et al., 2009), ductile fracturing (e.g. Handy and Stünitz, 2002; Dimanov et al., 2007; Rybacki et al., 2008; Menegon et al., 2013) and the presence of material heterogeneities (e.g. Rybacki et al., 2014) are only some of the mechanisms that were recognized in the field and through experimental work as factors causing rheological weakening and subsequent ductile localization of strain (see Burlini & Bruhn, 2005 for a review). A number of experimental investigations at constant strain rate have failed to produce notable localization in monophase materials in the ductile regime even at very high strains (e.g. Bystricky et al., 2000; Ter Heege et al., 2002; Barnhoorn et al., 2004). Some observations suggest that constant stress loading conditions appear to initiate localization in highly deformed olivine aggregates (Hansen at al., 2012). However, the effects of material properties and boundary conditions on the mechanical and microstructural evolution associated with strain localization and weakening are not yet understood and only a few experimental studies have addressed this. So far, the effect of the imposed loading conditions on the efficiency of localization within homogeneous materials has largely been investigated in theoretical models (Fressengeas & Molinari, 1987; Leroy & Molinari, 1992; Paterson, 2007) but experimental studies of ductile localization induced by some of the aforementioned mechanisms of rheological weakening have not yet been performed.

In nature, calcite-rich rocks are known to host localized shear zones developed in the high temperature ductile regime, leading to the formation of large scale shear zones where up to tens of kilometres of displacement are accommodated (e.g. the Glarus Thrust in the Helvetic Nappe, Groshong et al. 1984; Herwegh & Kunze, 2002; Ebert et al., 2007). Calcite and natural carbonate materials have been extensively studied in the ductile regime both experimentally (e.g. Schmid et al., 1980; Rutter, 1994, 1995, Pieri et al., 2001a, 2001b; Barnhoorn et al., 2004) and in the field (Schmid et al., 1981; Bestmann et al., 2000; Rogowitz et al., 2014, 2016), so that the calibration of mechanical, microstructural and textural data for calcite at different deformation conditions is well established.

In this contribution, we experimentally investigate the effects of different loading conditions (constant stress versus constant strain rate) on the nucleation and evolution of heterogeneity-induced high temperature shear zones in a carbonate system. It is important to anticipate that the phenomena investigated in the present study are inherently transient, as they mimic the nucleation stage of shear zone formation and its progressive propagation within intact material. Therefore, the loading condition may affect the shear zone evolution, which is in contrast to the commonly assumed path-independency of steady state deformation treated as being in thermodynamic equilibrium.

2.2 Experimental setup

The torsion experiments presented here were carried out on mono-mineralic calcite aggregates consisting of Carrara marble with elongated Solnhofen limestone inclusions. A thin (0.75 mm) circle segment of Solnhofen limestone with an arc length of about 11.8 mm was inserted in a saw-cut slot in a hollow cylinder (10 mm height, 15 mm outer diameter, 6.1 mm inner diameter) of Carrara marble. Ceramic glue was used to fill up the possible gaps in the slot. Two alumina spacers (for protection of the pistons in the deformation apparatus) and a solid gold cylinder inserted in the inner borehole of the sample completed the setup (Fig. 1).

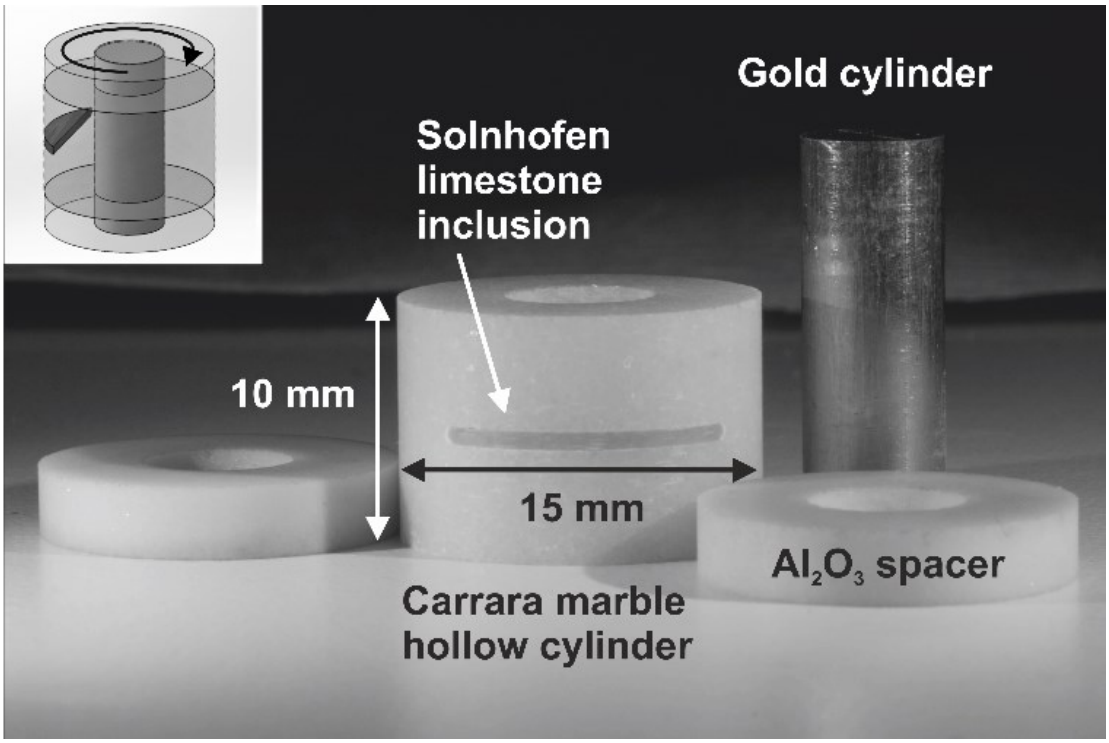

Fig. 1. *Elements of the sample assembly. In the small inset, the setup prior to insertion in the copper jacket; indicated is the direction of the applied torsion.*

The hollow cylinder configuration was preferred as it guarantees a relatively homogeneous distribution of shear stress within the sample (Paterson and Olgaard, 2000). Carrara marble is a largely used material in experimental rock deformation due to its exceptional purity (> 99% $CaCO_3$) and low to no initial porosity (Rutter, 1995; Pieri et al., 2001a and 2001b; Ter Heege et al., 2002; Barnhoorn et al., 2004; De Bresser et al., 2005). The undeformed marble shows a uniform grain size distribution with an average grain size on the order of the hundreds of microns (~ 150 μm), abundant triple junctions, straight grain boundaries and a quasi-uniform crystallographic orientation distribution (see *section 4.3* and figures therein). Twinned crystals are present, but the twins are extremely thin (< 5 μm), straight and not pervasive; these types of twins are commonly

interpreted as late features typical of a low temperature natural environment (Burkhard, 1993; Ferrill et al., 2004). Solnhofen limestone is an extremely fine grained (~ 5 µm average grain size) almost pure calcite rock (more than 97 wt.% calcite, Rutter, 1972), which has been long used as a standard material for experimental deformation of natural fine-grained calcite (e.g. Rutter, 1972; Rutter and Schmid, 1975; Schmid et al., 1980; Schmid et al., 1987; Casey et al., 1998). As a consequence of a large difference in initial grain size, Solnhofen limestone is up to 9 times weaker than Carrara Marble at the imposed experimental conditions of 900 °C temperature and 400 MPa confining pressure (e.g. Rybacki et al., 2014). As a result, the Solnhofen limestone inclusion and Carrara marble host introduce a large viscosity contrast in the experimental setup.

Experiments were performed in a Paterson-type gas deformation apparatus equipped with a torsion actuator (Paterson and Olgaard 2000). Prior to experimental runs, the samples were inserted into copper jackets of ~ 0.2 mm thickness (to isolate them from the gas confining pressure medium) the strength of which is accounted for in the evaluation of the mechanical data. The samples were first pressurized to 400 MPa, followed by heating at a rate of ~ 30 °C/min up to the desired temperature of 900 °C (with accuracy of ± 2 °C along the sample axis). After test termination, the load imposed by the actuator was maintained constant during cooling (at equal rate to the heating phase) to preserve deformation microstructures and to reduce the amount of static recovery occurring within the samples.

Following Paterson and Olgaard, 2000, the measured torque M was converted to maximum shear stress τ at the periphery of the sample cylinder according to the equation:

$$\tau = \frac{4M\left(3+\frac{1}{n}\right)}{\pi} \frac{D_0^{\frac{1}{n}}}{D_0^{3+\frac{1}{n}} - D_i^{3+\frac{1}{n}}} \quad (1)$$

where D_0 and D_i are the external and internal diameters of the cylinder, respectively. Measured displacement rate $\dot{\theta}$ in radians is converted to maximum shear strain rate $\dot{\gamma}$ according to the following:

$$\dot{\gamma} = \frac{D_0 \dot{\theta}}{2l} \quad (2)$$

where D_0 is the external diameter of the sample and l is the length of the cylindrical specimen.

2.3 Analytical methods

Thin sections were produced for microstructural and textural investigations. To ensure the analyses were carried out on the portion of the sample that experienced the highest (measured) strain, the sections were cut tangentially to the outer rim and parallel to the longitudinal axis of the cylinders (after Paterson & Olgaard, 2000). The thin sections were

polished in two steps, first with diamond paste up to 0.25 µm grain size followed by 2 hours of chemical-mechanical polishing with an alkaline solution of colloidal silica. To investigate the crystallographic orientation of the calcite grains, all thin sections were examined with the electron back-scattered diffraction (EBSD) technique on a FEI Quanta 3D FEG dual beam machine equipped with an EDAX-TSL Digiview IV EBSD detector and the TSL software OIM 5.31 for the acquisition of diffraction patterns. EBSD analyses were performed on uncoated samples under low vacuum conditions (10 Pa H_2O) using an accelerating voltage of 15 kV and beam current of 8 nA at variable working distances between 13 and 16 mm.

Crystallographic orientation mapping was performed systematically in all samples using two different step sizes (10 µm and 3.5 µm). The coarser step size map was used to map the orientations of the whole sample and for the construction of mean grain size profiles across the thin sections (top to bottom; orange rectangles in Fig. 2a–d). The fine step size mapping was limited to the area in front of the limestone inclusion, where deformation in the marble localizes (Fig. 3a–d); these maps were used for the study of shape descriptors (*section 2.4.4*) and their variations within regions in and outside of the localized zone in front of the inclusion (red rectangles in Fig. 3a–d).

Clean-up of the raw data was carried out using the TLS software OIM Analysis 7.3, with standardization of the confidence index (CI) within grains. Individual grains were defined using the following parameters: minimum grain tolerance angle of 10° (misorientation angle between neighbouring points) and a minimum of 10 indexed points per grain. Following this step, a CI correlation between neighbour points was applied to the datasets with low CI (< 0.1) points reassigned to the orientation and CI of the neighbour data point with the highest CI within individual grains.

To identify very small (dynamically recrystallized) grains and their spatial distribution, a minimum of 5 indexed points per grain criterion (to reduce the loss of small grains by interpolation and smoothing) was used in the finer stepping size maps within a region of interest (Fig. 3a-d, black rectangles). Unless otherwise specified, grain sizes are expressed as equivalent diameter (diameter of a circle of equivalent area to the grain).

Calculations on the EBSD data were performed using the MTEX 4.3.2 toolbox for Matlab (Hielscher and Schaeben, 2008; Bachmann et al., 2010). Orientation distribution function and pole figure contouring were calculated using a Gaussian half-width of 10° and a maximum harmonic expansion factor of 32.

Grain size evolution across the samples (see *section 2.4.4*) was investigated using the coarser EBSD maps (10 µm step size). A moving, partially overlapping (one third of the vertical size) window of size 1.85x0.5 mm (Fig. 2a-d) was used to extract data along a profile parallel to the longitudinal axis of the sample cylinder located directly in front of the limestone inclusion in the Carrara marble. Grains transected by the boundary of the

moving window were excluded from the calculations. For each window, we estimated the average grain size using the RMS (root mean square) value of the distribution.

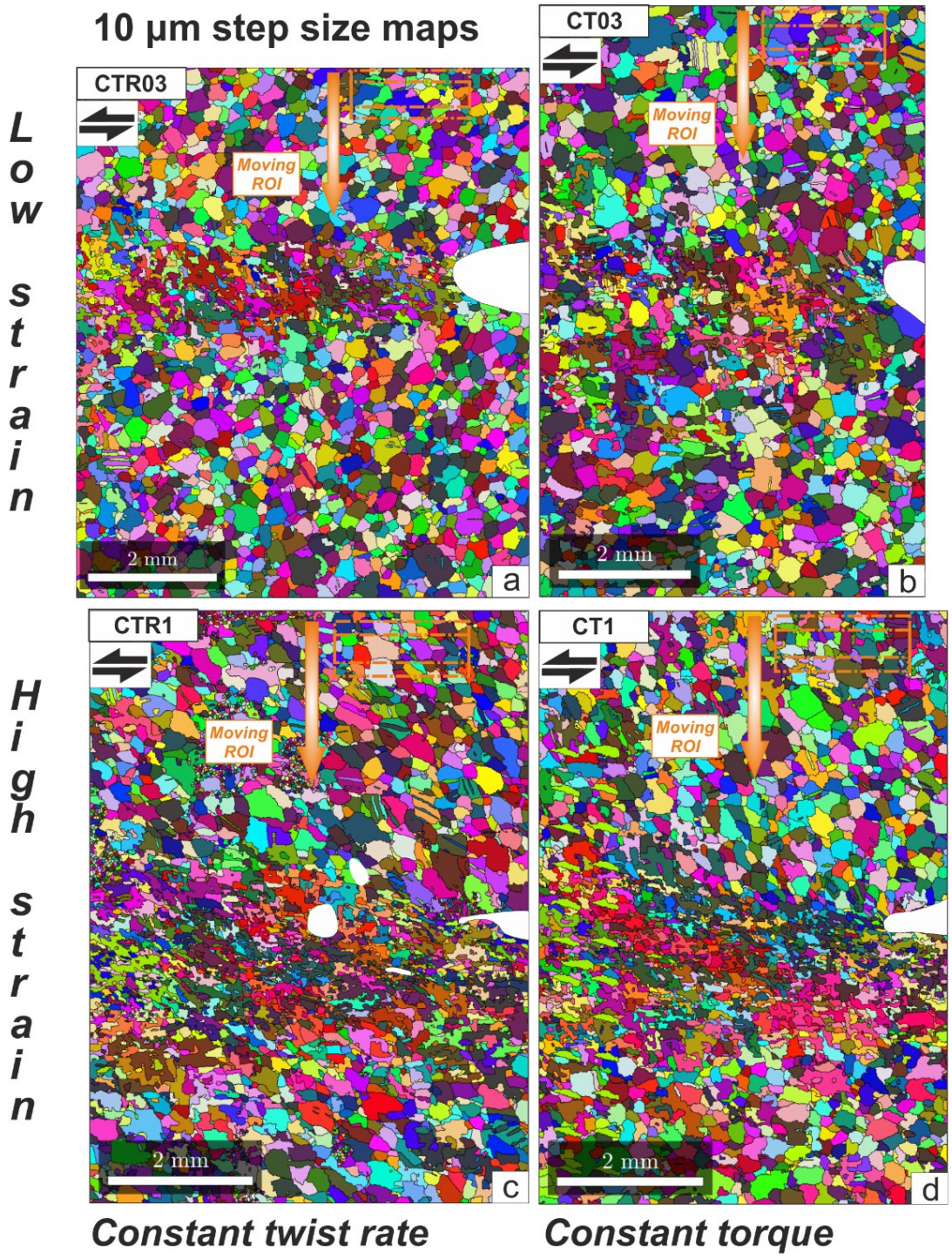

Fig. 2. *a–d: 10 µm step size orientation maps from EBSD data, used for the construction of grain size profiles across the thin sections (in orange, the partially overlapping moving region of interest, ROI). In a and c the constant twist rate samples and in b and d the constant torque ones. Colour coding represent IPF (inverse pole figure); the white patches in c are patches of misoriented data due to damages in the thin section.*

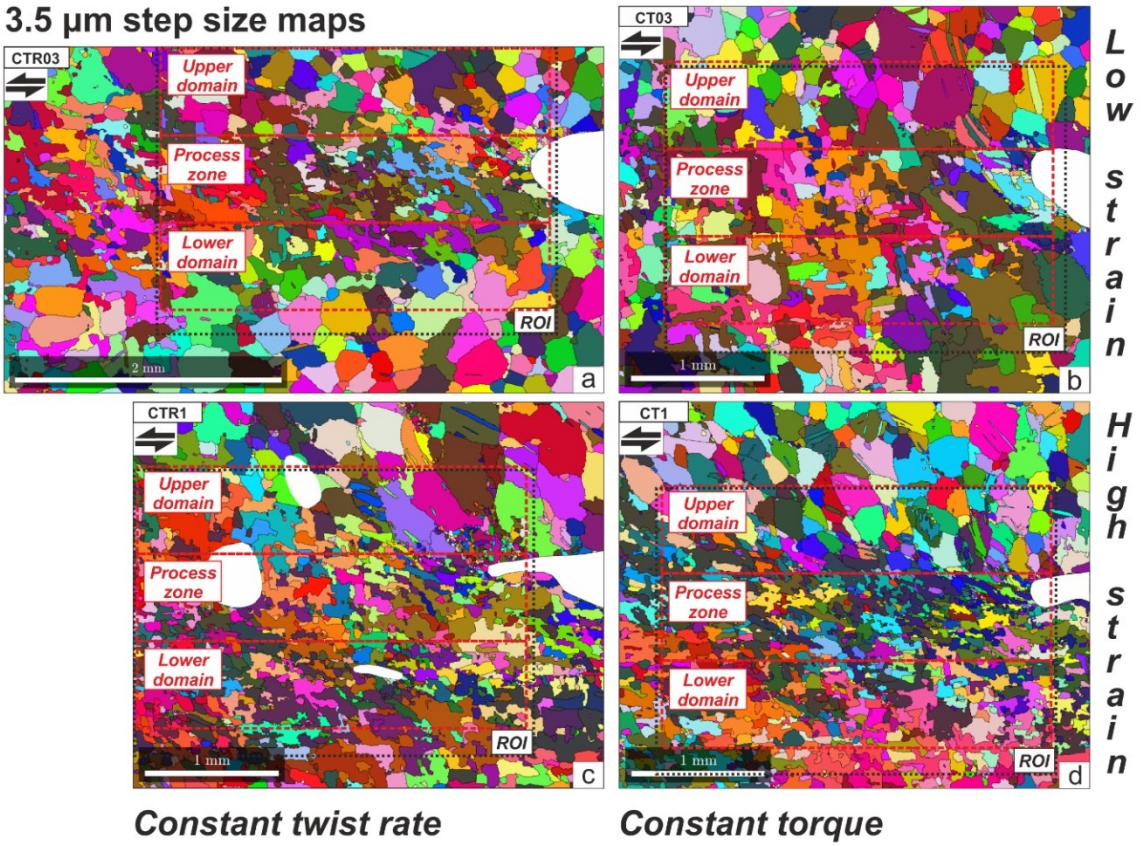

Fig. 3. *a–d: Location of regions of interest for different data extractions on 3.5 µm step size orientation maps from EBSD data. Two types of areas (red and black) are considered for different calculations. In a and c the constant twist rate samples, in b and d the constant torque ones. Colour coding represent IPF (inverse pole figure); the white patches in c are patches of misoriented data due to damages in the thin section. (For interpretation of the references to colour in this figure legend, the reader is referred to the web version of this article.)*

To characterize grain shape evolution within the area covered by the finer step size maps (*section 2.4.4*), two shape descriptors were considered. First, the inverse aspect ratio (according to the definition of the MTEX toolbox, Hielscher and Schaeben, 2008: $IAR = \frac{w}{l}$, w and l being the width and length of the particle, respectively) and secondly a variation of the classical circularity shape factor, defined as follows:

$$Circ = \frac{4\,\pi\,A}{P^2}, \qquad (4)$$

where A is the area and P the perimeter of a grain (Heilbronner and Barrett, 2014). Both shape descriptors assume values between 1 and 0, where the former represents a circle (maximum IAR) with smooth surfaces (maximum circularity) and the latter is characteristic of an infinitely non-circular shape (minimum IAR) with infinitely rough surfaces (minimum circularity).

For the study of shape descriptors, a grain size filtering was applied to the datasets in order to remove small grains produced by dynamic recrystallization, which are expected to approach the ideal circular shape at the time of formation. The size filter was set to 20 μm, which is the average grain size of dynamically recrystallized grains determined by optical microscopy.

Six transmission electron microscopy foils (0.15 μm in thickness) from a single thin section (sample CTR03) were prepared using the focused ion beam technique (e.g. Wirth, 2005) and subsequently inspected with transmission electron microscopy (TEM) on a FEI Tecnai G2F20 X-Twin TEM for the calculation of dislocation densities (see *section 2.4.5*).

2.4 Results

2.4.1 Mechanical data

We present the results from four experiments, two of which were run at constant twist rate and two at constant torque conditions (CTR and CT, respectively, equivalent to constant strain rate and constant stress) in the torsion setup of a Paterson-type gas deformation apparatus. The final bulk strains reached in the experiments are γ ~0.3 and γ ~1, respectively, for both loading configurations. Experimental conditions for the four samples presented here are shown in Table 1.

Table 1. *Experimental conditions for the four samples examined. CTR is constant twist rate (strain rate) experiments, CT constant torque (stress),* $\dot{\gamma}$ *is shear strain rate (in* s^{-1}*),* γ_{max} *is maximum bulk shear strain and* γ_{sec} *is the local shear strain in a section of radius* r_{sec}*.*

Sample name	P (MPa)	T (°C)	Test type	$\dot{\gamma}$, s^{-1}	τ, MPa	γ_{max}	γ_{sec}
CTR03	400	900	Torsion	1.8×10^{-4}	20.1	0.293	0.2
CT03	400	900	Torsion	$2.1–2.4 \times 10^{-4}$	19.8	0.29	0.2
CTR1	400	900	Torsion	1.9×10^{-4}	19.7–17.6	0.99	0.68
CT1	400	900	Torsion	$1.2–4.0 \times 10^{-4}$	18.8–18.4	0.94	0.65

In CTR experiments (Fig. 4a), shear stress is plotted against bulk shear strain, while for CT experiments (Fig. 4b), shear strain rate is plotted versus bulk shear strain in semi-logarithmic scale. In constant twist rate experiments, measured peak shear stresses of about 19 MPa at the periphery of the samples are reached at low values of bulk shear strain (γ ~0.15), after which mechanical softening occurs and a gradual weakening of the samples can be observed up to the maximum bulk strains reached, γ = 0.29 for sample CTR03 and γ = 0.99 for sample CTR1. For constant torque experiments, the applied torque was set so that the shear stress at the periphery of the samples is ~19 MPa, similar to the maximum stress measured in constant twist rate tests. Bulk shear strain rates first

decreased rapidly due to elastic loading, followed by a gradual decrease up to a minimum at γ ~0.1-0.2. Subsequently, strain rates increased corresponding to mechanical weakening of the samples up to a factor of about 4 at $\gamma = 1$ (Fig. 4b). The slightly higher minimum strain rate of sample CT03 compared to CT1 is related to the higher initially applied stress (Tab. 1).

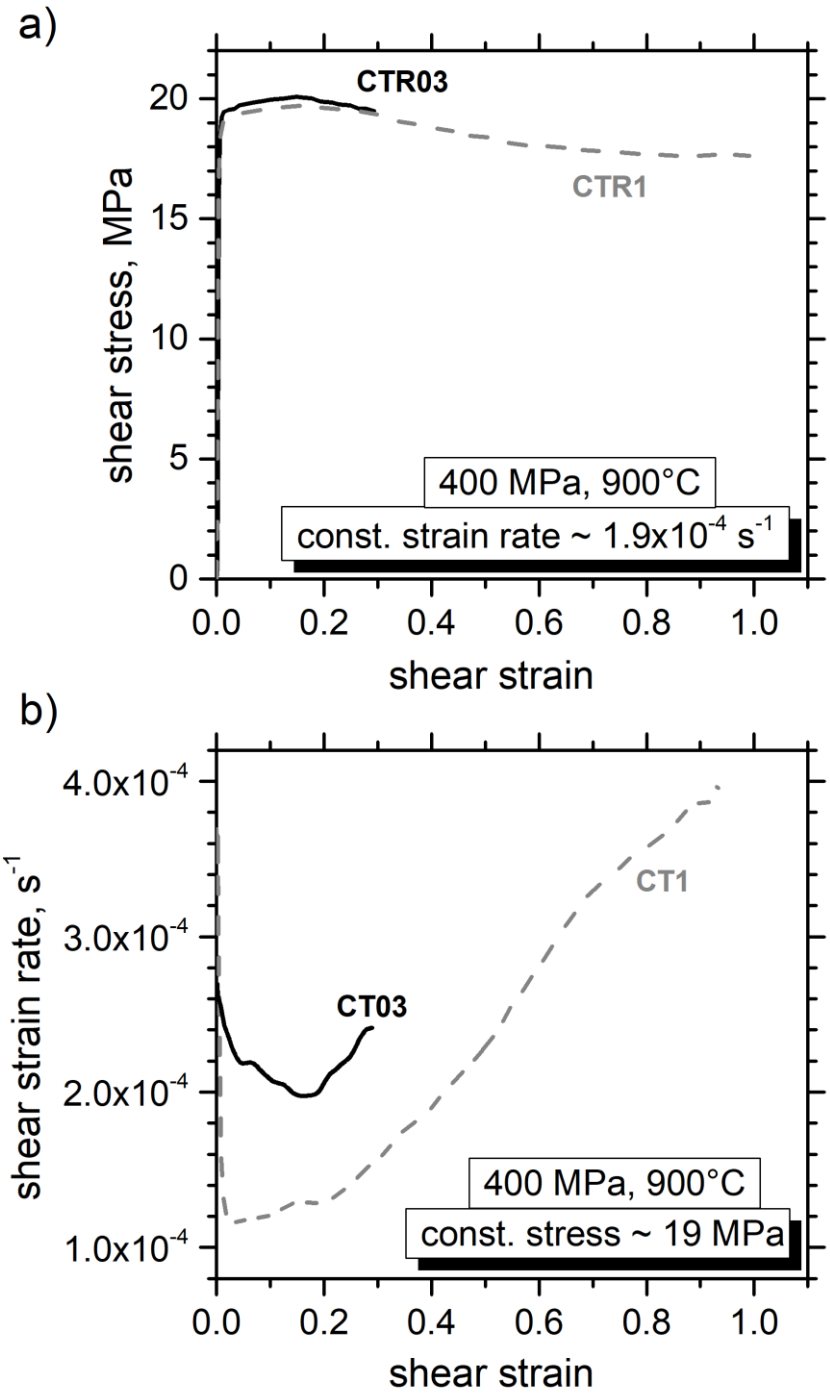

Fig. 4. *a and b: Mechanical shear stress-strain curves of torsion experiments performed at constant twist rate (a) and constant torque (b).*

2.4.2 Strain localization

In order to quantify the local distribution of shear strain within the samples, passive strain markers were applied to the copper jackets prior to the experimental runs (except for sample CTR03). A grid of evenly spaced straight lines, parallel to the cylinder axis, was carved in the copper jacket (Fig. 5; with denser spacing applied to the area where the inclusion is) and recovered after the experiments. The locally imposed shear strain is estimated from the angular deflection of the originally straight lines. After deformation, the distribution of those lines is clearly heterogeneous and reflects the partitioning of strain between the limestone inclusion and the Carrara marble.

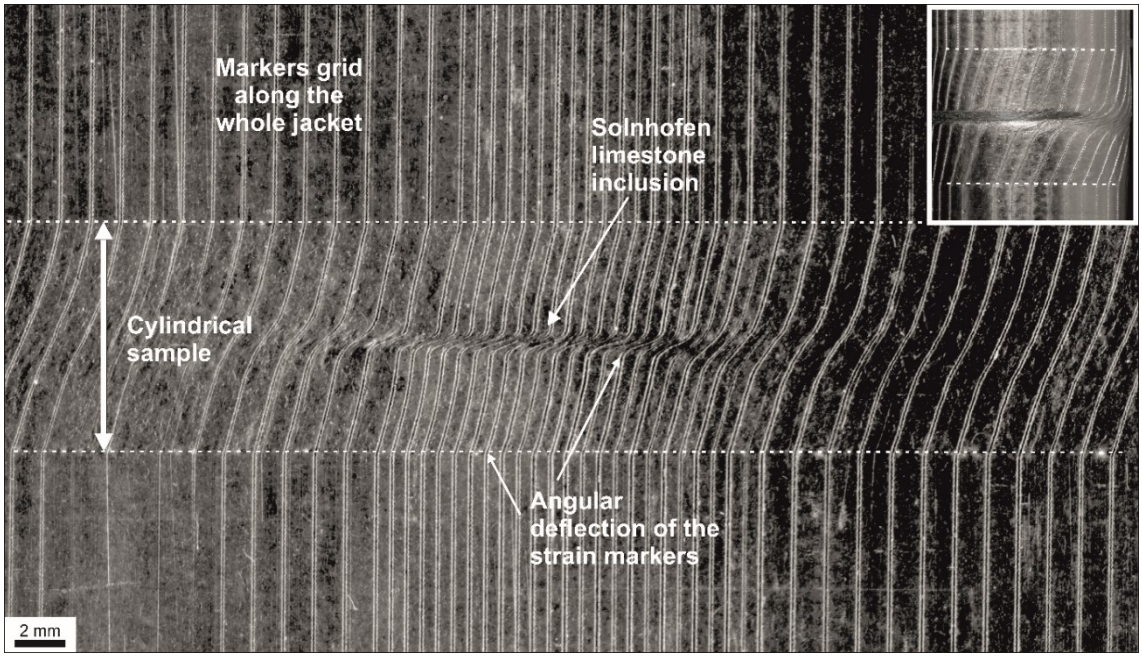

Fig. 5. *Example of the strain markers grid as applied on the copper jacket, recovered after the experimental run.*

In particular, a substantial difference in shear strain can be observed between the region directly in front of the Solnhofen inclusion and the surrounding matrix, indicative of ongoing strain localization within the Carrara marble itself, related to the presence of a nearby material heterogeneity.

Local shear strains are calculated for this area of incipient localized deformation (named hereafter the process zone) and for the less deformed matrix at some distance from the inclusion tip. A strongly localized shear strain in front of the inclusion is observed (up to a factor ~12 compared to the imposed bulk strain), rapidly decaying to background strain level with distance (~10 mm) from the inclusion (Fig. 6a). The degree of strain localization (i.e. the ratio between local to bulk shear strain) is not substantially different between the two loading conditions of constant twist rate or constant torque (cf., samples CTR1 and CT1, respectively), especially when one considers the large uncertainty in the

calculated local strains when the angular deflection is large and the measurements become less accurate (a 3° variation can lead to a difference in γ of 10).

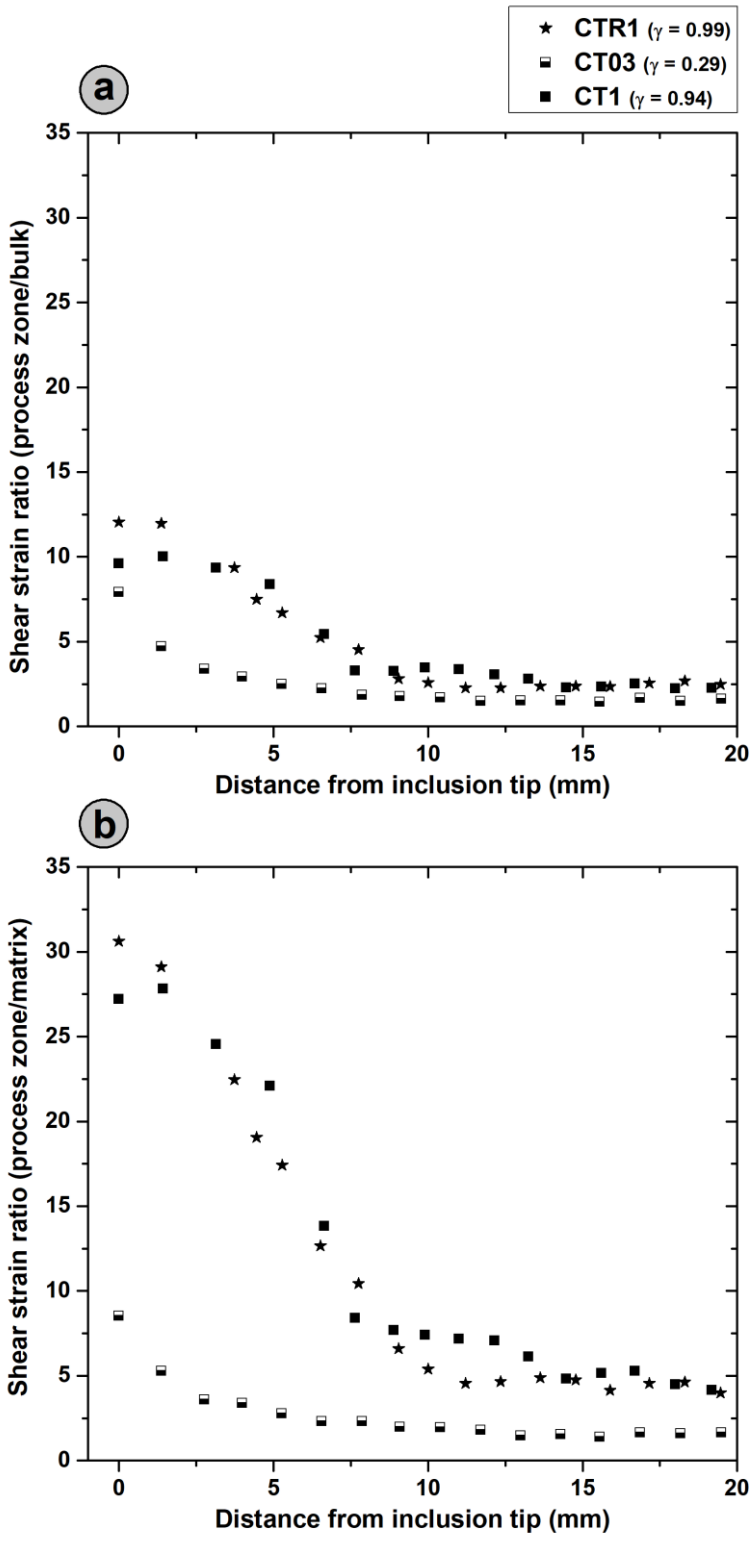

Fig. 6. *a and b: Local shear strain evolution with distance from inclusion tip. a) Normalized local shear strain ($\gamma_{process\ zone}/\gamma_{bulk}$); b) local shear strain ratio, $\gamma_{process\ zone}/_{matrix}$.*

In Fig. 6b the local strain measured in the process zone is normalized to that of the surrounding, less deformed matrix, plotted against distance from the inclusion tip in the lateral dimension. The localization of deformation in the process zone with respect to the adjacent matrix is higher by a factor ~2–3 than with respect to the bulk strain (Fig. 6a). Clearly, the degree of localization is further developed at higher total bulk strain (samples CTR1 and CT1, as opposed to sample CT03). Again, no substantial difference is noticed between constant stress and constant strain rate samples.

2.4.3 Microstructures

In composite micrographs from optical microscopy images we typically observe an area of intense grain size reduction and highly deformed grains in the Carrara marble matrix, close to the Solnhofen limestone inclusion (Fig. 7a–b and f–g). In contrast, the surrounding matrix region remains almost undeformed, and equant grains display similar characteristics to the undeformed Carrara marble (Fig. 7k–m). Note that the bulk shear strain indicated on the micrographs refers to the maximum measured shear strain. Approximate local shear strain γ_{sec} within a section of the sample cylinder cut at a radius r_{sec} is about 30% lower (Table 1), determined by:

$$\gamma_{sec} = \frac{r_{sec}}{r}\gamma_{max} \qquad (3)$$

In all micrographs the Solnhofen limestone inclusion is located on the right side, showing at higher strain stronger distortion from the original undeformed rectangular shape (Fig. 1).

In the low strain samples (CTR03 and CT03, γ ~0.3; Fig. 7a and f) the process zone, represented by the area of intense localized deformation in front of the inclusion tip, is characterized by intense twinning, with grains often developing two distinct sets of twins oriented at ~60° to each other (Fig. 7c and 7h–i). Bending and tapering of twin sets can be observed in several cases (arrows in Fig. 7c and i). After Burkhard, 1993 and Ferrill et al., 2004, twins are identified as predominantly type 2 and 3, with some remnants of type 1 twins mainly at a distance from the inclusion. Undulose extinction and lobate grain boundaries (arrows in Fig. 7c–d and Fig. 7h–i) are pervasive, indicating active crystal plasticity and intracrystalline deformation mostly by dislocation glide. Grain size reduction by dynamic recrystallization is incipient in the process zone of the low strain samples. Qualitatively, the microstructures of the two samples deformed to similar strain at different boundary conditions show similar characteristics.

The most striking feature characterizing the process zone of the high bulk shear strain samples (CTR1 and CT1, γ ~1; Fig. 7b and g) is the intense grain size reduction due to pervasive dynamic recrystallization (Fig. 7e and j), frequently resulting in core-and-mantle structures. The abundance of undulose extinction, lobate grains boundaries and subgrains similar in size to the recrystallized grains suggest prevailing subgrain rotation recrystallization with subordinate contributions of grain boundary migration recrystallization (Guillope and Poirier, 1979; Drury and Urai, 1989).

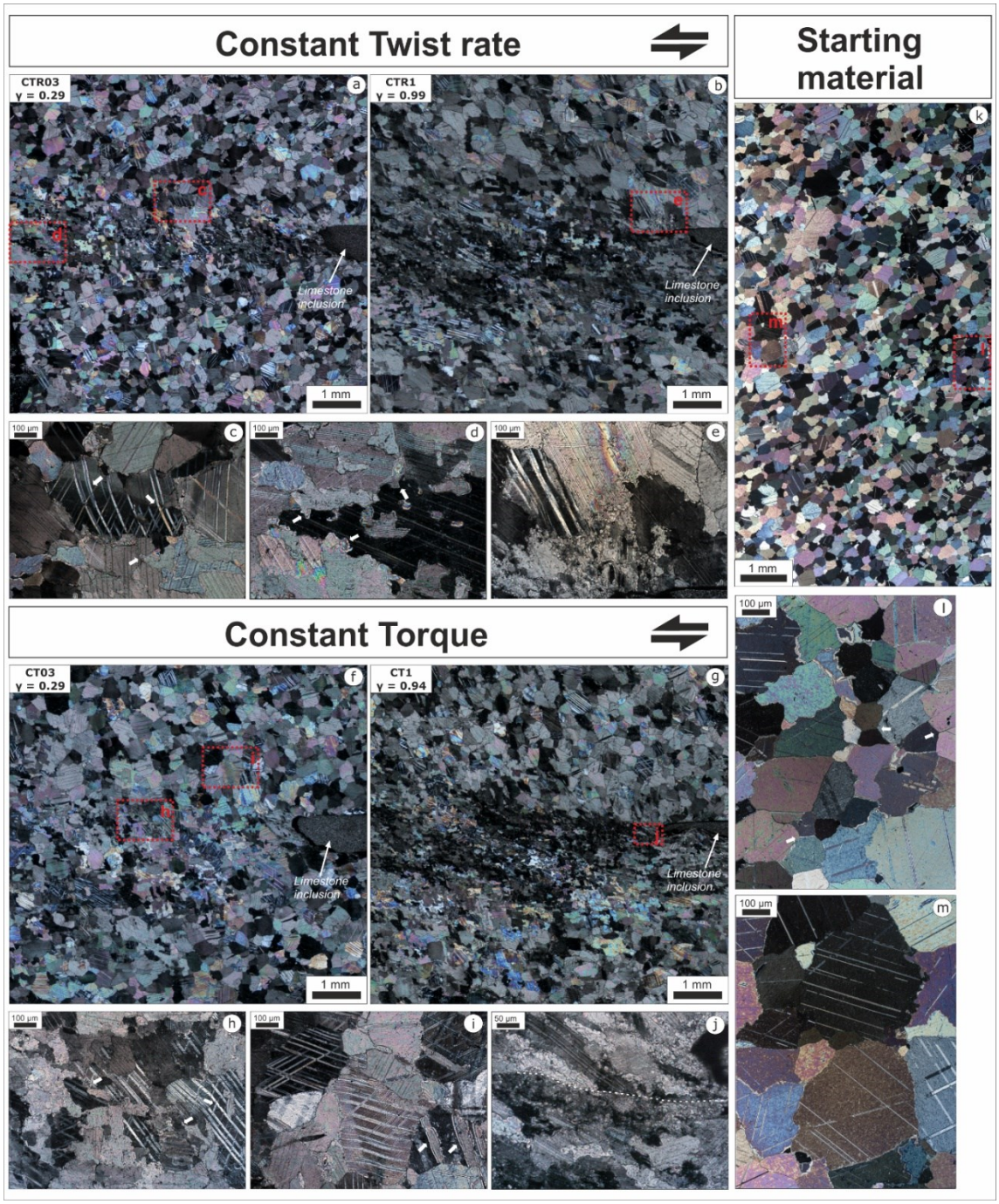

Fig. 7. *a–m: Optical micrographs of 5 thin sections (four from the experimental runs and one from the undeformed starting material), and small insets (c–e, h–j and l,m) displaying details of the microstructures; insets c and d are areas of sample CTR03, e is from sample CTR1, f and g from CT03 and h from CT1. The undeformed starting material displays a homogeneous microstructure with little to no stored strain, large equant grains and abundance of triple junctions (l); twin sets are thin and straight (m). In the overview micrographs of the deformed samples (a–b and f–g), a strongly inhomogeneous distribution of strain can be observed, with the incipient (CTR03 and CT03) and progressive (CTR1 and CT1) formation of an area of intensely localized deformation in front of the inclusion.*

At high strain twinning is less prominent. Grain boundaries are typically sutured and curved indicating grain boundary migration. We observe a shape preferred orientation of the deformed elongate grains resulting in a foliation gently inclined to the shear plane (Fig. 7b and g). Similar to the low strain samples, the main microstructural features are similar in samples deformed in both loading conditions applied to the high strain samples.

Close to the inclusion tip incipient brittle deformation is visible in all samples (Fig. 8). Scanning electron microscope (SEM) images combined with optical close-ups reveal cracks preferentially located at grain boundaries and small voids ahead of the inclusion tip. Small, mostly tensile cracks oriented parallel to the direction of σ_1 are visible in the low strain constant twist rate sample (Fig. 8a–b). In the equivalent strain constant torque sample, a single shear fracture propagating from the tip of the weak limestone inclusion is formed within the host marble (Fig. 8c–d).

Many grain boundaries in the process zone surrounding the inclusion tip are decorated by strings of pores. It is conceivable that these indicate crack closure and healing during the tests. The displacement associated with the shear fracture is accommodated by the weakest phase (the limestone), as can be observed in the relative movement of the ceramic glue at the contact between the marble and the inclusion. At higher bulk strain (Fig. 8e–h), a long single shear fracture is observed in the constant torque sample (Fig. 8g–h). For constant twist rate conditions (Fig. 8e–f) a few small incipient intracrystalline cracks developed at the very tip of the soft inclusion. No substantial offset can be discerned along these small cracks. A large, extended fracture oriented consistently to the direction of σ_1 is seen in this sample, potentially enhanced during unloading given its extension, developing beyond the microstructurally defined process zone.

2.4.4 Grain size and grain shape evolution

The microstructures of the investigated samples vary strongly on the sample scale as a result of the strain partitioning between limestone inclusion and host Carrara marble, and within the marble matrix due to the formation of a shear zone in front of the inclusion. To investigate the distribution of these heterogeneities within samples and between specimens deformed at different conditions we collected EBSD data and performed analysis of grain size distribution and characterized the grain shape evolution (for details on the methods applied, see *section 2.3*). Based on optical observations measuring some tens of recrystallized grains per thin section, average grain size of dynamically recrystallized grains was estimated to 20 ± 4 µm.

2.4.4.1 Grain size evolution

Figs. 9a (low bulk strain samples) and 9b (high bulk strain samples), respectively, show profiles of average grain size plotted against axial distance from the inclusion (above and below; red rectangles in Fig. 9a and b indicate the approximate location of the inclusion). For details on the parameters used for the construction of profiles, see *section 2.3*.

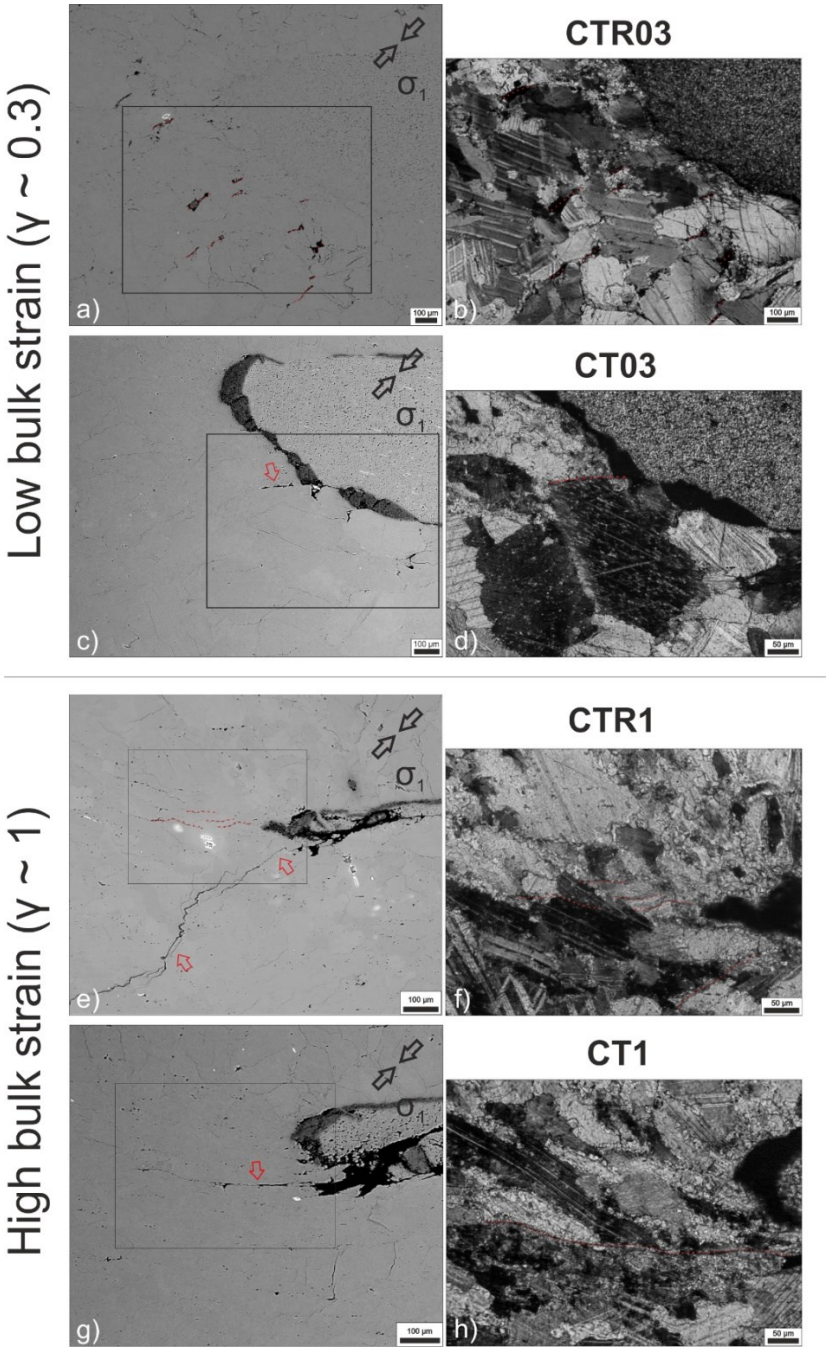

Fig. 8. *a–h: SEM images and optical close-ups of brittle features in the deformed samples for low (a–d) and high (e–h) bulk strain. Applied loading conditions are specified in brackets together with the sample number. The direction of maximum compressive stress, σ_1 is indicated in the upper right corner of the SEM images. The orientation of brittle cracks with respect to the direction of the principal stress is somewhat different at low strain between constant twist rate (a–b) and constant torque (c–d). Note voids that formed ahead of the inclusions (dotted segments in a). Dark seam at inclusion/matrix interface (b) is deformed ceramic cement. Note abundant pores decorating open and closed grain boundaries around the inclusion tip. With increasing bulk strain, similarly oriented fractures are present in both samples, while in the constant twist rate sample (e–f) a single fracture with similar orientation as at lower strain (a–b) is present. Cracks may have been enhanced by unloading at the end of the experimental run.*

Significantly reduced average grain size down to about 60 µm, as a result of intense dynamic recrystallization, is clearly visible in the process zone of all samples. Up to a shear strain of 0.3 a clear symmetry in the average grain size evolution across the process zone is displayed (Fig. 9a). At high strains of about 1 the development of two distinct domains on opposite sides of the inclusion becomes more evident, with lower average grain size values in the lower sector of the samples (Fig. 9b, note the different slopes of the profiles on opposite sides of the inclusion). The applied loading conditions have no significant effect on grain size evolution, suggesting that the amount of recrystallized material associated with localized deformation is not substantially dependent on the imposed boundary conditions.

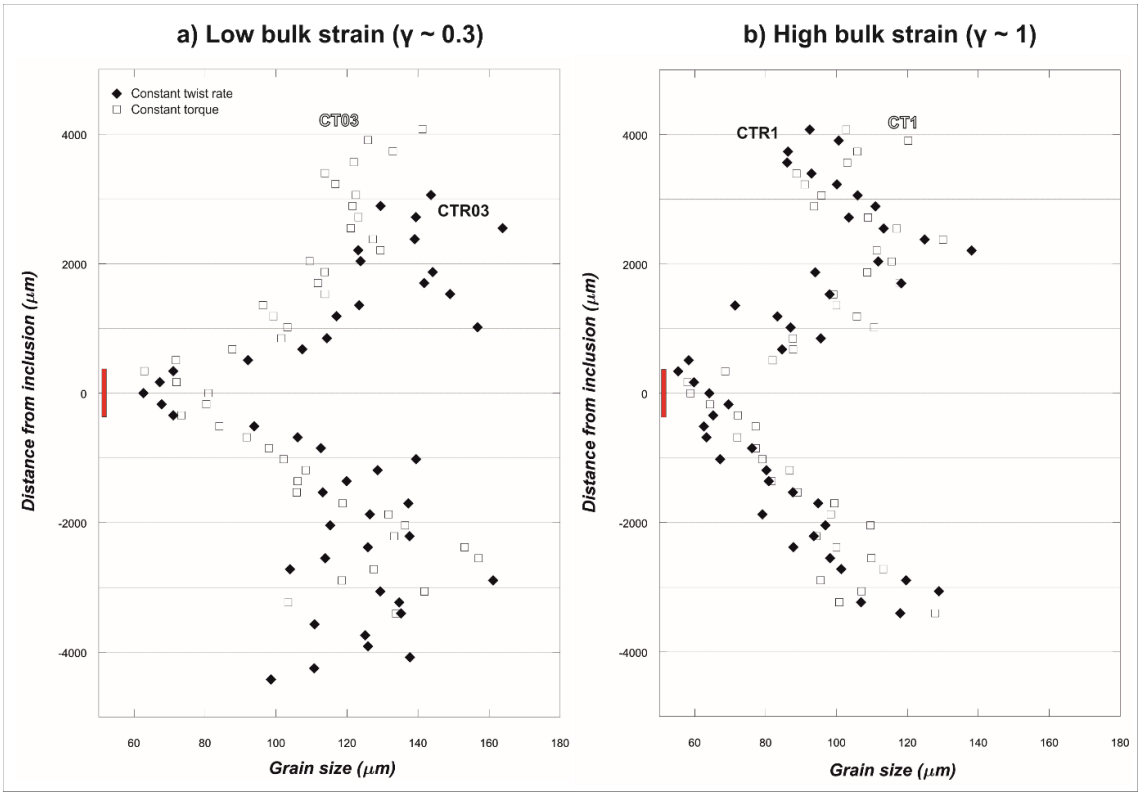

Fig. 9. *a and b: Evolution of average grain size across the thin section, above and below the process zone where deformation localizes in front of the limestone inclusion (the position of the inclusion is indicated in red). a) bulk strain = 0.3; b) bulk strain = 1.*

The finer step size EBSD maps (see *section 2.3*) were used to investigate three regions of the samples in more detail (here referred to as *upper domain*, *process zone* and *lower domain*; Fig. 3a–d). The grain size distributions for all three domains, for the cumulative area of the maps and for the undeformed starting material are shown in terms of area fraction vs equivalent diameter (Fig. 10; diameter of a circle of equivalent area to each grain). Solid, dashed and stippled lines indicate the median values for constant twist rate, constant torque and starting material samples, respectively (see Table 2 for a transcription of the values). For both low and high bulk shear strains the overall grain size distributions

of constant torque and constant twist rate samples within the whole thin section area are largely overlapping with rather similar median values (Fig. 10a and e). In all samples, the average grain sizes are significantly reduced in the process zones compared to adjacent domains and the starting material. Reduction of average grain size outside the process zone is more pronounced at high strain (cf. median lines in Fig. 10h compared to Fig. 10d) as a consequence of the increased contribution of dynamically recrystallized grains.

Table 2. *Median values (in μm) for the area fraction grain size distribution presented in Fig. 10.*

Domain	Low bulk shear strain samples		High bulk shear strain samples		Starting material
	CTR03	CT03	CTR1	CT1	
Whole section	158.52 μm	168.41 μm	134.52 μm	132.55 μm	214.17 μm
Upper domain	183.06 μm	218.44 μm	180.12 μm	163.39 μm	
Process zone	114.77 μm	136.28 μm	115.80 μm	102.14 μm	
Lower domain	169.77 μm	154.44 μm	116.18 μm	137.27 μm	

For low strain samples (Fig. 10b–d) the strongest grain size reduction occurs within the process zone (Fig. 10c), where the applied loading conditions appear to play no role in the resulting distribution. Upper and lower domains (Fig. 10b and d) display some subtle differences in evolution between constant twist rate (CTR03) and constant torque (CT03) samples. For constant twist rate samples, grain size distributions are similar above and below the process zone. Samples deformed at constant torque show a generally lower average grain sizes in the domain below the process zone (Fig. 10d). In general, however, grain size evolutions are very similar in samples deformed at different loading conditions. At high strain, the asymmetry in grain size evolution between the upper and lower domain is preserved (also seen in Fig. 9), but the difference between loading conditions is reduced (Fig. 10f and h). Note, however, that the overall grain size evolution (Fig. 9) and distribution (Fig. 10a and e) ultimately appear not to be influenced by the imposed boundary conditions.

The spatial distribution of dynamically recrystallized grains across the combined three domains (stippled black rectangle in Fig. 3a–d) using 3.5 μm step size maps is plotted in Fig. 11. Bivariate histograms are constructed by defining a 25 × 25 grid colour coded based on how many recrystallized grains (equivalent diameter < 20 μm) are present within each grid square. The frequency of recrystallized grains is largest ahead of the inclusion and increases with increasing bulk strain. No major differences can be observed between the different loading conditions. This is in accordance with the observation that the area fraction of grains with equivalent diameter smaller than 20 μm is similar in samples deformed at both imposed boundary conditions (Fig. 10a and e).

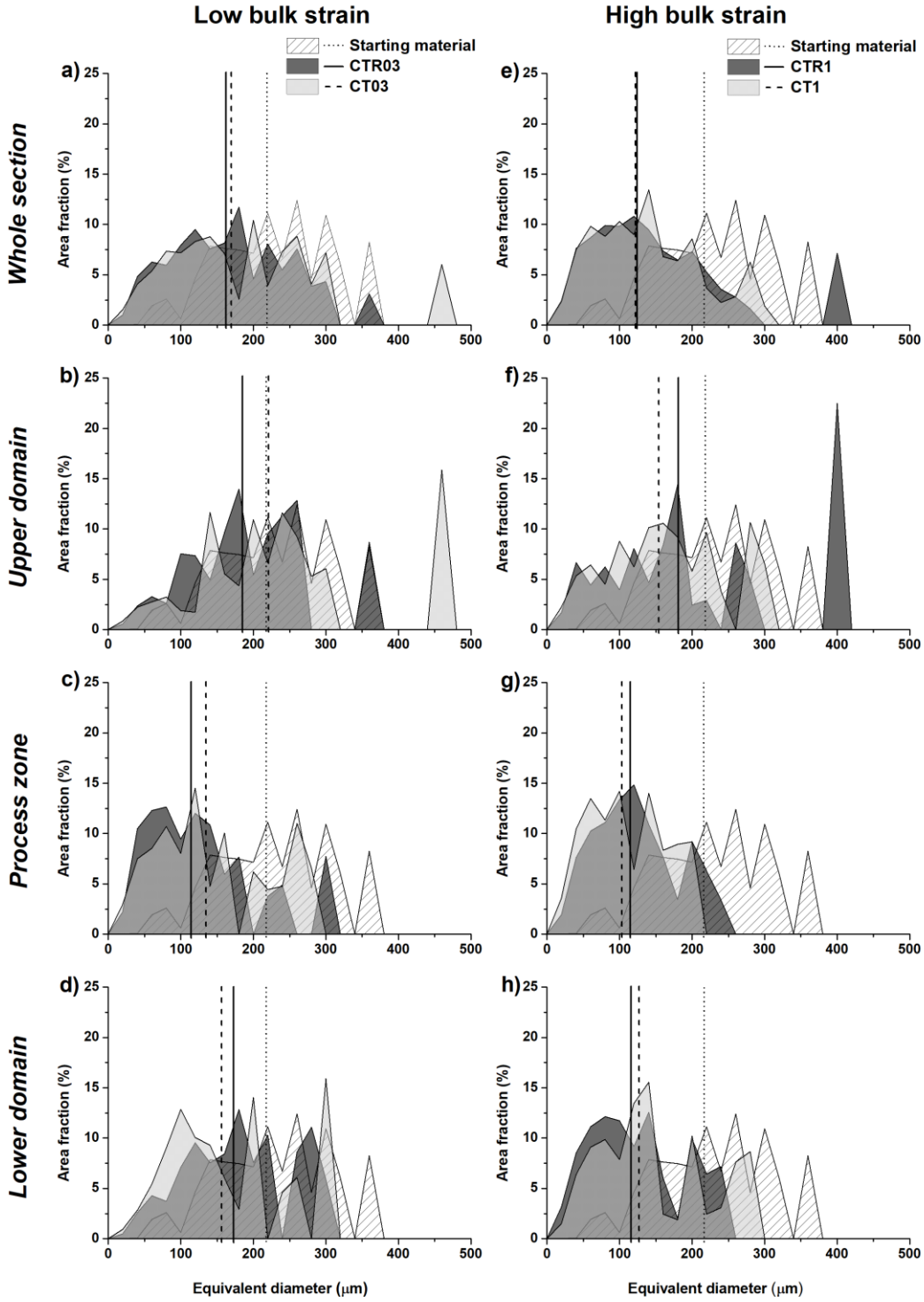

Fig. 10. *a–h: Grain size distribution expressed as normalized area fraction within domains described in text (upper, lower domains and process zone) and for the whole thin section for the two populations of samples (low bulk strain in a–d, high bulk strain in e–h) compared to the starting material. Solid, stippled and dotted lines indicate the median value of grain size distribution for constant twist rate, constant torque samples and undeformed material, respectively. The median grain size in the process zone of all deformed samples is significantly smaller than in adjacent domains and compared to the starting material.*

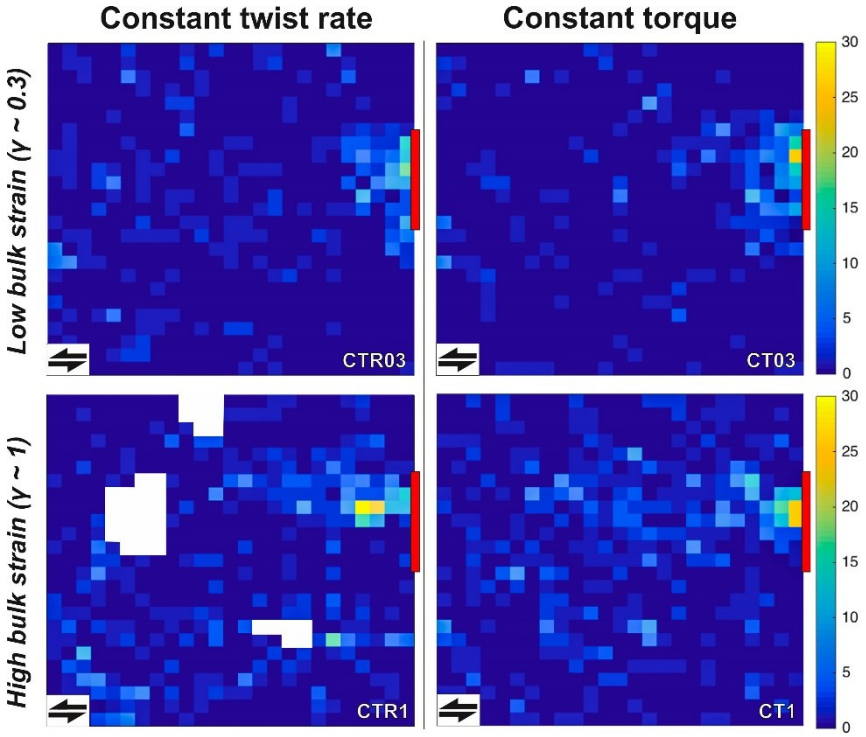

Fig. 11. *Bivariate histograms showing the spatial distribution of small recrystallized grains (eq. diameter < 20 μm) for constant twist rate (left) and constant torque (right) samples. A 25 × 25 grid was defined over the region of interest where the calculation is carried out (black rectangles, Fig. 3a–d); the scale indicates the number of measurements within each unit of the grid. A red bar indicates the approximate position of the inclusion prior to deformation. The white polygons in sample CTR1 correspond to patches of misindexed data (where the thin section was damaged) that were computed as artificial small grains by the mtex toolbox. (For interpretation of the references to colour in this figure legend, the reader is referred to the web version of this article.)*

2.4.4.2 Grain shape evolution

We determined the average grain shape within the aforementioned domains to analyze the degree of plastic deformation of the matrix material (see *section 2.3* for details). In Fig. 12a–l, normalized circularity and inverse aspect ratio data are plotted within the three area domains for the two considered bulk strains (Fig. 12a–f, γ ~0.3 and Fig. 12g–l γ ~1.0; the data is normalized to the total number of grains).

The shape distribution of the starting material (hatched curves) is given for comparison. Vertical lines indicate the median values of each distribution.

The histograms in Figs. 12a–c and 12g–i show the distribution of circularity data, i.e. a measure of the roughness of grain boundaries, at low and high bulk strain, respectively. A comparison of the median values shows that the imposed boundary conditions do not produce a very significant difference in the distribution of circularities within any of the domains considered.

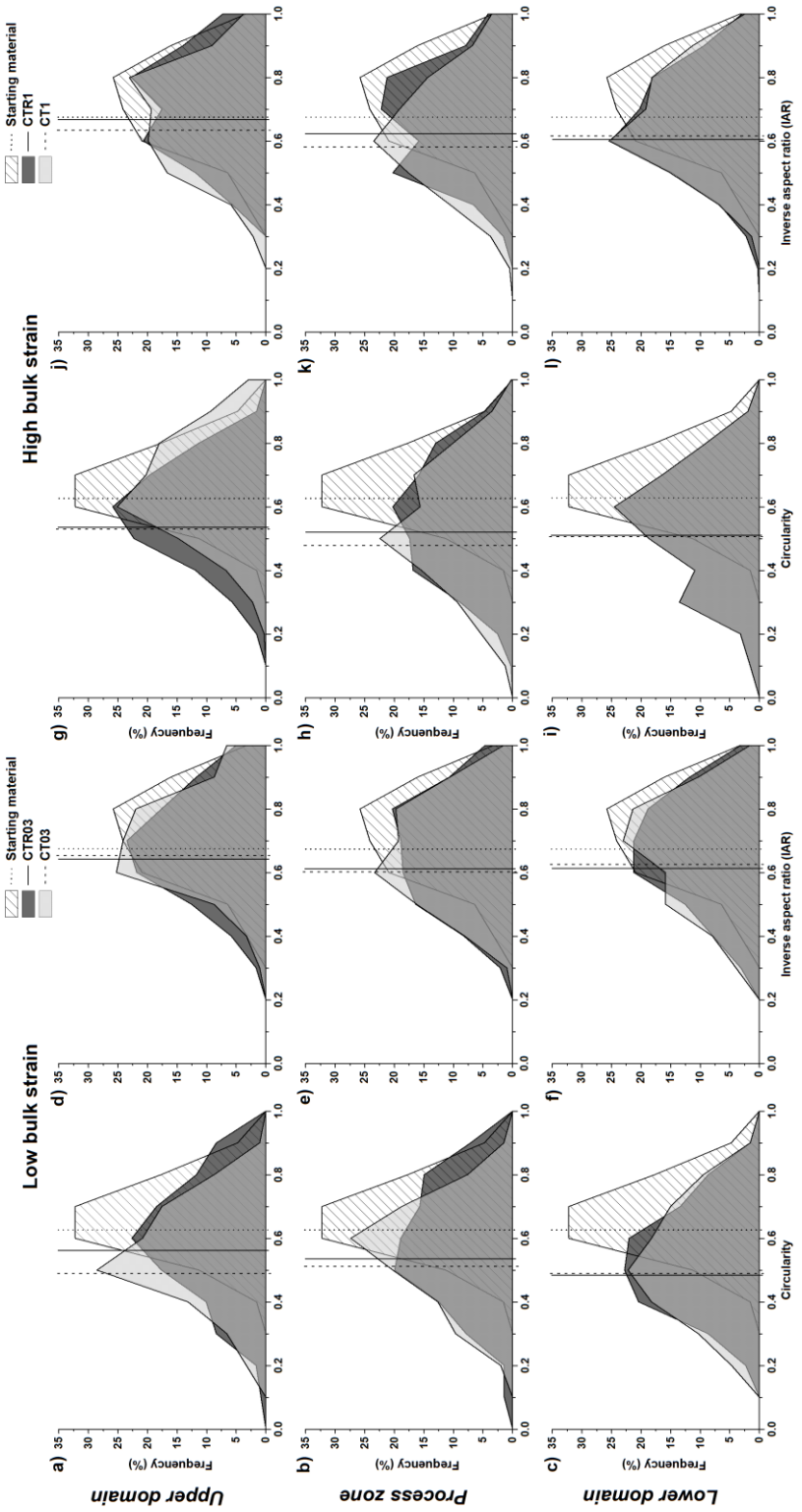

Fig. 12. *a–l: Frequency histograms for the two shape descriptors considered (circularity in a-c and g-i and inverse aspect ratio in d-f and j-l) within the three described domains (upper, lower and process zone) for all samples (low bulk strain in a-f and high bulk strain in g-l) with comparison to starting material distributions. Vertical lines indicate the median value of each distribution. For detailed description see text.*

Compared to the starting material distribution, both constant twist rate (CTR03, CTR1) and constant torque (CT03, CT1) samples show an overall increase in surface roughness (decrease in circularity values) across the entire thin section. The similarities between different boundary conditions are also found for the inverse aspect ratio data, especially at low strains (Fig. 12d–f). Within the general trend of increased ellipticity (decreased inverse aspect ratio) with respect to the starting material distribution, small differences are present in the process zone of high strain samples (Fig. 12k).

2.4.5 Local stress concentration at the tip of the inclusions

The observations carried out on macrostructural and microstructural data indicate that strain is locally concentrated within the Carrara marble in front of the weak Solnhofen inclusion. This suggests that the distribution of stress within the samples is also strongly heterogeneous. Stress appears to be locally enhanced in regions around the inclusion tips that experience the highest amounts of dynamic recrystallization and intracrystalline deformation. Several paleopiezometer techniques may be used to estimate local stresses (e.g. recrystallized grain size, dislocation density, twin density), but they all rest on the assumption that the considered microstructures are in equilibrium with the thermodynamic conditions. On the scale of the entire sample we observe a transient evolution of both strength and microstructure as the shear zone propagates into the Carrara matrix. Although on a local scale (process zone) we may have reached local steady state of stress and microstructure this is not the case for the entire samples considered here. The results presented in the following in terms of recrystallized grain size and dislocation density piezometry are therefore expected to represent lower and upper bounds, respectively, to the true stress values locally experienced by the samples. Recrystallized grains may be larger than the steady state size at the given stress conditions (lower bound), while the density of free dislocations might not be fully reset to the local stress (upper bound).

Calibration of the recrystallized grain size piezometer for Carrara marble has been carried out at different experimental conditions by several authors (Schmid et al., 1980; Rutter, 1995; De Bresser, 1996; Barnhoorn et al., 2004). In this study, we applied the piezometer from Barnhoorn et al., 2004 calibrated on high strain torsion experiments performed between 500 and 700 °C and from Rutter, 1995, who used triaxial compressive and extensional configurations at temperatures between 500 and 1000 °C. The general relationship between stress and recrystallized grain size is given by:

$$\sigma = C \times d^m , \quad (5)$$

where σ is the equivalent stress, d is the recrystallized grain size, and C and m are two constants. Note that the conversion from shear to equivalent stress is defined as follows (Paterson and Olgaard, 2000):

$$\tau = \frac{1}{\sqrt{3}} \sigma. \quad (6)$$

The values of the two constants are 573.03 and -0.82, respectively, calibrated by Barnhoorn et al., 2004 and 812.83 and -0.88 using Rutter's 1995 calibration. Note that both piezometers are based on the assumption that subgrain rotation is the predominant recrystallization mechanism, as is expected from our microstructural observations (see *section 2.4.3*).

For the determination of recrystallized grain sizes within a lateral distance of about 500 µm from the inclusion, between 50 and 100 grains were digitized in each of the samples, and the average of their equivalent diameters was calculated. Results show stress concentration with respect to the applied bulk stress of 2.2–3.1 and 2.9–4.2 using the Barnhoorn and Rutter calibration, respectively (Table 3). Within error in grain size determinations, calculated stress values are independent of bulk finite strain and loading conditions.

Table 3. *Estimated recrystallized grain size and corresponding calculated equivalent stresses. Stress concentration factor = local /bulk stress ratio.*

Sample name	Loading condi-tions	Total imposed bulk strain (γ)	Recrystallized grain size (µm)	Calculated σ (MPa) - Barnhoorn et al., 2004	Stress concent-ration	Calculated σ (MPa) - Rutter, 1995	Stress concent-ration
CTR03	CTR	0.29	10 ± 4	77 ± 30	2.2	100 ± 40	2.9
CT03	CT	0.29	9 ± 3	87 ± 20	2.5	115 ± 30	3.4
CTR1	CTR	0.99	9 ± 3	85 ± 20	2.5	113 ± 30	3.3
CT1	CT	0.94	8 ± 3	101 ± 35	3.1	135 ± 40	4.2

Dislocation densities at increasing distance from the tip of the weak Solnhofen inclusion were estimated using transmission electron microscopy (TEM) of sample CTR03 (low bulk strain constant twist rate). Six foils of 0.15 µm thickness were prepared from areas within relict deformed grains at incremental distances of ~500 µm (Fig. 13a). The foils were examined in STEM mode (scanning transmission electron microscope). Detailed images of each foil were acquired at 5 different tilt angles to highlight the number of visible dislocations. Subsequently, detailed images were stitched together and, by means of a user defined grid, spatial densities of free dislocations (number of dislocations per unit area, i.e. the number of free dislocations that would intersect the linear traverses of the grid) were manually calculated for all the tilt angles considered. Following De Bresser, 1996, the density is defined as:

$$\rho = \frac{2N}{\lambda t}, \qquad (7)$$

where N is the number of intersections, λ the length of the transect line and t the (constant) thickness of the TEM foil.

The piezometer was calibrated by De Bresser, 1996 on both single crystals and polycrystalline calcite deformed between 550–800 °C, yielding:

$$\sigma = 10^{-6.21} \times \rho^{-0.62}, \quad (8)$$

where σ is the equivalent stress in MPa and ρ is the dislocation density in m^{-2}.

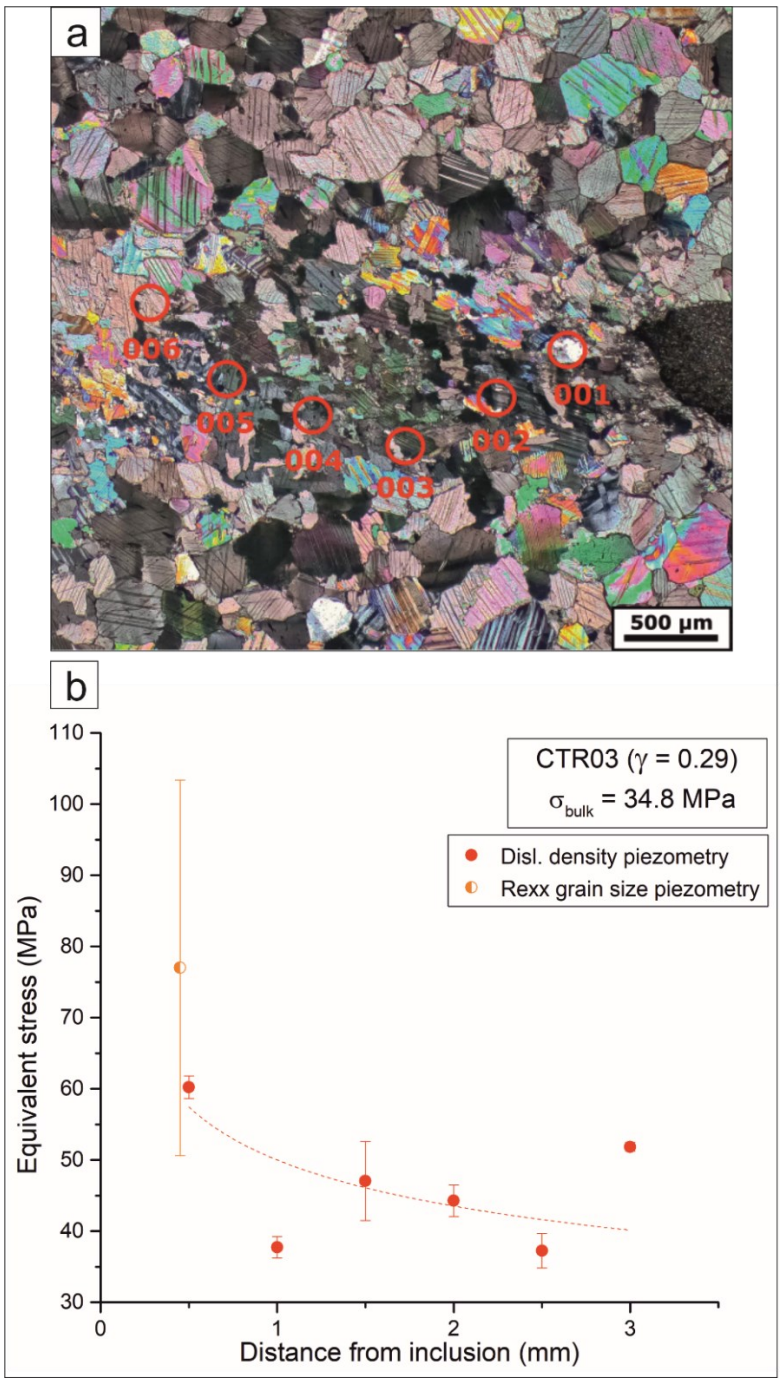

Fig. 13. *a and b: a) Micrograph of sample CTR03 with approximate locations of FIB foils for TEM analysis, b) local stress with distance from the inclusion tip as calculated using dislocation density (red) and recrystallized grain size (orange) piezometry.*

Resulting stresses show significant error bars (as a consequence of the uncertainty in the measured dislocation densities), but decrease non-linearly with distance (Fig. 13b). With respect to the applied bulk equivalent stress of 34.8 MPa, the resulting stress concentration at the tip of the inclusion is approximately a factor 2, in accordance with the results from the recrystallized grain size piezometry.

2.4.6 Crystallographic preferred orientation

For the calculation of pole figures, maps produced with a 10 μm step size were used. A rectangular area of the thin sections covering the process zone was analyzed for all samples. Irrespective of applied loading conditions, a strong CPO developed in the deformed samples with increasing strain. Samples deformed at constant torque and constant twist rate show comparable textural evolution (Fig. 14b–e) and pole figures that differ significantly from the starting material (Fig. 14a).

In CTR03 (low strain constant twist rate sample, Fig. 14b), the [0001] axes are distributed along a rather complete girdle normal to the shear plane and with two maxima at a high angle to the pole of the shear plane. For this sample, an incipient alignment of the poles of {10–14} with the pole of the shear plane is observed, while the poles of {11–20} appear to be quite scattered, with a component parallel to the shear direction.

The {01–12} poles are distributed across two clear maxima at an angle of ~45° to the shear direction. With increasing strain (Fig. 14c), the girdle of [0001] poles becomes more continuous and it cross-cuts the shear plane, also developing a strong maximum around 20° to the shear plane pole. While the {10–14} poles undergo some dispersion, poles of {11–20} strengthen the parallelism to the shear direction. Similarly, {01–12} poles preserve the two described maxima and develop two more, also at ~45° to the shear direction. Poles of {01–18} form small girdles perpendicular to the shear zone, with a maximum concentration at an angle (~15°) to the shear plane pole.

In constant torque samples (Fig. 14d–e), CT03 presents a weak texture similar to the low strain, constant twist rate experiment. Poles of [0001] display a weak girdle with a maximum at about 30° from the center of the pole figure within the shear reference plane and two incipient weak maxima oblique (~45°) to the shear plane and opposite the shear direction are also visible. The poles to {10–14} and {11–20} planes are rather dispersed, although these latter display maxima normal and at ~45° to the shear plane. Poles of {01–12} are again arranged in four symmetrical maxima at ~45° to shear direction, with the addition of further maxima normal and sub-parallel to the shear plane. With increasing strain (Fig. 14e), the CPO strengthens substantially, similar to the sample deformed at constant twist rate. Poles of [0001] are now arranged in one single girdle normal to the shear plane, with one dominant maximum at ~20° to the poles of the shear plane. The {10–14} poles show an alignment parallel to the shear plane, while the poles of {11–20} seem to follow the shear direction. Poles of {01–12} are arranged in four symmetrical maxima as described for the constant twist rate sample. A strong preferred orientation is observed for {01–18} poles as well, forming girdles around the normal to the shear plane.

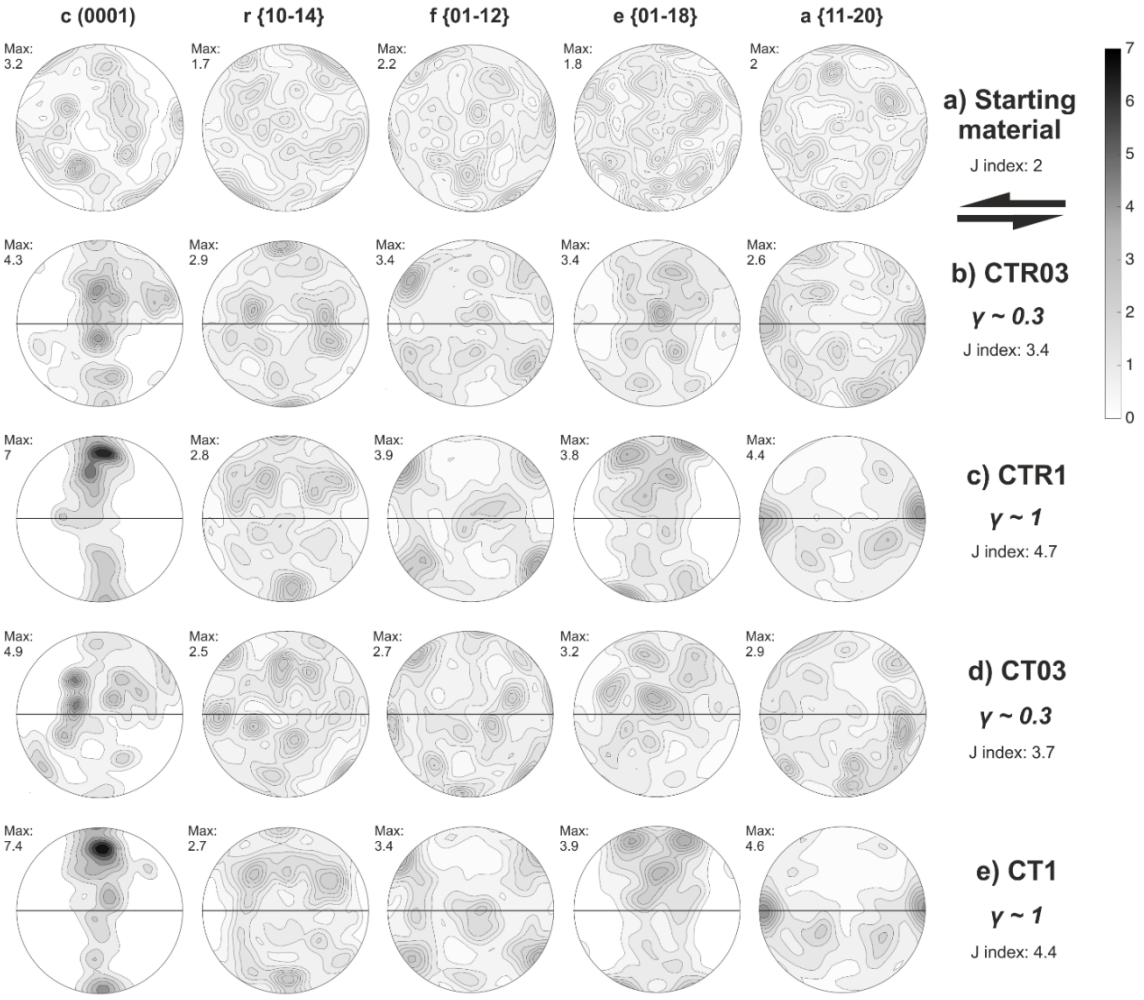

Fig. 14. *a–e: Crystallographic preferred orientation of calcite in Carrara marble a) from the undeformed sample or b-e) within the process zone of the experimental samples (as defined in Fig. 3a–d), for the poles of basal (c (0001)), rhomb (r {10–14}, f {01–12}), (e {01–18}) and prismatic (a {11–20}) planes. Orientation of shear plane is indicated by arrows at the top right of the figure.*

2.5 Discussion

2.5.1 Weakening mechanisms

Plastic strain localization requires the development of an instability in the system undergoing deformation (Poirier, 1980; Hobbs et al., 1990). It is generally assumed that potentially coexisting weakening mechanisms (recrystallization-induced grain size reduction, CPO formation, reaction softening, shear heating) may lead to local strength perturbations and ultimately to strain localization (for a review, see Fossen and Cavalcante, 2017).

At the given experimental conditions, Carrara marble is expected to deform in the dislocation creep regime (e.g. Schmid et al., 1987; Pieri et al., 2001a, b; Rybacki et al., 2014). This assumption is confirmed by the observed presence of a strong

crystallographic preferred orientation even at early increments of bulk shear strain (Fig. 14). Moreover, the increased mean aspect ratio of relict grains with respect to the undeformed starting material (Fig. 15a–b) associated with the development of a SPO within the process zone of the investigated samples (Fig. 15c–d) are indicative of intracrystalline deformation.

Intense, strain dependent grain size reduction by dynamic recrystallization is observed to develop dominantly in the process zone (Fig. 11), induced by the concentration of stresses and shear strain around the inclusion tip (Fig. 13). Some contribution of grain size sensitive diffusion creep is expected to be active in fine-grained regions in Carrara marble, as shown for the same experimental conditions and for recrystallized grain sizes in the order of 10–15 μm (ref. Fig. 13 in Rybacki et al., 2014). As discussed by the latter authors, the measured stress concentration at the tip of the inclusion may induce switching into the dislocation creep regime, suggesting that the deformation mechanism in Carrara marble leading to weakening at the examined experimental conditions is grain size insensitive. This is supported by our observations indicating formation of cracks at the inclusion tip.

The textural data (Fig. 14) allows identifying possible slip systems activated in the process zone of the samples, based on the classification of slip systems operating in calcite deformed at high temperature (e.g. De Bresser and Spiers, 1993). A general trend of switching main slip systems with increasing strain is observed in both constant twist rate and constant torque samples. Basal slip (notice the strong alignment of c-poles in Fig. 14c, e) is prevalent in both the high bulk strain samples, together with remnants of slip along the rhomb r plane in the a-direction {10–14} <20–21>. The low strain samples show a weaker texture, mainly due to slip along the rhomb r{10–14} and f{01–12} planes in the a<20–21> direction (Fig. 14b, d). Strengths of the texture within the process zone, as quantified by the calculated j-index (Bunge, 1982), are similar for constant twist rate and constant torque samples at similar bulk strains. Pole figures are in good agreement with observations on calcite at similar conditions in previous studies (Schmid et al., 1987; Pieri et al., 2001a, b; Barnhoorn et al., 2004; Rybacki et al., 2014). The activity of similar slip systems and the analogous degree of textural development as a function of finite strain in our samples suggests that the deformation mechanisms active in the process zone are independent of applied loading conditions.

All deformed samples show cracks at the inclusion tips (Fig. 8a–h). Cracks mostly follow grain boundaries and some open fractures are oriented parallel to the maximum compressive stress. Although some microcracks may have been induced by cooling and unloading, voids, low aspect ratio cracks and healed cracks clearly formed during the tests. Locally, where stresses are concentrated, brittle deformation assists in reducing grain size as described in natural examples of crustal scale shear zone networks (Fusseis et al., 2006; Fusseis and Handy, 2008). The microstructural observations show that brittle fracturing even occurs in combination with plastic deformation of calcite (Fig. 8).

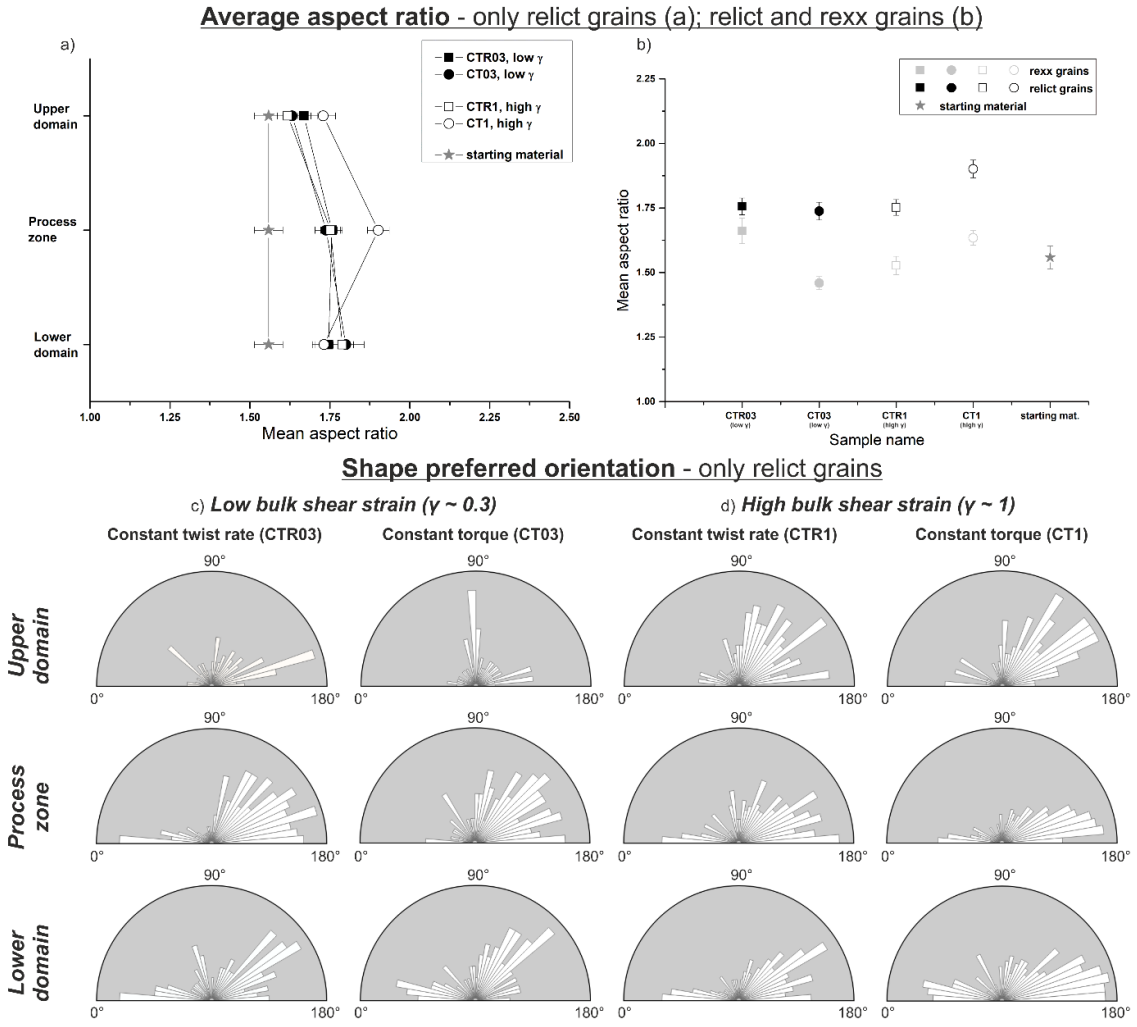

Fig. 15. *a–d: (a) Analysis of mean aspect ratio of relict grains (equivalent diameter > 20 µm) across the vertical profiles defined in Fig. 2a–d; (b) comparison of mean aspect ratios of relict (eq diam. > 20 µm) and recrystallized (eq. diam. < 20 µm) grains within the process zone of the samples; (c, d) shape preferred orientation of relict grains (eq. diam. > 20 µm) across the vertical profiles defined in Fig. 2a–d.*

As the process zone propagates into the Carrara marble matrix, cracking is overprinted by high-temperature creep of the fine-grained recrystallized matrix assisted by crack healing. It is conceivable that some of the cracking is also obliterated during unloading and slow cooling of the samples at the end of the experimental runs.

In CTR samples (Fig. 8a–b and e–f), microcracks and voids display a somewhat different distribution and orientation with respect to constant torque samples. At low strain, a set of small (50–100 µm) cracks is found, most that are oriented parallel to the direction of σ_1 (Fig. 8a–b). Most of these cracks are open and appear to be tensile in nature while others are associated with small, dynamically recrystallized material. At higher bulk shear strains (Fig. 8e–f), some intracrystalline microcracks occur in parallel to the maximum shear direction, together with a long interconnected fracture parallel to σ_1. In both

constant torque experiments (Fig. 8c–d and g–h), a single fracture forms in plane with the shear propagation direction from the tip of the inclusion, consistent with the far field direction of maximum shear stress. It is, in all cases, difficult to assess with certainty whether any displacement occurred along these fractures, as the presence of fine recrystallized material related to the ongoing plastic deformation overprints any possible passive marker in the microstructure. The preservation of such a fracture in both low and high bulk strain sample suggests its formation in the early stages of deformation and its further exploitation with increasing strain. Brittle deformation, in all samples, appears to be confined to small domains (where local stresses and strain rates are highest) and small intervals of strain, associated with pervasive high-temperature creep of calcite.

2.5.2 Stress distribution and deformation transients

The heterogeneous stress distribution produced in the matrix due to the presence of an inclusion is clearly expressed in the resulting microstructures. The stress enhancement in the marble matrix in the process zone in front of the inclusion tip is substantial and has been quantified to a factor of 1.5–3 with respect to the applied bulk stress (Table 3, Fig. 13), although it should be borne in mind that the paleopiezometers applied here were calibrated for steady state conditions not achieved in our tests (Rutter, 1995; De Bresser, 1996; Barnhoorn et al., 2004). Note that the amount of stress concentration surrounding a material heterogeneity depends on the effective viscosity contrast between inclusion and matrix and on coupling of the two materials (Kenkmann and Dresen, 1998). At given thermodynamic conditions of our tests, the initial viscosity contrast between Carrara marble and Solnhofen limestone is expected to be a factor ~10 (Rybacki et al., 2014). As suggested by the local shear strain, stress and grain size distributions found in the process zone, an exponential decay is observed with distance from the inclusion towards the matrix.

The time-dependent strain localisation pattern can be additionally investigated using numerical forward models (Döhmann et al., 2018 and Fig. 16). Here we employ 2D Cartesian models with periodic boundary conditions that have been benchmarked to experimental mechanical data. The gradient in flow stress reconstructed for sample CTR03 (Fig. 13) by means of dislocation density piezometry is in general accordance with results from numerical models (Fig. 16). In their study, Döhmann et al., 2018 found a rapid stress drop, down to roughly far-field levels, within 2–3 mm from the inclusion tip. Numerical modelling was carried out by means of the geodynamic modelling software SLIM3D (Semi-Lagrangian Implicit Model for 3 Dimensions, Popov and Sobolev, 2008), which was originally intended for the study of lithospheric-scale processes (Brune, 2016) but has been applied to laboratory scale localization models as well (Cyprych et al., 2016). For the applied thermodynamically coupled conservation equations, see Popov and Sobolev, 2008. Experimentally derived (Schmid et al., 1980 and Rybacki et al., 2014) flow laws were used to model deformation of Carrara marble and Solnhofen limestone, and a strain-dependent viscous softening mechanism was implemented (Brune et al., 2014).

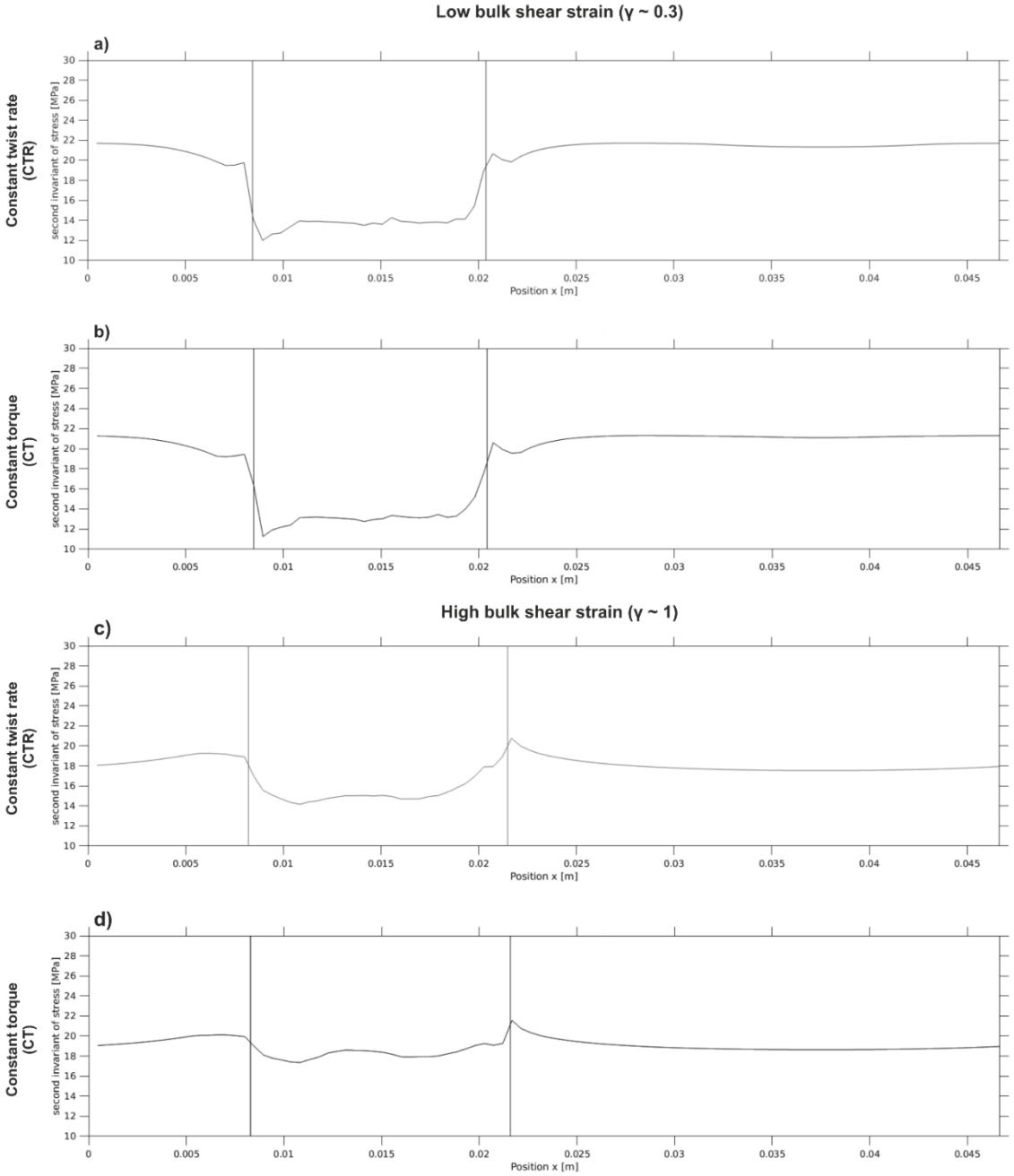

Fig. 16. *A–d: Results of a modelling study assuming material parameters and experimental conditions as in the tests (Döhmann et al., 2018). The profiles of the second invariant of stress are plotted across the outer surface of the sample cylinders; vertical lines are indicating the position of the Solnhofen limestone inclusion at the final bulk shear strain for low strain (a, b) and high strain (c, d). Note low shear stresses within the inclusion and stress maxima at the inclusion tips.*

Model-derived profiles of the second invariant of stress along the inclusion and process zone at the cylinders' outer surface show local stress concentration at the inclusion tip decaying towards the matrix (Fig. 16). Stress concentration is significantly smaller than observed in the deformed samples but the general trend agrees with experimental results.

For example, a nonlinear stress decay is observed with increasing distance from the inclusion towards the matrix irrespective of loading conditions. The enhanced strain induced in the marble by the applied higher stresses leads to a progressive stress relaxation along the process zone (compare Fig. 16a and c for constant twist rate and 16b and d for constant torque experiments). Note that a stress peak at the inclusion tip is preserved in all cases, regardless of total strain (Table 3 and Fig. 16), as the viscosity contrast between the inclusion and the matrix surrounding it is still high. Fig. 16 also shows little difference in the shape and magnitude of the area of enhanced stress.

The paleowattmeter introduced by Austin and Evans, (2007) allows grain size of dynamically recrystallized material to be related to mechanical work rather than to flow stress alone. We applied the suggested scaling relationship (Eqs. 8, 9 in Austin and Evans, 2007) to our data. Using the measured grain sizes listed in Table 3 and the values of local strain rates derived from the strain markers (see *section 2.4.2*), the predicted concentration in stresses with respect to the far field equivalent stress is in the range 3–5, in good agreement with the paleopiezometric estimates (factors 2–4, depending on calibration, Table 3). The approach may also be used to predict the average recrystallized grain size for given differential stresses and strain rates. Resulting recrystallized grain sizes vary between 10 and 12 μm (far field stress) and 8–10 μm (up to a factor 4 stress concentration, the upper bound derived from paleopiezometry), in accordance to what is measured optically in the samples (Table 3). Taking into account the uncertainty of measured grain sizes and strain rates, we conclude that our experiments do not allow us to determine if the wattmeter yields more reliable results than the piezometer.

2.5.3 Amount and geometry of strain localization

Strain localization as indicated by strain markers increased as the process zone propagated into the Carrara matrix (Fig. 6a, b). However, localization remained unaffected by the different loading conditions. Within the process zone at low bulk strains Carrara marble is strongly twinned: thick, often tapered or bent twins are abundant, as are multiple twin sets within single crystals. Deformation twinning in calcite has been extensively studied in the past (e.g. Barber and Wenk, 1979; Wenk, 1985), and twin morphology and intensity (number of twins per mm) are often used as stress-strain indicators (paleopiezometers) during low grade metamorphism (Ferrill, 1991; Ferrill et al., 2004; Rybacki et al., 2013 and Burkhard, 1993 for a review). At low temperatures and low stress, twinning on the e-plane {01–18} may accommodate strain until hardening sets in due to the activity of only one independent slip system (Burkhard, 1993). At higher temperatures, dynamic recovery processes accommodate strain as observed in the high strain samples, CTR1 and CT1. Qualitatively, the morphology and distribution of twin sets do not display substantial differences between samples deformed at different loading conditions. Other microstructural expressions of localized viscous deformation in the process zone have been extensively presented (*sections 2.4.3* and 2.*4.4*): little variation is noted for constant stress and constant strain rate samples. Strain partitioning into the process zone is clearly recognizable at low bulk strains of $\gamma \sim 0.3$ and continues progressively with increasing

shear strain irrespective of loading conditions (Fig 6b). Once weakening is completed with progressive strain, partitioning of shear strain into the localized shear zone saturates at a constant shear strain ratio between shear zone and bulk sample (Fig.6a). The slope in Fig. 6a defines the critical shear strain γ_c required to complete weakening at a critical length of the process zone. Process zone length and shear strain gradient depend on viscosity contrast between the strong host rock and weak shear zone, and the weakening mechanism(s).

2.5.4 Comparison to previous experimental work

High temperature experimental deformation has been conducted extensively on rock-forming minerals to reproduce the processes occurring in natural shear zones. Since the introduction of the torsion setup in the Paterson gas deformation apparatus, a number of large strain studies have been performed on monophase materials, such as olivine (e.g. Bystricky et al., 2000; Hansen et al., 2012), calcite (Casey et al., 1998; Pieri et al., 2001a, b; Barnhoorn et al., 2004), quartz (e.g. Schmocker et al., 2003) or on multi-phase aggregates (e.g. Rybacki et al., 2003; Barnhoorn et al., 2005; Dimanov & Dresen, 2005; Holyoke & Tullis, 2006). Notably, although mechanical weakening of the deforming materials was described in all cases, localization of deformation at the sample scale was only observed in a small number of these studies, where it appeared to be favoured, e.g. by high initial strength contrast between phases (Holyoke and Tullis, 2006), by a switch in deformation mechanism in only one of the deforming phases, producing locally heterogeneous phase distribution (Barnhoorn et al., 2005) or in the case of imposed constant load (torque) boundary conditions (Hansen et al., 2012). This latter is in good agreement with what was theoretically predicted for the torsion geometry by several authors (Fressengeas and Molinari, 1987; Leroy and Molinari, 1992; Paterson, 2007) who, by means of linearized perturbation analysis, prescribe strain localization to be dependent on the applied boundary conditions. A small enough perturbation of one of the material properties is not expected to produce localization in a constant displacement rate setting even if strain weakening is observed, as opposed to a constant load setup in which localization is always favored. However, the linear perturbation analysis of Fressengeas and Molinari (1987**)** is carried out with the assumption that deviations from homogeneity of the material properties are small. For larger perturbations the field equations cannot be linearized and the analytical solutions are much more complex. We argue that, in our experimental setting, the initial departure from a homogeneous stress distribution imposed by the presence of a strong viscosity contrast is much larger than can be treated by the linear approximation. As a consequence, it can be inferred that, for bi- or multi-phase materials with sufficient viscosity contrast (as is often the case in nature), the expected influence of boundary conditions on localization is absent or minor.

2.5.5 Implications for natural shear zones

Our study shows that, in the presence of a material heterogeneity in an otherwise homogeneous medium, localized shear zones form regardless of the imposed loading

conditions. Recent theoretical studies accompanied by integration of existing field data (Whipple Mountains core complex, southeast California; Platt and Behr, 2011a and Platt and Behr, 2011c) propose a theory for the development of viscous shear zone in the middle to lower crust in a stress-controlled environment. The authors concluded that the yield stress of the undeformed host rock controls the flow stress in the deforming shear zone. Consequently, a constant velocity boundary condition is always converted into a constant stress condition. However, the theory is based on the assumption of steady-state deformation of a homogeneous crustal material. This premise seems to apply to a limited number of tectonic situations, but may not apply to channel flow (Beaumont et al., 2004) or the dynamic feedback between the brittle upper crust and the semibrittle to ductile lower crust during syn- and inter-seismic periods (Trepmann and Stöckhert, 2003). In their review paper on shear zones in the mantle, Vauchez et al. (2012) argue that the yield stress of a rock is strain rate dependent, where the strain rate itself is a function of shear zone width; thus stress cannot be constant. Numerous field and experimental studies conducted in the past decades have identified a number of mechanisms that are believed to trigger strain localization at the crustal scale. Most of these involve some form of inherited presence of a rheological or structural heterogeneity, or the mentioned interaction with the seismogenic crust (for a review, see Vauchez et al., 2012). Our results suggest that a rheological heterogeneity will initiate shear zone formation with little impact of the applied boundary conditions.

2.6 Conclusions

We conducted high temperature torsion experiments to investigate the effect of loading conditions (constant twist rate or constant torque) on the initial and transient stages of strain localization in marble containing a weak material heterogeneity. The inclusion induced stress concentration halos in the stronger surrounding matrix resulted in strain partitioning into localized shear bands propagating into the marble with ongoing bulk deformation. Progressive localization is associated with strain weakening accommodated by dynamic recrystallization, CPO development and plastic deformation of relict grains within a process zone which is markedly different from the surrounding, relatively intact matrix. High temperature creep of marble is the dominant deformation mechanism at the applied experimental conditions, although evidence for coexisting brittle deformation is found regardless of loading conditions and total strain. This latter observation is of particular interest, as it is a feature that is frequently recognized in nature where the presence of fractures and veins associated with localized ductile deformation is often interpreted as the necessary precursor to localization (e.g. Mancktelow and Pennacchioni, 2005) or as the expression of coexisting brittle and ductile deformation (e.g. Badertscher and Burkhard, 2002; Ebert et al., 2007; Poulet et al., 2014). Overall, we observe that the geometry, microstructural and textural features and evolution of the process zone are qualitatively and quantitatively comparable in constant torque and constant twist rate experiments.

Our results suggest that the loading conditions do not significantly affect strain localization induced by the presence of a material heterogeneity during nucleation and transient evolution stages.

It should be kept in mind that the experimental setup poses some intrinsic limitations on the number of variables that can be investigated simultaneously. The effects that some of the latter (as the applied confining pressure, temperature or the presence of a second phase in the deforming matrix) might have on the weakening mechanisms and ultimately on the processes favouring strain localization are manifold and would require further investigation and a multidisciplinary approach (with experimental, field based and model based studies).

Acknowledgements

We are grateful to Stefan Gehrmann for the preparation of experimental samples and thin sections. Further thanks are given to Anja Schreiber for FIB-foil cutting and Dr. Richard Wirth for the invaluable help with TEM analysis. Dr. Luca Menegon is gratefully thanked for fruitful discussion on the manuscript and the project in general. This manuscript was greatly improved by the thorough and constructive reviews of Marco Herwegh and Andreas Kronenberg, and comments from Editor-in-chief Kelin Wang. This project was founded by DFG grant GR 4468/2. M.D. and S.B. have been funded through the Helmholtz Young Investigators Group CRYSTALS (VH-NG-1132).

References

Austin, N. J., & Evans, B. (2007). Paleowattmeters: A scaling relation for dynamically recrystallized grain size. *Geology*, *35*(4), 343–346. ISSN 0091-7613, http://dx.doi.org/10.1130/G23244A.1

Bachmann, F., Hielscher, R., Schaeben, H. (2010). Texture Analysis with MTEX – Free and Open Source Software Toolbox, In *Solid State Phenomena*, 160, 63–68, ISSN 1662-9779, http://doi.org/10.4028/www.scientific.net/SSP.160.63

Badertscher, N. P., Burkhard, M. (2000). Brittle–ductile deformation in the Glarus thrust Lochseiten (LK) calc-mylonite. *Terra Nova*, *12*(6), 281–288. https://doi.org/10.1046/j.1365-3121.2000.00310.x

Barber, D. J., Wenk, H. R (1979). Deformation twinning in calcite, dolomite and other rhombohedral carbonates, In *Physics and Chemistry of Minerals*, 5(2), 141-165, ISSN 1432-2021, https://doi.org/10.1007/BF00307550

Barnhoorn, A., Bystricky, M., Burlini, L., Kunze, K. (2004). The role of recrystallisation on the deformation behaviour of calcite rocks: large strain torsion experiments on Carrara marble, In *Journal of Structural Geology*, *26*(5), 885–903, ISSN 0191-8141, https://doi.org/10.1016/j.jsg.2003.11.024

Barnhoorn, A., Bystricky, M., Kunze, K, Burlini, L., Burg, J.-P. (2005) Strain localisation in bimineralic rocks: Experimental deformation of synthetic calcite–anhydrite aggregates, *Earth and Planetary Science Letters*, *240*(3–4), 748–763, ISSN 0012-821X, https://doi.org/10.1016/j.epsl.2005.09.014

C. Beaumont, R. A. Jamieson, M. H. Nguyen, S. Medvedev, Crustal channel flows: 1. Numerical models with applications to the tectonics of the Himalayan-Tibetan orogeny, In Journal of Geophysical Research: Solid Earth, Volume 109, Issue B6, 2004 ISSN 0148-0227, https://doi.org/10.1029/2003JB002809

Beaumont, C., Jamieson, R.A., Nguyen, M.H., Medvedev, S., 2004. Crustal channel flows: 1. Numerical models with applications to the tectonics of the Himalayan-Tibetan orogeny. J. Geophys. Res. Solid Earth 109 (B6), ISSN 0148-0227, https://doi.org/10.1029/2003JB002809

Bercovici, D., 1996. Plate generation in a simple model of lithosphere-mantle flow with dynamic self-lubrication. Earth Planet. Sci. Lett. 144 (1–2), 41–51. ISSN 0012-821X. https://doi.org/10.1016/0012-821X(96)00140-9

Bercovici, D., 1998. Generation of plate tectonics from lithosphere–mantle flow and void–volatile self-lubrication. Earth Planet. Sci. Lett. 154 (1–4), 139–151. ISSN 0012- 821X. https://doi.org/10.1016/S0012-821X(97)00182-9

Bercovici, D., 2003. The generation of plate tectonics from mantle convection. Earth Planet. Sci. Lett. 205 (3–4), 107–121. ISSN 0012-821X. https://doi.org/10.1016/ S0012-821X(02)01009-9

Bercovici, D., Karato, S.-I., 2002. Theoretical analysis of shear localization in the lithosphere. Rev. Mineral. Geochem. 51 (1), 387–420. ISSN 1529-6466. https://doi.org/10.2138/gsrmg.51.1.387.

Bestmann, M., Kunze, K., Matthews, A., 2000. Evolution of a calcite marble shear zone complex on Thassos Island, Greece: microstructural and textural fabrics and their kinematic significance. J. Struct. Geol. 22 (11–12), 1789–1807. ISSN 0191-8141. https://doi.org/10.1016/S0191-8141(00)00112-7

Brune, S., 2016. Rifts and rifted margins: a review of geodynamic processes and natural hazards. In: Duarte, J.C., Schellart, W.P. (Eds.), Plate Boundaries and Natural Hazards. Geophysical Monograph Series 219. pp. 11–37. https://doi.org/10.1002/9781119054146.ch2

Brune, S., Heine, C., Pérez-Gussinyé, M., Sobolev, S.V., 2014. Rift migration explains continental margin asymmetry and crustal hyper-extension. Nat. Commun. 5, 4014. https://doi.org/10.1038/ncomms5014

Bunge, H., 1982. Texture Analysis in Material Sciences: Mathematical Methods. Butterworths, London, pp. 593.

Burkhard, M., 1993. Calcite twins, their geometry, appearance and significance as stressstrain markers and indicators of tectonic regime: a review. J. Struct. Geol. 15 (3–5), 351–368. ISSN 0191-8141. https://doi.org/10.1016/0191-8141(93)90132-T.

Burlini, L., Bruhn, D., 2005. High-strain zones: laboratory perspectives on strain softening during ductile deformation. Geol. Soc. Lond., Spec. Publ. 245 ISSN 2041-4927. http://sp.lyellcollection.org/content/245/1/1.

Bystricky, M., Kunze, K., Burlini, L., Burg, J.-P., 2000. High shear strain of olivine aggregates: rheological and seismic consequences. Science 290 (5496), 1564–1567. ISSN 1095-9203. http://science.sciencemag.org/content/290/5496/1564.

Holyoke, Caleb W., Tullis, Jan, 2006. Mechanisms of weak phase interconnection and the effects of phase strength contrast on fabric development. J. Struct. Geol. (0191-8141) 28 (4), 621–640. https://doi.org/10.1016/j.jsg.2006.01.008

Casey, M., Kunze, K., Olgaard, D.L., 1998. Texture of Solnhofen limestone deformed to high strains in torsion. J. Struct. Geol. 20 (2–3), 255–267. ISSN 0191-8141. https://doi.org/10.1016/S0191-8141(97)00058-8

Cyprych, D., Brune, S., Piazolo, S., Quinteros, J., 2016. Strain localization in polycrystalline material with second phase particles: Numerical modelling with application to ice mixtures. Geochem. Geophys. Geosyst. 17 (9), 3608–3628. ISSN 1525-2027. https://doi.org/10.1002/2016GC006471

De Bresser, J.H.P., 1996. Steady state dislocation densities in experimentally deformed calcite materials: Single crystals versus polycrystals. J. Geophys. Res. Solid Earth 101 (B10), 22189–22201. ISSN 2156-2202. https://doi.org/10.1029/96JB01759

De Bresser, J.H.P., Spiers, C.J., 1993. Slip systems in calcite single crystals deformed at 300–800 °C. J. Geophys. Res. Solid Earth 98 (B4), 6397–6409. ISSN 0148-0227. https://doi.org/10.1029/92JB02044

De Bresser, J.H.P., Urai, J.L., Olgaard, D.L., 2005. Effect of water on the strength and microstructure of Carrara marble axially compressed at high temperature. J. Struct. Geol. 27 (2), 265–281. ISSN 0191-8141. https://doi.org/10.1016/j.jsg.2004.10.002.

Dimanov, A., Dresen, G., 2005. Rheology of synthetic anorthite-diopside aggregates: Implications for ductile shear zones. J. Geophys. Res. Solid Earth (J. Geophys. Res.) (0148-0227) 110 (B7). https://doi.org/10.1029/2004JB003431

Dimanov, A., Rybacki, E., Wirth, R., Dresen, G., 2007. Creep and strain-dependent microstructures of synthetic anorthite–diopside aggregates. J. Struct. Geol. 29 (6), 1049–1069. ISSN 0191-8141. https://doi.org/10.1016/j.jsg.2007.02.010

Döhmann, M.J.E.A., Brune, S., Nardini, L., Rybacki, E., Dresen, G., 2018. Strain localization and weakening processes in viscously deforming rocks: numerical modeling based on laboratory torsion experiments. In EarthArXiv. https://doi.org/10.31223/osf.io/m2qjp

Drury, M.R., Urai, J.L., 1990. Deformation-related recrystallization processes. Tectonophysics 172 (3–4), 235–253. ISSN 0040-1951. https://doi.org/10.1016/0040-1951(90)90033-5

Ebert, A., Herwegh, M., Pfiffner, A., 2007. Cooling induced strain localization in carbonate mylonites within a large-scale shear zone (Glarus thrust, Switzerland). J. Struct. Geol. 29 (7), 1164–1184. ISSN 0191-8141. https://doi.org/10.1016/j.jsg.2007.03.007

Ferrill, D.A., 1991. Calcite twin widths and intensities as metamorphic indicators in natural low-temperature deformation of limestone. J. Struct. Geol. 13 (6), 667–675. ISSN 0191-8141. https://doi.org/10.1016/0191-8141(91)90029-I.

Ferrill, D.A., Morris, A.P., Evans, M.A., Burkhard, M., Groshong, R.H., Onasch, C.M., 2004. Calcite twin morphology: a low-temperature deformation geothermometer. J. Struct. Geol. 26 (8), 1521–1529. ISSN 0191-8141. https://doi.org/10.1016/j.jsg.2003.11.028.

Fossen, H., Cavalcante, G.C.G., 2017. Shear zones – a review. Earth Sci. Rev. 171, 434–455. ISSN 0012-8252. https://doi.org/10.1016/j.earscirev.2017.05.002.

Fressengeas, C., Molinari, A., 1987. Instability and localization of plastic flow in shear at high strain rates. J. Mech. Phys. Solids 35 (2), 185–211. ISSN 0022-5096. https://doi.org/10.1016/0022-5096(87)90035-4

Fusseis, F., Handy, M.R., 2008. Micromechanisms of shear zone propagation at the brittle–viscous transition. J. Struct. Geol. 30 (10), 1242–1253. ISSN 0191-8141. https://doi.org/10.1016/j.jsg.2008.06.005

Fusseis, F., Handy, M.R., Schrank, C., 2006. Networking of shear zones at the brittle-toviscous transition (Cap de Creus, NE Spain). J. Struct. Geol. 28 (7), 1228–1243. ISSN 0191-8141. https://doi.org/10.1016/j.jsg.2006.03.022

Groshong, R.H., Pfiffner, O.A., Pringle, L.R., 1984. Strain partitioning in the Helvetic thrust belt of eastern Switzerland from the leading edge to the internal zone. J. Struct. Geol. 6 (1–2), 5–18. ISSN 0191-8141. https://doi.org/10.1016/0191-8141(84)90079-8

Guillope, M., Poirier, J.P., 1979. Dynamic recrystallization during creep of single-crystalline halite: an experimental study. J. Geophys. Res. Solid Earth 84 (B10), 5557–5567. ISSN 0148-0227. https://doi.org/10.1029/JB084iB10p05557.

Handy, M.R., Stünitz, H., 2002. Strain localization by fracturing and reaction weakening — a mechanism for initiating exhumation of subcontinental mantle beneath rifted margins. Geol. Soc. Lond., Spec. Publ. 200, 387–407. ISSN 2041-4927. http://sp.lyellcollection.org/content/200/1/387

Hansen, L.N., Zimmerman, M.E., Dillman, A.M., Kohlstedt, D.L., 2012. Strain localization in olivine aggregates at high temperature: a laboratory comparison of constant-strainrate and constant-stress boundary conditions. Earth Planet. Sci. Lett. 333–334, 134–145. ISSN 0012-821X. https://doi.org/10.1016/j.epsl.2012.04.016

Heilbronner, R., Barrett, S.D., 2014. Image Analysis in Earth Sciences: Microstructures and Textures of Earth Materials. Springer, Berlin. http://public.eblib.com/choice/publicfullrecord.aspx?p=1082384

Herwegh, M., Kunze, K., 2002. The influence of nano-scale second-phase particles on deformation of fine grained calcite mylonites. J. Struct. Geol. 24 (9), 1463–1478. ISSN 0191-8141. https://doi.org/10.1016/S0191-8141(01)00144-4

Hielscher, R., Schaeben, H., 2008. A novel pole figure inversion method: specification of the MTEX algorithm. J. Appl. Crystallogr. 41 (6), 1024–1037. https://doi.org/10.1107/S0021889808030112

Hobbs, B.E., Mühlhaus, H.B., Ord, A., 1990. Instability, softening and localization of deformation. In: Knipe, R.J., Rutter, E.H. (Eds.), Deformation Mechanisms, Rheology and Tectonics. 54. Geological Society Special Publication, pp. 143–165.

Kenkmann, T., Dresen, G., 1998. Stress gradients around porphyroclasts: palaeopiezometric estimates and numerical modelling. J. Struct. Geol. 20 (2–3), 163–173. ISSN 0191-8141. https://doi.org/10.1016/S0191-8141(97)00074-6

Kilian, R., Heilbronner, R., Stünitz, H., 2011. Quartz grain size reduction in a granitoid rock and the transition from dislocation to diffusion creep. J. Struct. Geol. 33 (8), 1265–1284. ISSN 0191-8141. https://doi.org/10.1016/j.jsg.2011.05.004

Leroy, Y.M., Molinari, A., 1992. Stability of steady states in shear zones. J. Mech. Phys. Solids 40 (1), 181–212. ISSN 0022-5096. https://doi.org/10.1016/0022-5096(92)90310-X

Mancktelow, N.S., Pennacchioni, G., 2005. The control of precursor brittle fracture and fluid–rock interaction on the development of single and paired ductile shear zones. J. Struct. Geol. 27 (4), 645–661. ISSN 0191-8141. https://doi.org/10.1016/j.jsg.2004.12.001

Menegon, L., Stünitz, H., Nasipuri, P., Heilbronner, R., Svahnberg, H., 2013. Transition from fracturing to viscous flow in granulite facies perthitic feldspar (Lofoten, Norway). J. Struct. Geol. 48, 95–112. ISSN 0191-8141. https://doi.org/10.1016/j.jsg.2012.12.004

Michibayashi, K., Mainprice, D., 2004. The role of pre-existing mechanical anisotropy on shear zone development within oceanic mantle lithosphere: an example from the Oman ophiolite. J. Petrol. 45 (2), 405–414. https://doi.org/10.1093/petrology/egg099

Montési, L.G.J., Hirth, G., 2003. Grain size evolution and the rheology of ductile shear zones: from laboratory experiments to postseismic creep. Earth Planet. Sci. Lett. 211 (1–2), 97–110. ISSN 0012-821X. https://doi.org/10.1016/S0012-821X(03)00196-1

Paterson, M.S., 2007. Localization in rate-dependent shearing deformation, with application to torsion testing. Tectonophysics 445 (3–4), 273–280. ISSN 0040-1951. https://doi.org/10.1016/j.tecto.2007.08.015

Paterson, M.S., Olgaard, D.L., 2000. Rock deformation tests to large shear strains in torsion. J. Struct. Geol. 22 (9), 1341–1358. ISSN 0191-8141. https://doi.org/10.1016/S0191-8141(00)00042-0

Pieri, M., Burlini, L., Kunze, K., Stretton, I., Olgaard, D.L., 2001a. Rheological and microstructural evolution of Carrara marble with high shear strain: results from high temperature torsion experiments. J. Struct. Geol. 23 (9), 1393–1413. ISSN 0191-8141. https://doi.org/10.1016/S0191-8141(01)00006-2

Pieri, M., Kunze, K., Burlini, L., Stretton, I., Olgaard, D.L., Burg, J.-P., Wenk, H.-R., 2001b. Texture development of calcite by deformation and dynamic recrystallization at 1000 K during torsion experiments of marble to large strains. Tectonophysics 330(1–2), 119–140. ISSN 0040-1951. https://doi.org/10.1016/S0040-1951(00)00225-0

Platt, J.P., Behr, W.M., 2011a. Lithospheric shear zones as constant stress experiments. Geology 39 (2), 127–130. ISSN 0091-7613. https://doi.org/10.1130/G31561.1

Platt, J.P., Behr, W.M., 2011b. Grainsize evolution in ductile shear zones: implications for strain localization and the strength of the lithosphere. J. Struct. Geol. 33 (4), 537–550. ISSN 0191-8141. https://doi.org/10.1016/j.jsg.2011.01.018

Platt, J.P., Behr, W.M., 2011c. Deep structure of lithospheric fault zones. Geophys. Res. Lett. 38 (24). https://doi.org/10.1029/2011GL049719. ISSN 0094-8276.

Poirier, J.P., 1980. Shear localization and shear instability in materials in the ductile field. J. Struct. Geol. 2 (1), 135–142. ISSN 0191-8141. https://doi.org/10.1016/0191-8141(80)90043-7

Popov, A.A., Sobolev, S.V., 2008. SLIM3D: a tool for three-dimensional thermomechanical modeling of lithospheric deformation with elasto-visco-plastic rheology. Phys. Earth Planet. Inter. 171 (1–4), 55–75. ISSN 0031-9201. https://doi.org/10.1016/j.pepi.2008.03.007

Poulet, T., Veveakis, M., Herwegh, M., Buckingham, T., Regenauer-Lieb, K., 2014. Modeling episodic fluid-release events in the ductile carbonates of the Glarus thrust. Geophys. Res. Lett. 41 (20), 7121–7128. ISSN 0094-8276. https://doi.org/10.1002/2014GL061715

Regenauer-Lieb, K., Yuen, D.A., 2003. Modeling shear zones in geological and planetary sciences: solid- and fluid-thermal–mechanical approaches. Earth Sci. Rev. 63 (3–4), 295–349. ISSN 0012-8252. https://doi.org/10.1016/S0012-8252(03)00038-2

Regenauer-Lieb, K., Yuen, D.A., 2004. Positive feedback of interacting ductile faults from coupling of equation of state, rheology and thermal-mechanics. Phys. Earth Planet. Inter. 142 (1–2), 113–135. ISSN 0031-9201. https://doi.org/10.1016/j.pepi.2004.01.003

Rogowitz, A., Grasemann, B., Huet, B., Habler, G., 2014. Strain rate dependent calcite microfabric evolution – an experiment carried out by nature. J. Struct. Geol. 69 (Part A), 1–17. ISSN 0191-8141. https://doi.org/10.1016/j.jsg.2014.08.004

Rogowitz, A., White, J.C., Grasemann, B., 2016. Strain localization in ultramylonitic marbles by simultaneous activation of dislocation motion and grain boundary sliding (Syros, Greece). Solid Earth 7, 355–366. https://doi.org/10.5194/se-7-355-2016

Rutter, E.H., 1972. The influence of interstitial water on the rheological behaviour of calcite rocks. Tectonophysics 14 (1), 13–33. ISSN 0040-1951. https://doi.org/10.1016/0040-1951(72)90003-0

Rutter, E.H., 1995. Experimental study of the influence of stress, temperature, and strain on the dynamic recrystallization of Carrara marble. J. Geophys. Res. Solid Earth 100 (B12), 24651–24663. ISSN 2156-2202. https://doi.org/10.1029/95JB02500

Rutter, E.H., Casey, M., Burlini, L., 1994. Preferred crystallographic orientation development during the plastic and superplastic flow of calcite rocks. J. Struct. Geol. (0191-8141) 16 (10), 1431–1446. https://doi.org/10.1016/0191-8141(94)90007-8

Rutter, E., Schmid, S.M., 1975. Experimental Study of Unconfined Flow of Solnhofen Limestone at 500° to 600 °C. GSA Bull. (0016-7606) 86 (2), 145–152. https://doi.org/10.1130/0016-7606(1975)86<145:ESOUFO>2.0.CO;2

Rybacki, E., Paterson, M.S., Wirth, R., Dresen, G., 2003. Rheology of calcite–quartz aggregates deformed to large strain in torsion. J. Geophys. Res. Solid Earth 108 (B2). https://doi.org/10.1029/2002JB001833. ISSN 0148-0227.

Rybacki, E., Wirth, R., Dresen, G., 2008. High-strain creep of feldspar rocks: Implications for cavitation and ductile failure in the lower crust. Geophys. Res. Lett. 35 (4). https://doi.org/10.1029/2007GL032478. ISSN 1944-8007

Rybacki, E., Evans, B., Janssen, C., Wirth, R., Dresen, G., 2013. Influence of stress, temperature, and strain on calcite twins constrained by deformation experiments. Tectonophysics 601, 20–36. ISSN 0040-1951. https://doi.org/10.1016/j.tecto.2013.04.021

Rybacki, E., Morales, L.F.G., Naumann, M., Dresen, G., 2014. Strain localization during high temperature creep of marble: the effect of inclusions. Tectonophysics 634, 182–197. ISSN 0040-1951. https://doi.org/10.1016/j.tecto.2014.07.032.

Schmid, S.M., Paterson, M.S., Boland, J.N., 1980. High temperature flow and dynamic recrystallization in Carrara marble. Tectonophysics 65 (3–4), 245–280. ISSN 0040-1951. https://doi.org/10.1016/0040-1951(80)90077-3

Schmid, S.M., Casey, M., Starkey, J., 1981. The microfabric of calcite tectonites from the Helvetic Nappes (Swiss Alps). Geol. Soc. Lond., Spec. Publ. 9 (1), 151–158. ISSN 2041-4927. http://sp.lyellcollection.org/content/9/1/151

Schmid, S.M., Panozzo, R., Bauer, S., 1987. Simple shear experiments on calcite rocks: rheology and microfabric. J. Struct. Geol. 9 (5–6), 747–778. ISSN 0191-8141. https://doi.org/10.1016/0191-8141(87)90157-X

Schmocker, M., Bystricky, M., Kunze, K., Burlini, L., Stünitz, H., Burg, J.-P., 2003. Granular flow and Riedel band formation in water-rich quartz aggregates experimentally deformed in torsion. J. Geophys. Res. Solid Earth 108 (B5). https://doi.org/10.1029/2002JB001958. ISSN 0148-0227

Schubert, G., Turcotte, D.L., Olson, P., 2001. Mantle Convection in the Earth and Planets. Cambridge University Press.

Tackley, P.J., 2000. Mantle convection and plate tectonics: toward an integrated physical and chemical theory. Science 288 (5473), 2002–2007. http://science.sciencemag.org/content/288/5473/2002

Ter Heege, J.H., De Bresser, J.H.P., Spiers, C.J., 2002. The influence of dynamic recrystallization on the grain size distribution and rheological behaviour of Carrara marble deformed in axial compression. Geol. Soc. Lond. Spec. Publ. 200, 331–353. ISSN 2041-4927. https://doi.org/10.1144/GSL.SP.2001.200.01.19

Tommasi, A., Knoll, M., Vauchez, A., Signorelli, J.W., Thoraval, C., Logé, R., 2009. Structural reactivation in plate tectonics controlled by olivine crystal anisotropy. Nat. Geosci. 2, 423–427. ISSN 1752-0908. https://doi.org/10.1038/ngeo528

Trepmann, C.A., Stöckhert, B., 2003. Quartz microstructures developed during nonsteady state plastic flow at rapidly decaying stress and strain rate. J. Struct. Geol. 25 (12), 2035–2051. ISSN 0191-8141. https://doi.org/10.1016/S0191-8141(03)00073-7

Vauchez, A., Tommasi, A., Mainprice, D., 2012. Faults (shear zones) in the Earth's mantle. Tectonophysics 558–559, 1–27. ISSN 0040-1951. https://doi.org/10.1016/j.tecto.2012.06.006

Wenk, H.R., 1985. Carbonates. In: Preferred orientation in deformed metals and rocks: an introduction to modern texture analysis. Academic Press, pp. 361–384.

Wirth, R., 2005. Focused Ion Beam (FIB): applications in micro- and nanoanalysis in geosciences and applied mineralogy. Prakt. Metallogr. 42 (4), 188–205. https://doi.org/10.3139/147.100258

3 Strain localization and weakening processes in viscously deforming rocks: Numerical modeling based on laboratory torsion experiments

Döhmann, M. J. E. A., Brune, S., Nardini, L., Rybacki, E., & Dresen, G.

2019

Journal of Geophysical Research: Solid Earth, *124*, 1120–1137.

https://doi.org/10.1029/2018JB016917

Key Points:

- First-order numerical softening laws successfully reproduce strain localization and stress transients observed in laboratory torsion tests
- Our models provide a virtual way of analyzing viscous process zone evolution as it nucleates near an inclusion and propagates into a matrix
- The degree of weakening controls the process zone geometry, the finite width of shear bands and the potential formation of ultramylonites

Abstract

Localization processes in the viscous lower crust generate ductile shear zones over a broad range of scales affecting long-term lithosphere deformation and the mechanical response of faults during the seismic cycle. Here we use centimeter-scale numerical models in order to gain detailed insight into the processes involved in strain localization and rheological weakening in viscously deforming rocks. Our 2-D Cartesian models are benchmarked to high-temperature and high-pressure torsion experiments on Carrara marble samples containing a single weak Solnhofen limestone inclusion. The models successfully reproduce bulk stress-strain transients and final strain distributions observed in the experiments by applying a simple, first-order softening law that mimics rheological weakening. We find that local stress concentrations forming at the inclusion tips initiate strain localization inside the host matrix. At the tip of the propagating shear zone, weakening occurs within a process zone, which expands with time from the inclusion tips toward the matrix. Rheological weakening is a precondition for shear zone localization, and the width of this shear zone is found to be controlled by the degree of softening. Introducing a second softening step at elevated strain, a high strain layer develops inside the localized shear zone, analogous to the formation of ultramylonite bands in mylonites. These results elucidate the transient evolution of stress and strain rate during inception and maturation of ductile shear zones.

3.1 Introduction

Localization of deformation is ubiquitous in Earth materials and observed over a broad range of scales in space and time (Fossen & Cavalcante, 2017). In the brittle upper crust, localization is represented by fault zones (Coyan et al., 2013; Valoroso et al., 2013) transitioning into localized ductile shear zones in the middle–lower crust at the brittle-ductile transition hosting mylonites and ultra-mylonites (Palin et al., 2014; Park & Jung, 2017). Localization within the deeper ductile lithosphere is accommodated by a combination of different deformation mechanisms, e.g. diffusion and dislocation creep, frictional sliding or cataclasis, depending on mineral composition and boundary conditions (Burlini & Bruhn, 2005; Kenkmann & Dresen, 2002). These processes cause shear zone initiation at material heterogeneities and multiple defects commonly present in rocks that serve as nucleation points for shear zones on the micro- or macro-scale. Typical examples include randomly scattered flaws (e.g. Misra & Mandal, 2007), brittle fractures (Mancktelow & Pennacchioni, 2005), weak layers (Gerbi et al., 2015), veins and dykes (Handy, 1989) or rock fabric (Bürgmann & Dresen, 2008). A plethora of studies showed that a subsequent strength reduction in shear zones may be attributed to a wide range of processes, like grain-size reduction (Tasaka et al., 2017), shear heating (Duretz et al., 2015), a combination of both (Foley, 2018), a change in controlling deformation mechanism such as from dislocation to diffusion creep (e.g. Handy, 1989; Linckens et al.,

2011; White, 1976), the development of crystallographic preferred orientations (Ji et al., 2004) or melting (Handy et al., 2001).

Laboratory experiments on rock materials provide insights into localization and weakening processes during shear zone formation at well-defined deformation conditions. Several experimental studies at high P-T conditions have investigated strength and microstructures in high-strain deformation tests on mono-mineralic geomaterials. For pure Carrara marble it was found that strain weakening is associated with recrystallization to a fine grain size, the development of a strong lattice-preferred orientation (Pieri et al., 2001a), and that steady state flow is reached at shear strains $\gamma > 4$ (Pieri et al., 2001b). In axial compression tests at 700–990 °C, Ter Heege et al. (2001) found that dislocation creep mechanisms dominate Carrara marble flow at peak stresses and that grain size sensitive mechanisms contribute to flow only for higher bulk shear strains. However, Barnhoorn et al. (2004) observed no significant contribution of diffusion creep even for large shear strains $\gamma \leq 50$. Only minor rheological weakening may be attributed to grain size reduction by dynamic recrystallization, if grain growth is not inhibited (De Bresser et al., 2001). Zener pinning for example impedes grain growth and can thus enhance strain localization (Bruhn et al., 1999; Herwegh et al., 2005; Linckens et al., 2011; Bercovici & Ricard, 2012). By means of experimental studies with multiphase aggregates the localization phenomena have been analyzed at various conditions. A second phase, for example, helps maintain a fine grain size that allows continuous deformation in the diffusion creep regime (Tasaka et al., 2017). Geometric phase mixing occurs only at very high shear strains and is hence a consequence of localization (Cross & Skemer, 2017). Stress partitioning in a two phase system may lead to above-average stresses in one phase and comparatively low stresses in the other (Bruhn & Casey, 1997). Strong stress and strain gradients close to matrix/inclusion interfaces were also observed in a two-phase study using anorthite-diopside aggregates and are similar to deformation microstructures observed in ultramylonites (Dimanov & Dresen, 2005).The effect of material heterogeneities on the rheological response of otherwise homogeneous Earth materials has been recently addressed by Rybacki et al. (2014), who analyzed the effect of material heterogeneities on the onset of localized viscous deformation. These studies revealed a rich interplay of various factors and processes, yet it is difficult to study individual processes in isolation and to provide a time-dependent view of strain localization.

In addition to experimental studies, numerical modeling of localization processes allows testing realistic materials in order to isolate the effect of specific deformation mechanisms and parameters. Previous numerical modeling work aimed at understanding the role of strength anisotropies that are either caused by compositional differences (Kenkmann & Dresen, 1998; Mancktelow, 2002; Treagus & Lan, 2004; Cook et al., 2014) or due to inherited structures (Corti et al., 2007; Mazzotti & Gueydan, 2017; Webber et al., 2018). For example, during lithospheric extension the inherited mechanical structure exerts a strong control on rift geometry and architecture (Duretz et al., 2016). Material heterogeneities significantly impact strain localization: (1) Hard inclusions produce stress

concentrations inside a homogeneous matrix (Kenkmann & Dresen, 1998), and (2) weak inclusions localize strain in turn producing stress concentrations at the inclusion matrix interface (Cyprych et al., 2016). Jammes et al. (2015) identified three end-member types of shear zones: (1) localized, (2) localized anastomosing and (3) delocalized shear zone that depend on the proportion of strong and weak phase and the strength ratio. Other modeling studies focused on the effect of rheological weakening and hardening mechanisms. Weakening mechanisms have been formulated as a function of strain (Cyprych et al., 2016; Mazzotti & Gueydan, 2017), stress (Gardner et al., 2017), deformation work or grain size in combination with grain-size dependent flow laws (e.g. Jessell et al., 2005; Bercovici & Ricard, 2012; Herwegh et al., 2014; Cross et al., 2015). However, all these formulations have been shown to strongly influence the localization behavior in numerical models.

Here we compare the results of our numerical models to a series of laboratory tests (Nardini et al., 2018). in order to investigate the temporal and spatial evolution of strain localization and weakening processes in viscously deforming rocks. As mentioned above, ductile shear zones are often initiated at material heterogeneities which is why we use a single weak inclusion torsion setup to analyze dynamics, strength, and geometry of the resulting ductile shear zone. Based on this reference model, we perform additional numerical experiments assessing the time-dependent impact of weakening through a scan of the relevant parameters and finally we focus on the formation of ultramylonites.

3.2 Laboratory Experiments

3.2.1 Experimental setup

Sample preparation is following the procedures described in Rybacki et al. (2014): Cylinders of Carrara marble (10 mm in length, 15 mm outer diameter) were cut from a single block of marble, and an internal borehole (6.1 mm of inner diameter) was cored and subsequently filled with cylinders of solid gold to provide a homogeneous distribution of stress over the entire sample through the full duration of the experiments (Paterson & Olgaard, 2000). Circular segments of Solnhofen limestone (arc length ~11.8 mm), a very fine grained (average grain size < 10 µm) rock, were produced by polishing ~750 µm thick sections that were subsequently inserted in the external surface of the Carrara marble cylinders (see Figure 1a).

Experiments were conducted in a Paterson-type gas deformation apparatus (Paterson, 1970), at 900 °C temperature and 400 MPa confining pressure. The samples were inserted in copper jackets of ~0.2 mm thickness, and jacket strength at the experimental conditions was accounted for in the evaluation of the mechanical data. Straight vertical scratches on the jacket surface serve as passive strain markers. As shown in Rybacki et al. (2014), at experimental P-T conditions the fine grained limestone is substantially softer than Carrara marble and therefore acts as a weak material heterogeneity within a homogeneous stronger matrix. Two different loading conditions, constant twist rate (equivalent to a

shear strain rate of 1.9×10^{-4} s^{-1} at the outer periphery) and constant torque (~18.8 MPa), were tested. For each loading type, samples were tested to a final bulk shear strain $\gamma \sim 1$ (Nardini et al., 2018).

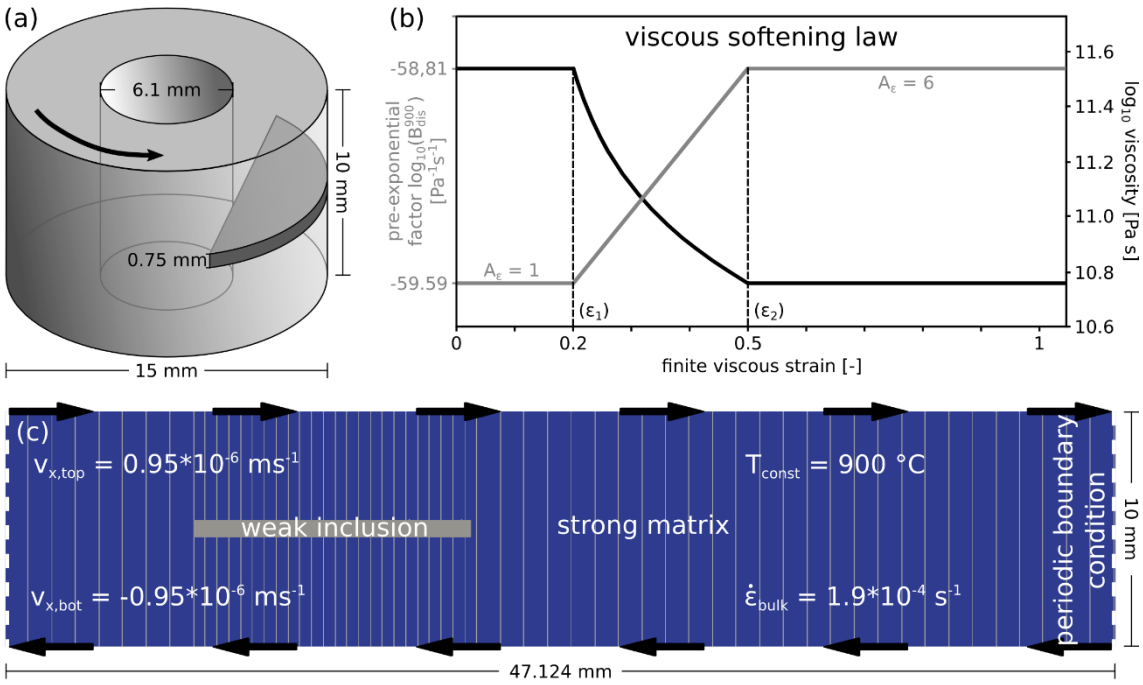

Figure 1. *(a) Schematic drawing of experimental setup: cylinder height is 10 mm, outer diameter is 15 mm, the inclusion features an angular length of 90°, and the inner borehole has a diameter of 6.1 mm and is filled with a solid gold cylinder. The matrix consists of Carrara marble and the inclusion of Solnhofen limestone. (b) Effect of viscous softening on Carrara marble flow law. The factor A_ε (a fraction of the weakening amplitude A) is increased between the two threshold values of local finite strain ε_1 and ε_2, hence the effective viscosity is locally reduced. (c) Model setup and boundary conditions. Constant bulk strain rate ($\dot{\varepsilon}_{bulk}$) is achieved by prescribing velocity at top ($v_{x,top}$) and bottom ($v_{x,bot}$) model boundaries. At the left and right model side we use periodic boundary conditions, i.e. velocity and stress are continuous across these faces and any material point crossing these boundaries enters again on the other side of the model. Flow laws of matrix and inclusion are chosen to represent Carrara marble (strong matrix) and Solnhofen limestone (weak inclusion; see Table 1). Vertical gray lines are passive strain markers.*

3.2.2 Experimental results

At constant twist rate, calculated shear stress at the sample periphery initially increased up to a peak value of ~19–20 MPa at a bulk shear strain of γ ~0.2, followed by gradual weakening up to the maximum bulk shear strain of about 1 for sample CTR1 (Figure 2a). This sample is used to benchmark the numerical model. In the constant torque experiment, torque was kept uniform such that the maximum shear stress at the sample periphery was about 18.8 MPa, similar to the peak stress measured in the constant twist rate experiment (see supplementary Figure S1 for results of the constant torque experiment and a

comparison to a numerical model). The experiments reveal that in front of the inclusion the strain within the Carrara marble was strongly localized forming a *process zone* consisting of highly deformed grains and grain size reduction. The local shear strain in this area is higher than in the adjacent host rock. At the inclusion tip, the local strain is up to about 30 times higher than in the neighboring matrix and ~10 times higher than the bulk strain (Nardini et al., 2018).

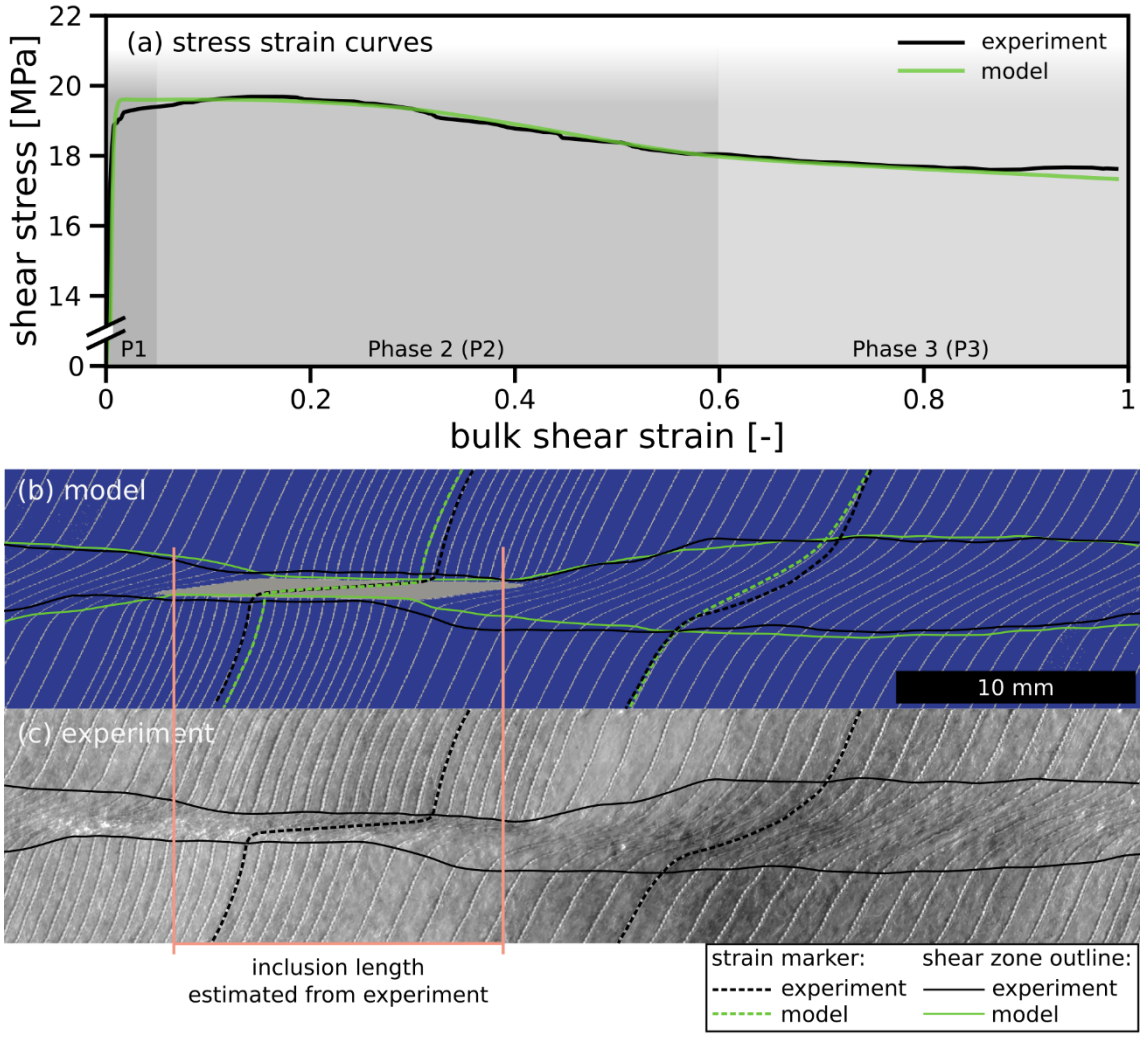

Figure 2. *Benchmark and comparison of constant strain rate model to experiment. (a) Stress strain curves of reference model (green) and experiment (black). Background shows the phases P1 – pre-weakening, P2 – onset and acceleration of weakening and P3 – deceleration of weakening. (b) Model with passive strain markers and shear zone outlines of model (green) and experiment (black). (c) Copper jacket from experiment with passive strain markers, estimated inclusion length and shear zone outline. Results in (b) and (c) are shown at a bulk shear strain of ~1.*

3.3 Model description

In the following, we describe the setup of the numerical model and examine (i) the results in comparison to the associated laboratory experiments, (ii) the time-dependent evolution of the model, (iii) the role of softening, (iv) the effect of varying softening parameters, and (v) the impact of progressive softening. Points (i) and (ii) combined with the mechanical data yield further insights into the strain localization process. With (iii) to (v) we expand the parameter space beyond the experimental results allowing new insights from the numerical perspective.

3.3.1 Numerical modeling technique

We use the geodynamic modeling software SLIM3D (Semi-Lagrangian Implicit Model for 3 Dimensions; Popov & Sobolev, 2008). The implicit finite element code utilizes the Arbitrary Lagrangian-Eulerian Method, has a realistic elasto-visco-plastic formulation for rheology and a free surface. The software was originally designed to investigate lithospheric-scale processes and has since been applied in divergent (Brune et al., 2012, 2013, 2014, 2016, 2017; Brune & Autin, 2013; Brune, 2014; Heine & Brune, 2014; Koopmann et al., 2014; Clift et al., 2015) convergent (Quinteros et al., 2010; Quinteros & Sobolev, 2013; Duesterhoeft et al., 2014; Ballato et al., 2019) and transform (Popov et al., 2012; Brune, 2014) plate boundary settings. Recently however, its scope has been extended with the aim to investigate localization processes on the centimeter scale (Cyprych et al., 2016).

With the SLIM3D software, we solve the thermomechanically coupled conservation equations of momentum

$$-\frac{\partial p}{\partial x_i} + \frac{\partial \tau_{ij}}{\partial x} + \rho g_z = 0 \tag{1}$$

energy

$$\rho C_p \frac{DT}{Dt} - \frac{\partial}{\partial x_i}\left(\lambda \frac{\partial T}{\partial x_i}\right) - \tau_{ij}\dot{\varepsilon}_{ij} = 0 \tag{2}$$

and mass

$$\frac{1}{K}\frac{Dp}{Dt} - \alpha_T \frac{DT}{Dt} + \frac{\partial v_i}{\partial x_i} = 0 \tag{3}$$

with coordinates x_i, velocities v_i, temperature T, time t, pressure p, stress deviator τ_{ij}, strain rate deviator $\dot{\varepsilon}_{ij}$, densities ρ, gravity vector g_z, heat capacities C_p, heat conductivities λ, thermal expansivities α_T, and bulk moduli K. The Einstein summation convention is applied over repeated indices.

The conservation equations are solved simultaneously considering the constitutive laws that relate deformation and stress. Total deviatoric strain rate is described as the sum of elastic and viscous strain rate (Simo & Hughes, 2006):

$$\dot{\varepsilon}_{ij} = \dot{\varepsilon}_{ij}^{elastic} + \dot{\varepsilon}_{ij}^{viscous} = \frac{1}{2G}\hat{\tau}_{ij} + \frac{1}{2\eta_{eff}}\tau_{ij} \quad (4)$$

where G is the elastic shear modulus, $\hat{\tau}_{ij}$ the objective stress rate (e.g. Bonet & Wood, 1997), and η_{eff} the effective viscosity.

We use dislocation creep flow laws to model the viscous deformation of limestone and marble. The effective viscosity is described as:

$$\eta_{eff} = \frac{1}{2}\tau_{II}\dot{\varepsilon}_{dis}^{-1} \quad (5)$$

with τ_{II} as the second invariant of the effective deviatoric stress given by:

$$\tau_{II} = \sqrt{\frac{1}{2}(\sigma_{xx} - p)^2 + \frac{1}{2}\left(\sigma_{yy} - p\right)^2 + \frac{1}{2}(\sigma_{zz} - p)^2 + \sigma_{xy}^2 + \sigma_{xz}^2 + \sigma_{yz}^2} \quad (6)$$

and $\dot{\varepsilon}_{dis}$ as the second invariant of the viscous strain rate for dislocation creep, which is defined as:

$$\dot{\varepsilon}_{dis} = B_{dis}A_{\varepsilon}(\tau_{II})^n \exp\left(-\frac{E_{dis}}{RT}\right) \quad (7)$$

where B_{dis} is the material-dependent creep parameter or pre-exponential factor, A_{ε} is a strain-dependent function of an arbitrary factor A which we call the weakening amplitude (defined below), n is the power law stress exponent, E_{dis} the activation enthalpy and R the gas constant (Popov & Sobolev, 2008). Flow law parameters for Carrara marble and Solnhofen limestone are given in Table 1.

To account for the rheological weakening mechanisms operating in rocks at elevated temperatures and pressures, we implement the function A_{ε} that captures progressive weakening. The strain rate $\dot{\varepsilon}_{dis}$ in each element is increased by this factor A_{ε} depending on the actual viscous strain ε of the element:

$$A_{\varepsilon} = \begin{cases} 1 & if \quad \varepsilon < \varepsilon_1 \\ 1 + \frac{A-1}{\varepsilon_2 - \varepsilon_1}(\varepsilon - \varepsilon_1) & if \ \varepsilon_1 < \varepsilon < \varepsilon_2 \\ A & if \quad \varepsilon > \varepsilon_2 \end{cases} \quad (8)$$

The threshold values ε_1 and ε_2 depend either on 1) accumulated finite viscous strain (see Cyprych et al., 2016) or 2) deformation work per element volume W_{def} defined as:

$$W_{def} = \varepsilon_{visc} * \tau_{II} \quad (9)$$

with ε_{visc} as the viscous component of finite strain, which is computed by integrating the second invariant of the deviatoric viscous strain rate tensor with respect to time. For all $\varepsilon < \varepsilon_1$ the factor A_{ε} is 1. With increasing finite viscous strain, A_{ε} is linearly increased between the threshold values ε_1 and ε_2. For $\varepsilon > \varepsilon_2$, A_{ε} is equivalent to the weakening

amplitude A. As a result, this parameterization reduces the effective viscosity (see Figure 1b). The thresholds ε_1 and ε_2 and the weakening amplitude A of the reference model are determined manually by iterative comparison to experimental observations (Figure 2a). A is chosen such that the stress drop observed from peak stress until the end of the experiment is matched. The threshold values ε_1 and ε_2 control the onset and the end of weakening and were selected such that the shape of the stress strain curve from the experiment is reproduced by the numerical model.

3.3.2 Setup of the numerical model

Our reference model is designed to reproduce the single inclusion experiments of Nardini et al. (2018) described above in 2-D Cartesian coordinates. We model the laboratory shear deformation of a hollow cylinder by using periodic boundary conditions, such that material leaving one side of the model in shear direction enters again on the opposite side (see Figure 1c). The model height is 10 mm and the length of the model along shear direction is 47.124 mm which represents the outer circumference of the hollow cylinder in the laboratory experiment. Thermal properties of the material do not influence the model results, due to an imposed temperature of 900 °C and the small model size. For the same reason temperature gradients are quickly dissipated, which is why shear heating does not play a role. To compare with the experiments, we apply constant strain rate and constant stress boundary conditions, respectively.

Flow laws implemented in the models are based on a series of torsion and triaxial experiments performed on Carrara marble and Solnhofen limestone by Rybacki et al. (2014). The flow law parameters are similar to those obtained by Schmid et al. (1980). Activation energy and thus temperature dependency are incorporated into the material-dependent pre-exponential parameter (B_{dis}^{900}), as the experiments and models are performed at a constant temperature (900 °C; see Table 1). The Solnhofen limestone flows as a superplastic material at the given P-T conditions (Schmid et al., 1977), due to its small grain-size. This is incorporated into the model setup by employing a low stress exponent of n = 1.4 derived by Rybacki et al. (2014).

3.4 Numerical model results

3.4.1 Benchmarking of the numerical model

We deduce the three weakening parameters of our strain-dependent softening parametrization (ε_1, ε_2, A), by iterative comparison between experiments and model. The experimentally derived stress-strain curve and final strain distribution are successfully reproduced using a model with the following values for the accumulated finite strain thresholds: ε_1 = 0.2, ε_2 =0.5 and the weakening amplitude: A = 6 (Figure 1b) affecting the Carrara marble.

Our model results are in excellent agreement with experimental results at constant strain rate (CTR1). Stress strain curve (see Figure 2a), shear zone width and matrix deformation

***Table 1**: Flow laws and boundary conditions for the reference model.*

Phase	Boundary conditions		Flow laws		Reference strength (at strain rate 1.9×10^{-4} s^{-1})	
	T [°C]	strain rate [s^{-1}]	n	$\log_{10}(B_{dis}^{900})$ [Pa^{-1} s^{-1}]	Stress [MPa]	Viscosity [Pa s]
Carrara marble (matrix)	900	1.9×10^{-4}	7.6[ac]	-59.59[a]	22.45	5.91×10^{10}
Solnhofen limestone (inlcusion)			1.4[a]	-13.10[b]	5.00	1.32×10^{10}

Note. *Temperature dependence is incorporated in the pre-exponential factor and flow law parameters are valid for given boundary conditions only (Rybacki et al. 2014). Reference strength gives stress and viscosity at the used bulk shear strain rate ($1.9*10^{-4}$ $s^{-1.}$).*
[a]Rybacki et al. (2014). [b]Rybacki et al. (2014) report -12.55; was modified such that peak stress of model is equivalent to experiment. [c]Schmid et al. (1980).

are very similar as shown by the passive strain markers (see Figure 2b and 2c). The inclusion length fits to the experimental estimate and its distorted rhomboidal shape (Rybacki et al., 2014) is also observed in the model. Steady-state deformation is not yet reached at a bulk shear strain of $\gamma = 1$, indicated by the non-zero slope of the stress strain curve. Constant stress model and experimental results also do not differ significantly as shown in the supplements (Figure S1). In agreement with the results from Nardini et al. (2018), this test likewise indicates that both loading configurations (constant strain rate and constant stress) lead to nucleation of ductile shear zones.

The benchmark comparison also reveals a minor difference between model and experiment. When using the experimentally determined flow laws, we find that the maximum bulk shear stress of the model is ~5% lower than in the experiment. Likely, this offset is due to experimental uncertainties contained in the flow laws, which we level out by adopting a slightly smaller pre-exponential factor for the Solnhofen inclusion (Table 1).

3.4.2 Spatial and temporal model evolution

In this section we investigate the bulk stress evolution by analyzing the evolution of model-intrinsic strength variations that arise from the flow laws and local stress partitioning. To describe inhomogeneous deformation surrounding the shear zone tip we use the term *process zone*, which originates from nonlinear fracture mechanics (Zang et al., 2000). Here we expand its meaning to viscous materials describing a region of enhanced microstructural modification in comparison to the remaining matrix (Rybacki et al., 2014). To analyze the evolution of the process zone that is observed in the experiments, we visualize the stress and strain distribution in space and time. We distinguish four phases (P1–P4) during model evolution: *pre-weakening* (P1), *onset and acceleration of weakening* (P2), *deceleration of weakening* (P3) and *steady-state* (P4). In

phase P1 stresses build up (loading) and no material is weakened by viscous softening, but with ongoing deformation the shear strain locally exceeds the threshold strain ε_1 defining the beginning of weakening and phase P2 at a bulk shear strain of γ ~0.05.

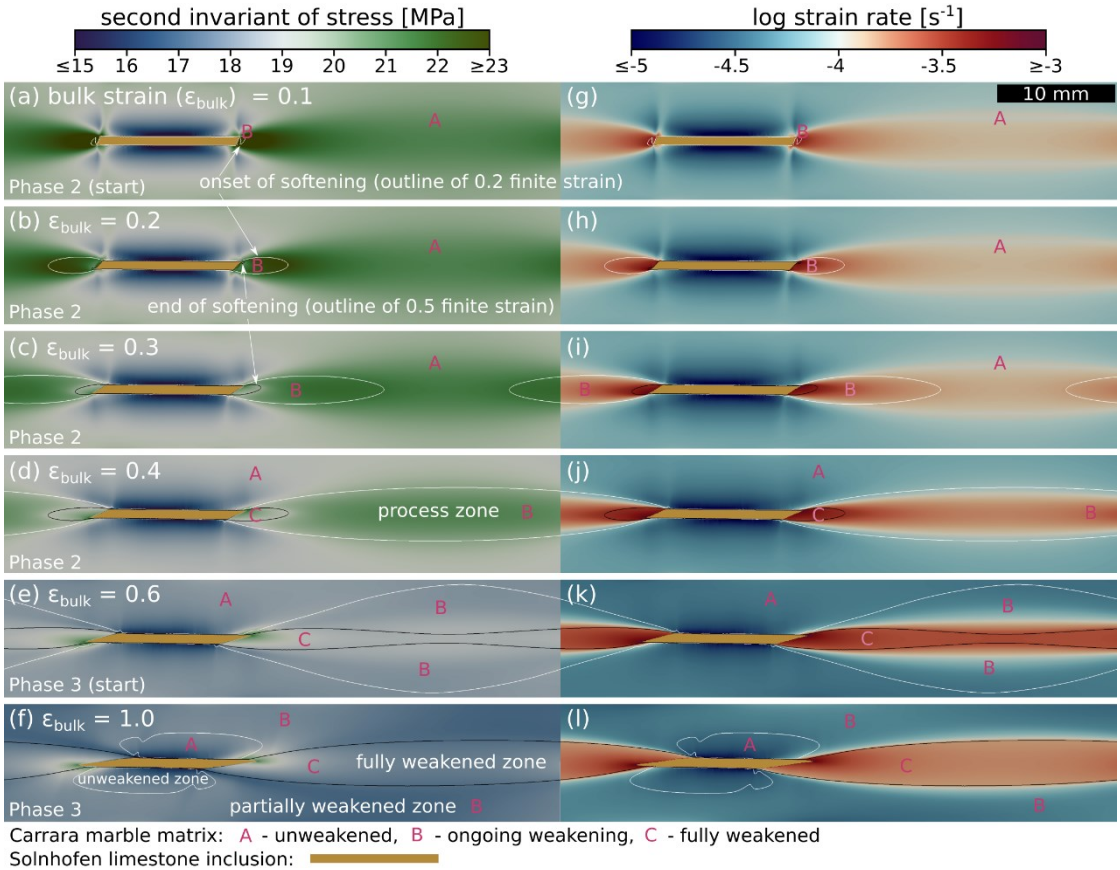

Figure 3. *Local stress (second invariant of the effective deviatoric stress) (a–f) and strain rate (g–l) evolution within the matrix of the constant strain rate benchmark model. A, B and C distinguish three different Carrara marble zones and their outlines indicate finite strain thresholds of $\varepsilon_1 = 0.2$ for beginning (white) and $\varepsilon_2 = 0.5$ for end (black) of softening. The process zone B is associated with a local stress maximum propagating into the matrix (a–c). The zone is controlled by the onset and end of softening. A second stress peak remains fixed at the inclusion tips (a–f).*

From this moment on the Carrara marble matrix is subdivided into an unaltered zone A and the process zone B that is submitted to ongoing weakening (Figure 3). With progressive deformation the process zone grows and a larger volume exceeds the weakening threshold, accelerating bulk softening. At a bulk shear strain of $\gamma \sim 0.6$ the process is slowing down defining the beginning of P3. Two fully weakened regions C emerge in the model center where shear strains start to exceed ε_2 that defines the second threshold and completion of weakening (Figure 3d). In phase P4 the deformation proceeds at steady state, which is only observed for bulk shear strains $\gamma > 2$ using the reference setup. In the experiment and the benchmark model, steady state is not reached since the test is terminated at a bulk shear strain of $\gamma \sim 1$.

Pronounced stress peaks in front of the inclusion tips are observed during early stages of deformation (P1 and early P2) (see Figure 3a) resulting in higher strain rates (Figure 3g) than in surrounding matrix regions of low stress. Similar to the experimental results, strain rates in the process zone are locally increased by up to a factor of ~30 in comparison to the matrix. Due to this stress and thus strain rate differences, the finite strain threshold value ε_1 (white outline) is first exceeded at the inclusion tips where softening of the material starts. This leads to a positive feedback promoting localization. Strain rate subsequently increases further and soon the second threshold value ε_2 (black outline) is also exceeded indicating local completion of softening (see Figure 3b–f and 3h–l). Consequently, stress gradually decreases again locally between the onset outline and the inclusion (see Figure 3b and 3c). The stress concentrations at the inclusion tips remain due to the remaining viscosity contrast between matrix and inclusion. The cylindrical symmetry of the experiment and our model results in a merge of the two weakening fronts (ε_1 outline). Once the two local stress peaks causing the onset of softening merge, they combine to a single, local stress maximum in the model center and the stress gradient in the process zone decreases significantly with further deformation (see Figure 3e). The fully weakened zones C grow, as the process zone B propagates into the matrix from the inclusion, featuring a gradual stress increase from the end of softening outline towards the inclusion tips (see Figure 3d). In phase P3 the completely weakened areas in the vertical model center are connected (see Figure 3e and 3k), after which the rate of weakening decreases (Figure 2a). Stress and strain rates directly above and below the inclusion remain low throughout the experiment due to local stress partitioning. A small transition zone between the inclusion and matrix exists due to coupling of the materials. The overall observed stress drop in the matrix (Figure 3a–f) results from our weakening parameterization, which decreases the effective viscosity of the Carrara marble.

Analytical solutions of a linear dislocation in an elastic half- space predict extremely high stresses as displacements vanish towards fracture tips (Okada, 1985). Within the ductile regime and for inclusions of finite width, however, we can show that the localization process at the inclusion tip evolves in a smoother and time-dependent way. Figure 4 shows length profiles that display key parameter values and their evolution with increasing bulk strain along two horizontal model cross sections. The position of profile (a) is chosen such that it crosses the center of the right inclusion tip at a bulk shear strain of 1 which is 0.1 mm above profile (b) along the model center. Horizontal velocity in profile (a) is increased, due to the vertical shift in position.

By that, the point symmetry to the inclusion center is broken, which on the other hand is a feature of profile (b). Similar to a dislocation in an elastic medium, the area surrounding the inclusion tip exhibits high gradients in deformation and stress. The profiles show the highest strain rates and strains inside the weak inclusion directly at the tip. Highest stress values are however observed in the matrix in front of the inclusion. Local strain in the process zone at the inclusion tip increases approximately linear with bulk strain by a factor of ~4.

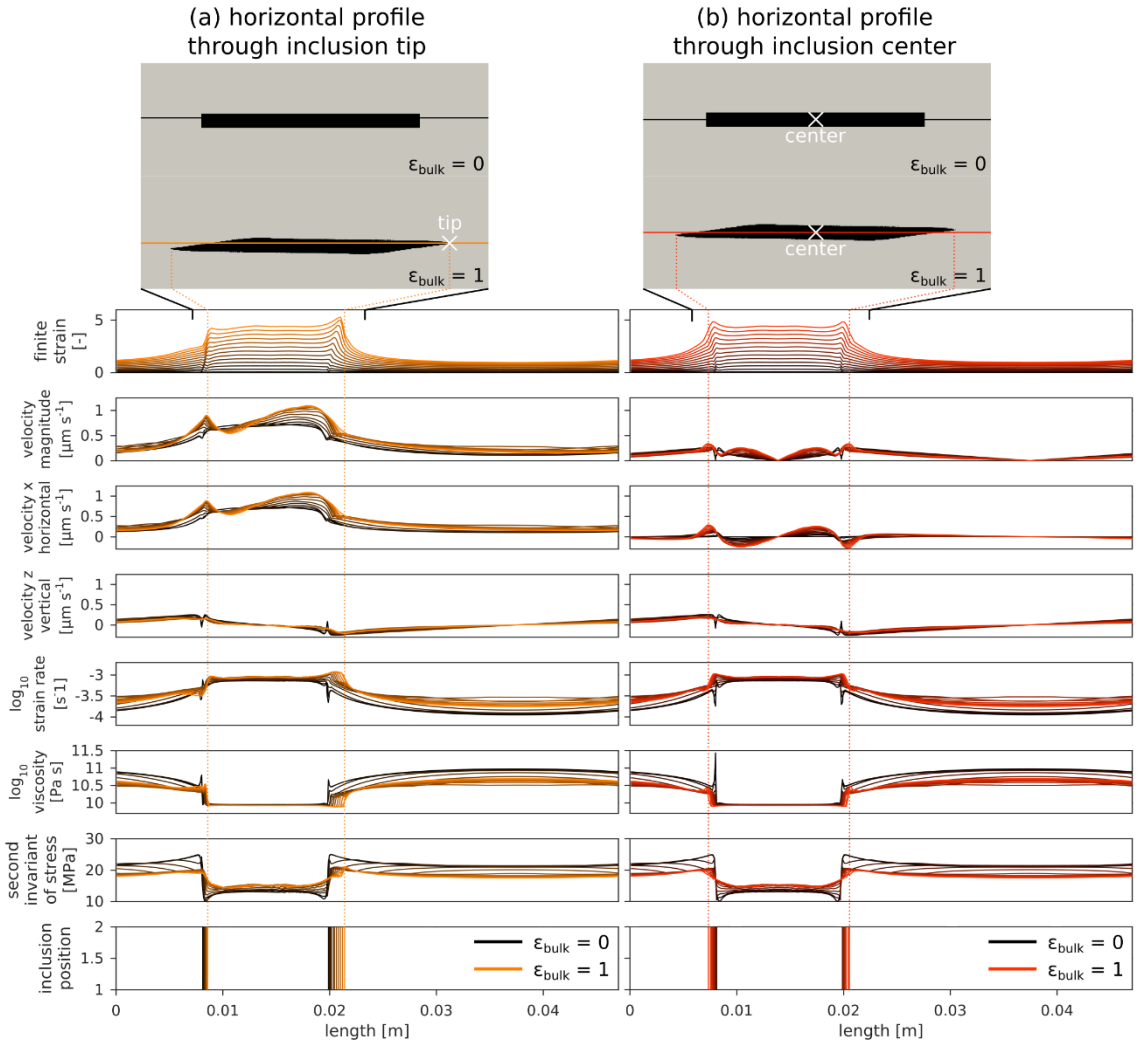

Figure 4. *Along-strike variations of key variables through time. The inclusion deforms due to simple shear generating differences between horizontal profiles at various vertical positions. Here we show horizontal profiles along the center of the inclusion (at a bulk shear strain of 1) and along the center of overall model domain, which is also the center of the inclusion. (a) Horizontal profile along the center of the inclusion tip. Maximum rate of deformation and accumulated finite strain are found in the inclusion tip and maximum stress in the matrix directly in front of the inclusion tip. (b) Horizontal profile along the model center. Due to the symmetry of the setup, results are approximately point symmetric to the model center.*

3.4.3 The impact of softening on the reference model

To better constrain the effect of the viscous softening formalism, we run an additional constant strain rate model, but without the strain dependent weakening law. Besides the differences in the stress strain curves (Figure 5a), also a less pronounced shear zone development is observed (Figure 5b). This is indicated by the linearly deflected, yellow strain marker crossing the matrix and the yellow shear zone outline. Strain is instead localizing mainly in the inclusion and, to a lesser extent, in the matrix close to the inclusion tips. Nonetheless, the results of this test still show reasonable agreement with

the experimental data, because the bulk weakening is generally low for the used samples and setup, which is indicated by the total shear stress drop of just ~2 MPa in the experiment.

Additionally, we test a softening law that is based on deformation work instead of finite strain as discussed above. In this formulation, the weakening thresholds (ε_1 and ε_2, Eq. 8) are not based on finite strain, but on deformation work as defined in Eq. 9. Threshold values ε_1 and ε_2 were chosen following the iterative procedure described above for finite strain. However, we find no significant difference to the strain based softening implementation (see supplementary Figure S2).

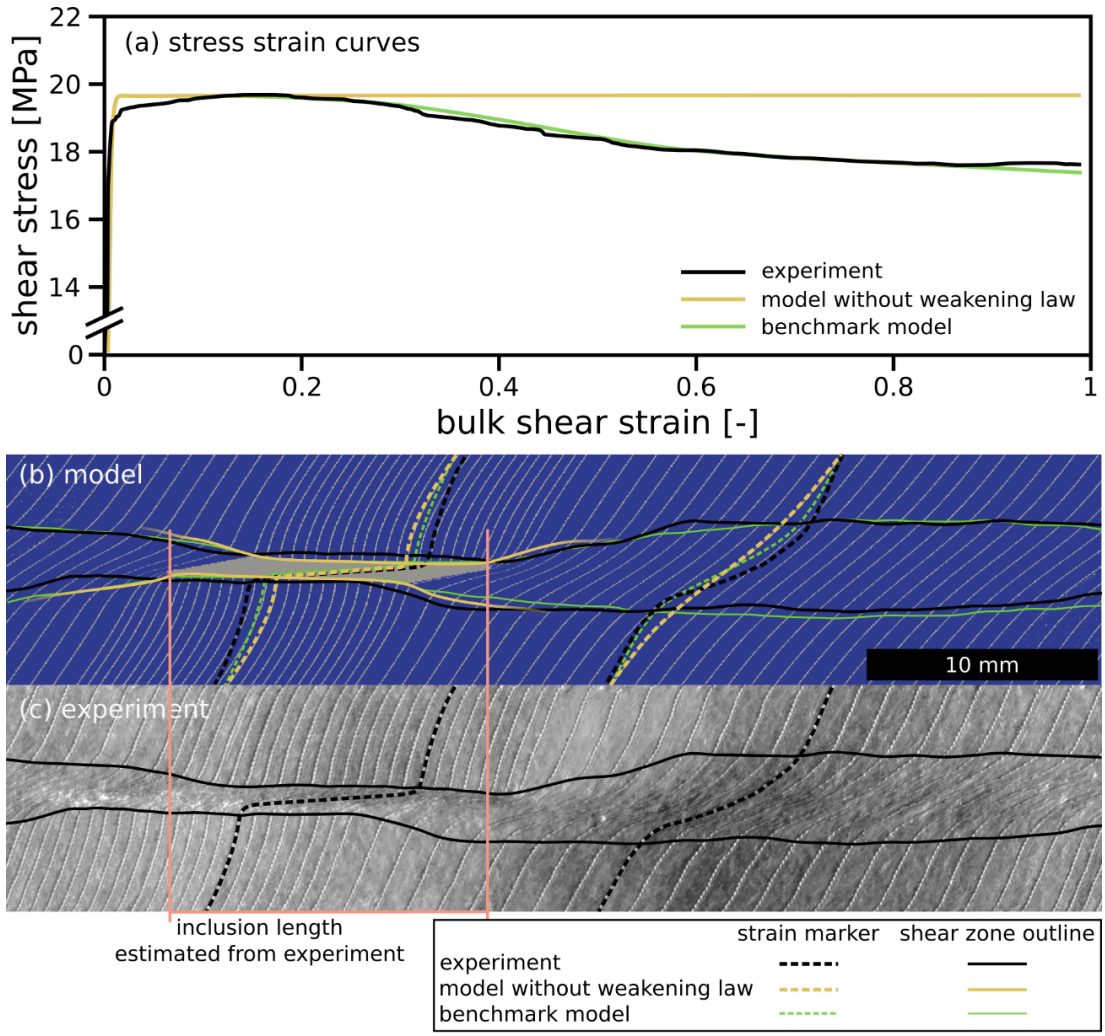

Figure 5. *Comparison of model without the weakening law to experiment and reference model (same as in Figure 2c). (a) Stress strain curves of model without weakening law (yellow), experiment (black) and reference model (green). (b) Model without weakening law with passive strain markers and shear zone outlines of model where inferable (yellow), experiment (black) and reference model (green). (c) Copper jacket from experiment with passive strain markers, estimated inclusion length and shear zone outline. Results in (b) and (c) are shown at a bulk shear strain of $\gamma \sim 1$. In comparison to the reference model, shear stress remains constant over time and the shear zone in the matrix is less pronounced.*

3.4.4 The softening law parameters

This chapter addresses the effects of the softening law parameters on the localization process. We therefore vary the three controlling parameters (Figure 1b), the finite strain threshold values onset (ε_1) and end (ε_2), as well as the weakening amplitude (A). In order to test the effect of varying A, we change this parameter between 1 and 500 leaving the remaining reference model parameters unchanged, that is ε_1 (0.2) and ε_2 (0.5) (Table 2). Models are conducted up to a bulk shear strain of γ ~4, where steady state conditions are reached in almost all cases. The reference model for instance reaches steady state at a bulk shear strain of approximately 2 (Figure 6a). Increasing A amplifies the weakening of the Carrara marble matrix, resulting in a bulk shear stress drop and enhanced strain and thus shear zone localization, which is also indicated by a decreasing angle between inclusion and matrix shear zone (Figure 6). Large values of A increase the rate of strain localization. This is indicated by the sudden shear stress drop at a bulk shear strain of 0.4 and by faster stress peak propagation into the matrix. For values of $A > 50$ the matrix separates into two zones of substantial viscosity contrast (Figure 6b).

Table 1. *Parameters for models used to test the effect of the weakening amplitude (A) of the softening law.*

Models for testing weakening amplitude A	ε_1	ε_2	$\Delta\varepsilon$	A
M0 – no softening	–	–	–	1
M1 – reference model	0.2	0.5	0.3	6
A1	0.2	0.5	0.3	20
A2	0.2	0.5	0.3	100
A3	0.2	0.5	0.3	500

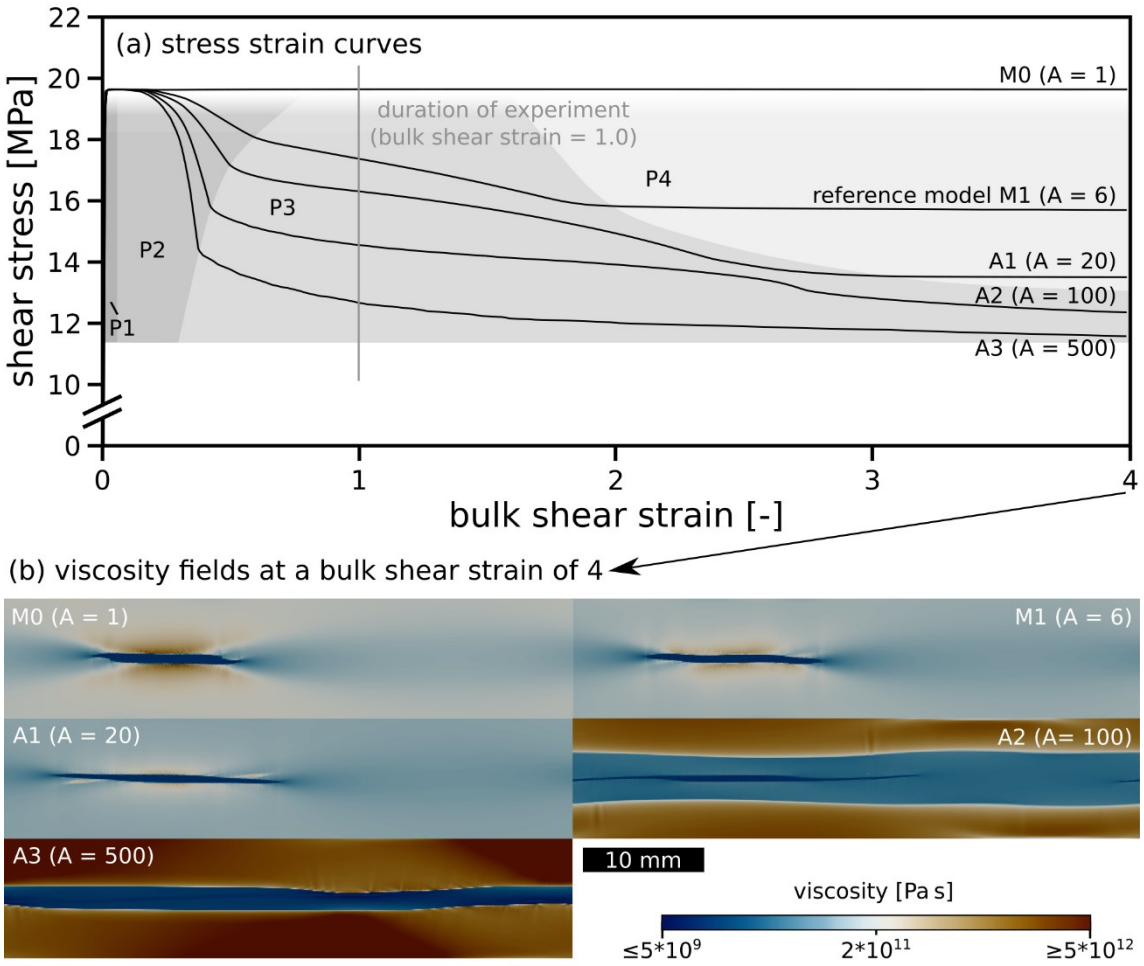

Figure 6. *Effect of the weakening amplitude A. (a) Stress strain curves of models with different weakening amplitude. For comparison the duration of the torsion experiment is indicated. P1–P4 refer to the phases described in chapter 3.4: pre-weakening (P1), onset and acceleration of weakening (P2), deceleration of weakening (P3) and steady-state (P4). (b) Viscosity fields of the models at a bulk shear strain of 4. The inclusion in the reference model is elongated further than in the model without weakening, as the matrix is increasingly deformed due to the softening law. This effect increases with A. For values of A > 50, strain localization is strongly pronounced, as shown by the viscosity field of models with a weakening amplitude A of 100 and 500. Higher values of weakening amplitude lead to stronger weakening and localization.*

In another experiment, models are run up to a bulk shear strain of 4, varying $\varepsilon_1$and ε_2 at constant A (Table 3). As expected, this shifts the onset and end of weakening – earlier for lower finite shear strain values and later for higher – but the actual effect on the model is not linear (Figure 7a). Note that by changing the strain range of softening $\Delta\varepsilon = \varepsilon_1 - \varepsilon_2$, the slope of the stress strain curve and thus localization rate is affected as well. The reference model with the lowest $\Delta\varepsilon$ displays the fastest localization rate, because the rate with which the pre-exponential factor is increased is higher between the two thresholds due to the linear nature of the softening law. Model E2 with $\Delta\varepsilon$ of 0.8 however, reaches steady state only after a long period of ongoing softening (between 0.4 and 3.4 bulk shear strain). The

local stress patterns of the tested models differ at a bulk shear strain of 1, depending on the applied threshold values. While model M0 is in the pre-weakening phase P1, model E3 & E2 are in phase P2 and model M1 & E1 already reached phase P3 approaching steady-state conditions (Figure 7b).

Table 2. *Parameters for models used to test the effect of onset (ε_1) and end (ε_2) of the softening law.*

Models for testing onset and end	ε_1	ε_2	$\Delta\varepsilon$	A
M0 - no softening	-	-	-	1
M1 - reference model	0.2	0.5	0.3	6
E1	0.0	0.5	0.5	6
E2	0.2	1.0	0.8	6
E3	0.5	1.0	0.5	6

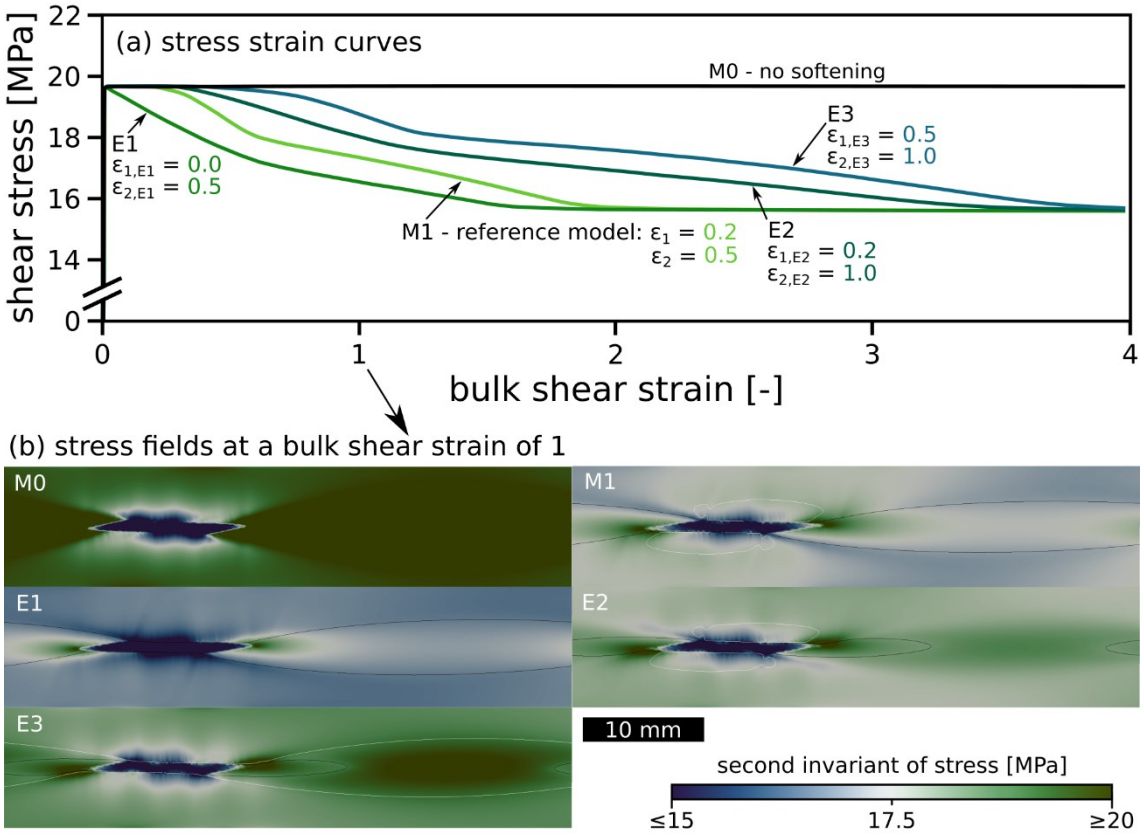

Figure 7*. Effect of onset and end of weakening on the stress strain evolution. (a) Stress strain curves of models with varying onset (ε_1) and end parameters (ε_2). Note the shapes of curves E1 and E3 (same $\Delta\varepsilon$) indicating a non linear relationship between threshold parameters and weakening behavior. (b) Stress field (second invariant of the effective deviatoric stress) of models at bulk shear strain of 1. M0) no softening; M1) reference model; E1) $\varepsilon_1 = 0$; E2) $\varepsilon_2 = 1$; E3) $\varepsilon_1 = 0.5$ and $\varepsilon_2 = 1.0$. Models with lower ε_1 have lower bulk strengths at the same bulk shear strain.*

3.4.5 Ultramylonite model – the effect of progressive softening and switch of deformation mechanism

Mylonitic shear zones often feature mm–cm wide bands with fine grain sizes referred to as ultramylonites (Hippertt & Hongn, 1998; Kenkmann & Dresen, 2002). It is commonly assumed that grain size refinement from cataclasis (Blenkinsop, 1991), dynamic recrystallization (Warren & Hirth, 2006) or mineral reactions (Herwegh et al., 2003) promotes a switch to grain size-sensitive deformation (Heitzmann, 1987; Bürgmann & Dresen, 2008). The switch to grain size-sensitive creep is transient unless grain growth is suppressed (e.g., Pearce & Wheeler, 2011), which can be achieved for example by pinning through phase mixing. In order to mimic a progressive change in mechanism, a second softening step is introduced using a similar approach as described above for the onset of weakening (Eq. 8), where we add additional strain thresholds for onset (ε_3) and end of weakening (ε_4). This second softening step is exploratory and not based any data. Configuration of the model setup and the initial onset of softening are identical to the reference model, hence earliest stages of model evolution are the same as before. The introduction of a second softening step with progressive strain, however, is expected to lead to further localization and formation of a narrow low-viscosity layer embedded in the primary shear zone. To this end finite strain thresholds for onset of weakening (ε_3 = 1) and completion (ε_4 = 2) are chosen, respectively. This procedure enables formation of a localized *ultramylonite* band inside the active shear zone. A high weakening amplitude (A_{um} = 20) is chosen to enable fast and strong localization once the threshold ε_3 is reached.

Evolution of the model is equivalent to the reference model for bulk shear strains less than 0.4 (compare Figure 3a–d to Figure 8a–d). Upon onset of the second softening stage, strain localizes into a narrow zone in the model center (Figure 8n and 8o). Inside this high strain zone, the inclusion is strongly elongated and an anastomosing pattern of the second shear zone establishes (Figure 8q and 8r) that additionally becomes wider with increasing bulk strain (Figure 8o–r). This transition to an anastomosing shape forms due to a rotation, which is caused by the shear deformation that the material is subjected to. Despite the simplicity of our setup with a single inclusion, our model nevertheless captures the nested structure and the anastomosing shape of the resulting high-strain band. This agrees very well with common observations of ultramylonite bands in nature (Heitzmann, 1987; Kilian et al., 2011).

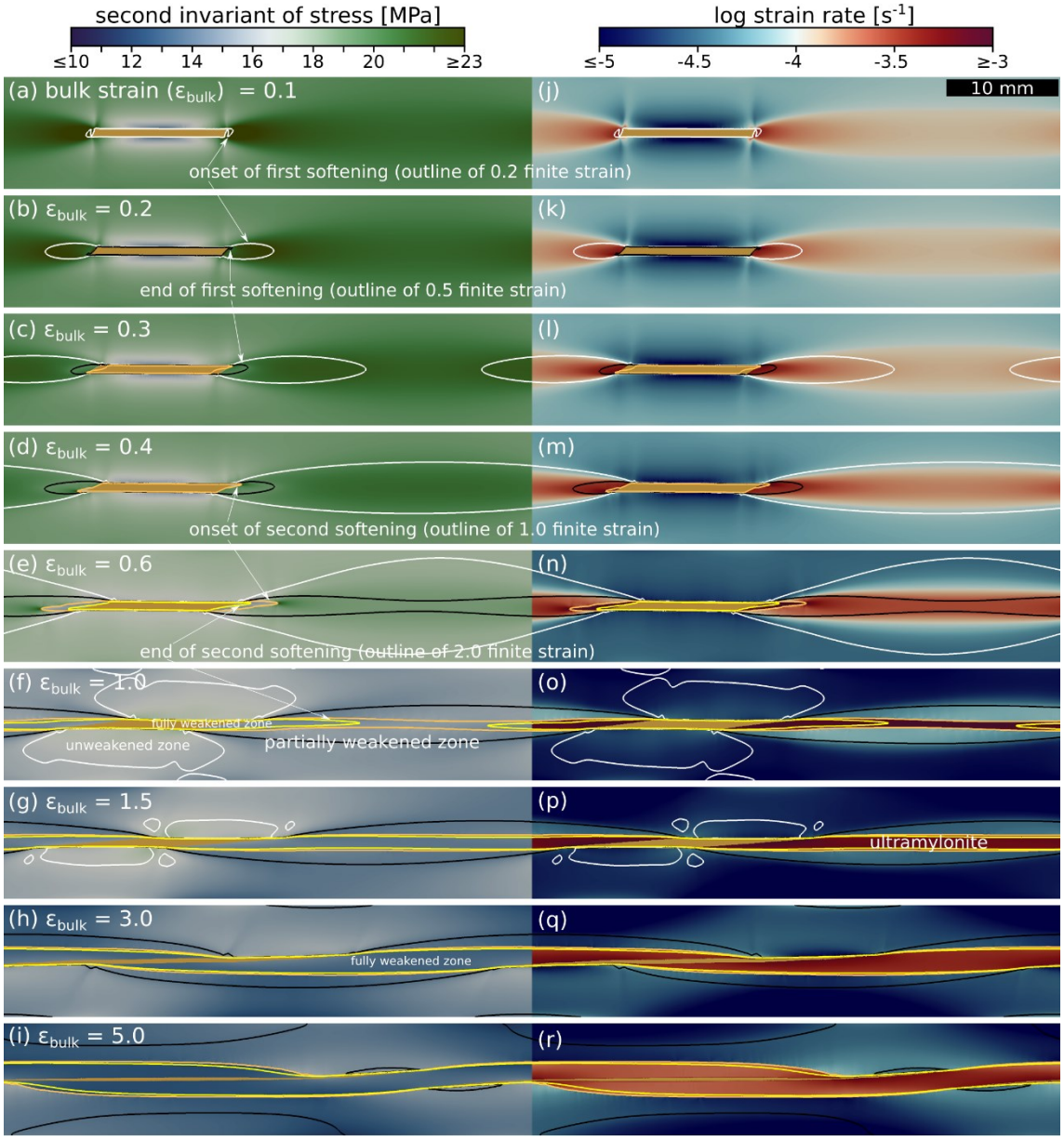

Figure 8. *Local stress (second invariant of the effective deviatoric stress) (a–i) and strain rate (j–r) evolution within the matrix of the ultramylonite model. Outlines indicate finite strain thresholds $\varepsilon_1 = 0.2$ for onset of softening (white), $\varepsilon_2 = 0.5$ end of first softening stage (black), $\varepsilon_3 = 1.0$ for beginning of second stage (orange) and, $\varepsilon_4 = 2.0$ for end of second (yellow) softening stage. The onset of the second softening stage triggers evolution of further localized high strain layer (e, f, n and o) representing ultramylonite formation within a mylonite.*

3.5 Discussion

3.5.1 Strain localization and shear zone evolution

The ductile shear zone formation observed in the experiments involves strain localization, rheological weakening of the Carrara marble and bulk strength reduction. Our numerical model reproduces these observations by employing a strain dependent viscous softening

law. The model reaches steady state at a bulk shear strain of ~2 in good agreement with observations from experiments (Rybacki et al., 2014). Once steady-state is reached, grain-size reduction through dynamic recrystallization and grain growth are anticipated to reach a dynamic balance (De Bresser et al., 2001), resulting in steady-state material strength. Our model results provide insight into the development of local stress, strain partitioning between matrix, inclusion and shear zone and ensuing viscosities. This provides detailed insight in the evolution of a localized shear zone that allows a direct comparison with the bulk mechanical data and microstructural observations collected from the deformation experiments. It has to be kept in mind though, that the numerical model does not feature the grain-scale resolution necessary to reproduce the brittle deformation as observed in the experiments. Nevertheless, the model successfully predicts local stress concentration and strain rate amplification ahead of the inclusion in first order agreement with the experimental results. This provides confidence to the results of the parameter study performed here, as to the magnitude of softening. This holds in particular to the results of models predicting progressive multistage softening combined with a change in deformation mechanisms, as suggested from a large number of field studies.

The nucleation of a localized shear zone at the inclusion tips involves formation of a process zone. This process zone is defined by a strong local stress concentration and resulting volume of enhanced microstructural modification (Rybacki et al., 2014). In our models this zone is represented by a 2D area showing local stress concentrations that result from the viscosity contrast between limestone and marble present at the assumed temperature conditions. The enhanced stress levels locally reduce the effective viscosity of the Carrara marble (power-law rheology) resulting in locally increased strain rates. In turn, this triggers rheological weakening causing shear strain to progressively localize in a shear zone embedded in the Carrara matrix. A localized, elliptical process zone is established, corresponding to the experiments, that displays a zone of gradually reduced grain-sizes around the inclusion tips.

3.5.2 Relating our softening parameterization to nature

The two threshold values for finite strain (ε_1 and ε_2) used in the numerical model are expected to mimic the effects that microstructural changes within the process zone have on the bulk strength of the experimentally deformed samples. As such, they are unlikely to represent specific and observable stages of the local microstructural evolution within the process zone. Strain weakening behavior is known to results from a number of different processes, e.g., dynamic recrystallization, dislocation annihilation, vacancy diffusion or lattice preferred orientation. These concur to produce the microstructural and textural modifications that can be observed in our experimental samples in proportions that are likely to vary in the course of the transient processes discussed here. A simple linear parametrization cannot be expected to capture single elements of such complexity within heterogeneously deforming samples. Our parameterization, however, appears to reproduce the phenomenological aspects of weakening as observed in our experiments with reasonably high accuracy.

While it is beyond the scope of our model to pinpoint the micromechanical processes and features corresponding to specific values of local shear strain, some general observations can be made to discuss the significance of our approach. Plastic yield of the bulk assembly, suggesting the onset of strain weakening processes at the local scale, is already observed at very low values of bulk shear strain (~0.01–0.02, cf. Fig. 4 in Nardini et al, 2018) corresponding to a local strain of ~0.1–0.2 at the tip of the inclusion (cf. Fig. 6a in Nardini et al., 2018), which is in the range of our selected ε_1. It is important to notice that the process zone forming along the weak inclusion plane is intrinsically transient both on a temporal and spatial level. The heterogeneity-induced viscosity contrast produces a volume of stress enhancement (e.g. Fig. 3), which evolves with bulk shear strain and determines a strongly heterogeneous strain distribution (Fig. 6 in Nardini et al., 2018). Similarly to what would be expected in the brittle regime for slip-weakening behavior, an area of strength perturbation is developed. It is characterized by higher strain rates and increasing microstructural changes closer to the inclusion: the extent of such a perturbation may determine the value of ε_2, that is. the *end of weakening* in our softening law. Whether or not, in a non-steady-state shear zone like is the case in our experimental samples, a microstructural and/or textural signature would be associated at all times with the varying volume of perturbed material is questionable. It is therefore reasonable to conclude that, while a definite one-to-one correlation between the described finite strain threshold values and specific microstructural changes is not possible, these parameters are still able to capture the bulk mechanical expression of the strain weakening processes locally activated in the microstructures.

3.5.3 Scope and limitation of strain softening parametrization

The advantage of employing a simple, first-order softening law is to keep numerical complexity low, which is not only more transparent, but also saves computational time in large-scale models (e.g. Huismans & Beaumont, 2003; Brune et al., 2014). In an attempt to model rock weakening and strain localization, different types of softening parameterizations have been previously used in order to describe the weakening behavior of natural materials. For example, Gardner et al. (2017) studied strain localization using different load bearing framework geometries. They found that interconnected weak layers are hard to form without a dynamic weakening process, which was also observed in an experimental study by Holyoke & Tullis (2006). This agrees with our results showing that pronounced shear zone formation in the matrix only occurs for materials with an implemented weakening formalism simulating progressive material softening. This implies the necessity of using softening laws to properly model strain localization and thus shear zone formation. Gardner et al. (2017) used a different implementation to simulate weakening. They introduced stress dependent softening combined with time dependent hardening focusing on the transition from non-linear to linear flow. At larger scale, Mazzotti & Gueydan (2017) pointed out the fundamental role of inherited tectonic structures for strain and seismicity concentrations in an intraplate setting. Similar to our study, their model also includes irreversible softening (no counteracting hardening

mechanism). However, in their model softening is achieved by changing the material yield stress instead of the pre-exponential factor in a constitutive law, as in this study.

In large-scale rock deformation, there are several major effects that may play an important role affecting localization and shear zone formation and that need to be considered in numerical modelling studies. These are highly non-linear processes such as shear heating (Thielmann & Kaus, 2012; Duretz et al., 2015; Foley, 2018), melting (Dannberg & Heister, 2016; Schmeling et al., 2018) or a switch to grain-size sensitive diffusion creep, like modeled in our study (e.g. Handy, 1989). In that aspect, our models provide a minimum constraint to the degree of viscous strain softening that can be expected to act in nature. Another important point is that numerical models of brittle deformation often involve a strong mesh-dependency (De Borst & Mühlhaus, 1992) such that the softening parameters have to be adopted to the chosen resolution. However, this is not the case when modeling viscous deformation where the size of the process zone as well as the bulk shear stress evolution and employed softening parameters (ε_1, ε_2, A) are almost independent of the model resolution.

3.6 Conclusions

Strain localization in shear zones is an important process in lithosphere dynamics occurring over a broad range of spatial scales. For simplicity, we use a piece-wise linear softening law and show that it is capable of reproducing rheological weakening observed in laboratory experiments. Our model provides a virtual way of analyzing the viscous process zone evolution that can be divided into four phases (P1) *pre-weakening*, (P2) *onset and acceleration of weakening*, (P3) *deceleration of weakening* and (P4) *steady state*. Spatial stress distributions show that matrix strain localization is initiated by a local stress peak at the inclusion tips. From there and with increasing strain, the process zone expands into the matrix. Shear zone width and localization rate are controlled by the amount of rheological weakening. Our numerical models show that rheological weakening is necessary to establish a pronounced shear zone in a strong matrix surrounding a weak inclusion and to explain the anastomosing shape and the nested structure of ultramylonites. This reinforces the importance for geodynamic models to contain softening laws that appropriately account for rheological weakening.

Acknowledgments

This manuscript has been greatly improved thanks to the constructive comments and suggestions of Andrew Cross, an anonymous reviewer, and associate editor Bjarne Almqvist. This study was conducted within the Helmholtz Young Investigators Group CRYSTALS (VH-NG-1132). Laboratory experiments were performed in Geomechanics and Rheology section of the German Research Centre for Geosciences and we thank Stefan Gehrmann for help with sample preparation. Simulations were performed on the cluster facilities of the German Research Centre for Geosciences. All data that this

numerical study is based on is found in Figure 1 and the parameter Tables 1, 2 and 3. Additional data regarding the torsion experiment is found within Nardini et al. (2018). Figures were created using Paraview and Matlab and color maps were taken from Crameri (2018).

References

Ballato, P., Brune, S., & Strecker, M. R. (2019). Sedimentary loading–unloading cycles and faulting in intermontane basins: Insights from numerical modeling and field observations in the NW Argentine Andes. Earth and Planetary Science Letters, 506, 388-396. https://doi.org/10.1016/j.epsl.2018.10.043

Barnhoorn, A., Bystricky, M., Burlini, L., & Kunze, K. (2004). The role of recrystallisation on the deformation behaviour of calcite rocks: Large strain torsion experiments on Carrara marble. Journal of Structural Geology, 26(5), 885–903. https://doi.org/10.1016/j.jsg.2003.11.024

Bercovici, D., & Ricard, Y. (2012). Generation of plate tectonics with two-phase grain-damage and pinning. Physics of the Earth and Planetary Interiors, 202, 27–55. https://doi.org/0.1016/j.pepi.2012.05.003

Blenkinsop, T. G. (1991). Cataclasis and processes of particle size reduction. Pure and Applied Geophysics, 136(1), 59–86. https://doi.org/10.1007/BF00878888

Bonet, J., & Wood, R. D. (1997). Nonlinear Continuum Mechanics for Finite Element Analysis. Cambridge University Press. https://doi.org/10.1017/CBO9780511755446

Bruhn, D. F., & Casey, M. (1997). Texture development in experimentally deformed two-phase aggregates of calcite and anhydrite. Journal of Structural Geology, 19(7), 909–925. https://doi.org/10.1016/S0191-8141(97)00023-0

Bruhn, D. F., Olgaard, D. L., & Dell'Angelo, L. N. (1999). Evidence for enhanced deformation in two-phase rocks: Experiments on the rheology of calcite-anhydrite aggregates. Journal of Geophysical Research, 104(B1), 707–724. https://doi.org/10.1029/98JB02847

Brune, S. (2014). Evolution of stress and fault patterns in oblique rift systems: 3-D numerical lithospheric-scale experiments from rift to breakup. Geochemistry, Geophysics, Geosystems, 15(8), 3392–3415. https://doi.org/10.1002/2014GC005446

Brune, S., & Autin, J. (2013). The rift to break-up evolution of the Gulf of Aden: Insights from 3D numerical lithospheric-scale modelling. Tectonophysics, 607, 65–79. https://doi.org/10.1016/j.tecto.2013.06.029

Brune, S., Heine, C., Clift, P. D., & Pérez-Gussinyé, M. (2017). Rifted margin architecture and crustal rheology: Reviewing Iberia-Newfoundland, Central South Atlantic, and South China Sea. Marine and Petroleum Geology, 79, 257–281. https://doi.org/10.1016/j.marpetgeo.2016.10.018

Brune, S., Heine, C., Pérez-Gussinyé, M., & Sobolev, S. V. (2014). Rift migration explains continental margin asymmetry and crustal hyper-extension. Nature Communications, 5, 4014. https://doi.org/10.1038/ncomms5014

Brune, S., Popov, A. A., & Sobolev, S. V. (2012). Modeling suggests that oblique extension facilitates rifting and continental break-up. Journal of Geophysical Research: Solid Earth, 117(B8). https://doi.org/10.1029/2011JB008860

Brune, S., Popov, A. A., & Sobolev, S. V. (2013). Quantifying the thermo-mechanical impact of plume arrival on continental break-up. Tectonophysics, 604, 51–59. https://doi.org/10.1016/j.tecto.2013.02.009

Brune, S., Williams, S. E., Butterworth, N. P., & Müller, R. D. (2016). Abrupt plate accelerations shape rifted continental margins. Nature, 536(7615), 201. https://doi.org/10.1038/nature18319

Bürgmann, R., & Dresen, G. (2008). Rheology of the Lower Crust and Upper Mantle: Evidence from Rock Mechanics, Geodesy, and Field Observations. Annu. Rev. Earth Planet. Sci., 36(1), 531–567. https://doi.org/10.1146/annurev.earth.36.031207.124326

Burlini, L., & Bruhn, D. (2005). High-strain zones: laboratory perspectives on strain softening during ductile deformation. Geological Society, London, Special Publications, 245(1), 1–24. https://doi.org/10.1002/2017JB014333

Clift, P. D., Brune, S., & Quinteros, J. (2015). Climate changes control offshore crustal structure at South China Sea continental margin. Earth and Planetary Science Letters, 420, 66–72. https://doi.org/10.1016/j.epsl.2015.03.032

Cook, A. C., Vel, S. S., Gerbi, C., & Johnson, S. E. (2014). Computational analysis of nonlinear creep of polyphase aggregates: Influence of phase morphology. Journal of Geophysical Research B: Solid Earth, 119(9), 6877–6906. https://doi.org/10.1002/2014JB011197

Corti, G., van Wijk, J., Cloetingh, S., & Morley, C. K. (2007). Tectonic inheritance and continental rift architecture: Numerical and analogue models of the East African Rift system. Tectonics, 26(6). https://doi.org/10.1029/2006TC002086

Coyan, M. M., Arrowsmith, J. R., Umhoefer, P., Coyan, J., Kent, G., Driscoll, N., & Gutíerrez, G. M. (2013). Geometry and quaternary slip behavior of the San Juan de los Planes and Saltito fault zones, Baja California Sur, Mexico: Characterization of rift-margin normal faults. Geosphere, 9(3), 426–443. https://doi.org/10.1130/GES00806.1

Crameri, F. (2018). Geodynamic diagnostics, scientific visualisation and StagLab 3.0. Geoscientific Model Development Discussions, (February), 1–41. https://doi.org/10.5194/gmd-2017-328

Cross, A. J., Ellis, S., & Prior, D. J. (2015). A phenomenological numerical approach for investigating grain size evolution in ductiley deforming rocks. Journal of Structural Geology, 76, 22–34. https://doi.org/10.1016/j.jsg.2015.04.001

Cross, A. J., & Skemer, P. (2017). Ultramylonite generation via phase mixing in high-strain experiments. Journal of Geophysical Research: Solid Earth, 122(3), 1744–1759. https://doi.org/10.1002/2016JB013801

Cyprych, D., Brune, S., Piazolo, S., & Quinteros, J. (2016). Strain localization in polycrystalline material with second phase particles: Numerical modeling with application to ice mixtures. Geochemistry, Geophysics, Geosystems, 17(9), 3608–3628. https://doi.org/10.1002/2016GC006471

Dannberg, J., & Heister, T. (2016). Compressible magma/mantle dynamics: 3-D, adaptive simulations in ASPECT. Geophysical Journal International, 207(3), 1343–1366. https://doi.org/10.1093/gji/ggw329

De Borst, R., & Mühlhaus, H. B. (1992). Gradient-dependent plasticity: Formulation and algorithmic aspects. International Journal for Numerical Methods in Engineering, 35(3), 521–539. https://doi.org/10.1002/nme.1620350307

De Bresser, J. H. P., Ter Heege, J. H., & Spiers, C. J. (2001). Grain size reduction by dynamic recrystallization: Can it result in major rheological weakening? International Journal of Earth Sciences, 90(1), 28–45. https://doi.org/10.1007/s005310000149

Dimanov, A., & Dresen, G. (2005). Rheology of synthetic anorthite-diopside aggregates: Implications for ductile shear zones. Journal of Geophysical Research: Solid Earth, 110(B7). https://doi.org/10.1029/2004JB003431

Duesterhoeft, E., Quinteros, J., Oberhänsli, R., Bousquet, R., & de Capitani, C. (2014). Relative impact of mantle densification and eclogitization of slabs on subduction dynamics: A numerical thermodynamic/thermokinematic investigation of metamorphic density evolution. Tectonophysics, 637, 20–29. https://doi.org/10.1016/j.tecto.2014.09.009

Duretz, T., Petri, B., Mohn, G., Schmalholz, S. M., Schenker, F. L., & Müntener, O. (2016). The importance of structural softening for the evolution and architecture of passive margins. Scientific Reports, 6(38704). https://doi.org/10.1038/srep38704

Duretz, T., Schmalholz, S. M., & Podladchikov, Y. Y. (2015). Shear heating-induced strain localization across the scales. Philosophical Magazine, 95(28–30), 3192–3207. https://doi.org/10.1080/14786435.2015.1054327

Foley, B. J. (2018). On the dynamics of coupled grain size evolution and shear heating in lithospheric shear zones. Physics of the Earth and Planetary Interiors, 283, 7–25fol. https://doi.org/10.1016/j.pepi.2018.07.008

Fossen, H., & Cavalcante, G. C. G. (2017). Shear zones – A review. Earth-Science Reviews, 171, 434–455. https://doi.org/10.1016/j.earscirev.2017.05.002

Gardner, R., Piazolo, S., Evans, L., & Daczko, N. (2017). Patterns of strain localization in heterogeneous, polycrystalline rocks – a numerical perspective. Earth and Planetary Science Letters, 463, 253–265. https://doi.org/10.1016/j.epsl.2017.01.039

Gerbi, C., Johnson, S. E., Cook, A., & Vel, S. S. (2015). Effect of phase morphology on bulk strength for power-law materials. Geophysical Journal International, 200(1), 374–389. https://doi.org/10.1093/gji/ggu388

Handy, M. R. (1989). Deformation regimes and the rheological evolution of fault zones in the lithosphere: the effects of pressure, temperature, grainsize and time. Tectonophysics, 163(1–2), 119–152. https://doi.org/10.1016/0040-1951(89)90122-4

Handy, M. R., Mulch, A., Rosenau, M., & Rosenberg, C. L. (2001). The role of fault zones and melts as agents of weakening, hardening and differentiation of the continental crust: a synthesis. Geological Society, London, Special Publications, 186(1), 305–332. https://doi.org/10.1144/GSL.SP.2001.186.01.18

Heine, C., & Brune, S. (2014). Oblique rifting of the equatorial atlantic: Why there is no saharan atlantic ocean. Geology, 42(3), 211–214. https://doi.org/10.1130/G35082.1

Heitzmann, P. (1987). Calcite mylonites in the central root zone. Tectonophysics, 135(1–3), 207–215. https://doi.org/10.1016/0040-1951(87)90162-4

Herwegh, M., Berger, A., & Ebert, A. (2005). Grain coarsening maps: A new tool to predict microfabric evolution of polymineralic rocks. Geology, 33(10), 801–804. https://doi.org/10.1130/G21789.1

Herwegh, M., Poulet, T., Karrech, A., & Regenauer-Lieb, K. (2014). From transient to steady state deformation and grain size: A thermodynamic approach using elasto-visco-plastic numerical modeling. Journal of Geophysical Research: Solid Earth, 119(2), 900–918. https://doi.org/10.1002/2013JB010701

Herwegh, M., Xiao, X., & Evans, B. (2003). The effect of dissolved magnesium on diffusion creep in calcite. Earth and Planetary Science Letters, 212(3–4), 457–470. https://doi.org/10.1016/S0012-821X(03)00284-X

Hippertt, J. F., & Hongn, F. D. (1998). Deformation mechanisms in the mylonite/ultramylonite transition. Journal of Structural Geology, 20(11), 1435–1448. https://doi.org/10.1016/S0191-8141(98)00047-9

Holyoke, C. W., & Tullis, J. (2006). Mechanisms of weak phase interconnection and the effects of phase strength contrast on fabric development. Journal of Structural Geology, 28(4), 621–640. https://doi.org/10.1016/j.jsg.2006.01.008

Huismans, R. S., & Beaumont, C. (2003). Symmetric and asymmetric lithospheric extension: Relative effects of frictional-plastic and viscous strain softening. Journal of Geophysical Research: Solid Earth, 108(B10). https://doi.org/10.1029/2002JB002026

Jammes, S., Lavier, L. L., & Reber, J. E. (2015). Localization and delocalization of deformation in a bimineralic material. Journal of Geophysical Research: Solid Earth, 120(5), 3649–3663. https://doi.org/10.1002/2015JB011890

Jessell, M. W., Siebert, E., Bons, P. D., Evans, L., & Piazolo, S. (2005). A new type of numerical experiment on the spatial and temporal patterns of localization of deformation in a material with a coupling of grain size and rheology. Earth and Planetary Science Letters, 239(3–4), 309–326. https://doi.org/10.1016/j.epsl.2005.03.030

Ji, S., Jiang, Z., Rybacki, E., Wirth, R., Prior, D., & Xia, B. (2004). Strain softening and microstructural evolution of anorthite aggregates and quartz-anorthite layered composites deformed in torsion. Earth and Planetary Science Letters, 222(2), 377–390. https://doi.org/10.1016/j.epsl.2004.03.021

Kenkmann, T., & Dresen, G. (1998). Stress gradients around porphyroclasts: palaeopiezometric estimates and numerical modelling. Journal of Structural Geology, 20(213), 163–173. https://doi.org/10.1016/S0191-8141(97)00074-6

Kenkmann, T., & Dresen, G. (2002). Dislocation microstructure and phase distribution in a lower crustal shear zone - An example from the Ivrea-Zone, Italy. International Journal of Earth Sciences, 91(3), 445–458. https://doi.org/10.1007/s00531-001-0236-9

Kilian, R., Heilbronner, R., & Stünitz, H. (2011). Quartz grain size reduction in a granitoid rock and the transition from dislocation to diffusion creep. Journal of Structural Geology, 33(8), 1265–1284. https://doi.org/10.1016/j.jsg.2011.05.004

Koopmann, H., Brune, S., Franke, D., & Breuer, S. (2014). Linking rift propagation barriers to excess magmatism at volcanic rifted margins. Geology, 42(12), 1071–1074. https://doi.org/10.1130/G36085.1

Linckens, J., Herwegh, M., Mntener, O., & Mercolli, I. (2011). Evolution of a polymineralic mantle shear zone and the role of second phases in the localization of deformation. Journal of Geophysical Research: Solid Earth, 116(B6). https://doi.org/10.1029/2010JB008119

Mancktelow, N. S. (2002). Finite-element modelling of shear zone development in viscoelastic materials and its implications for localisation of partial melting. Journal of Structural Geology, 24(6–7), 1045–1053. https://doi.org/10.1016/S0191-8141(01)00090-6

Mancktelow, N. S., & Pennacchioni, G. (2005). The control of precursor brittle fracture and fluid-rock interaction on the development of single and paired ductile shear zones. Journal of Structural Geology, 27(4), 645–661. https://doi.org/10.1016/j.jsg.2004.12.001

Mazzotti, S., & Gueydan, F. (2017). Control of tectonic inheritance on continental intraplate strain rate and seismicity. Elsevier. https://doi.org/10.1016/j.tecto.2017.12.014

Misra, S., & Mandal, N. (2007). Localization of plastic zones in rocks around rigid inclusions: Insights from experimental and theoretical models. Journal of Geophysical Research: Solid Earth, 112(B9). https://doi.org/10.1029/2006JB004328

Nardini, L., Rybacki, E., Döhmann, M. J., Morales, L. F., Brune, S., & Dresen, G. (2018). High-temperature shear zone formation in Carrara marble: The effect of loading conditions. Tectonophysics, 749, 120-139. https://doi.org/10.1016/j.tecto.2018.10.022

Okada, Y. (1985). Surface deformation due to shear and tensile faults in a half-space. Bulletin of the Seismological Society of America, 75(4), 1135–1154.

Palin, R. M., Searle, M. P., St-Onge, M. R., Waters, D. J., Roberts, N. M. W., Horstwood, M. S. A., … Weller, O. M. (2014). Two-stage cooling history of pelitic and semi-pelitic mylonite (sensu lato) from the Dongjiu-Milin shear zone, northwest flank of the eastern Himalayan syntaxis. Gondwana Research, 28(2), 509–530. https://doi.org/10.1016/j.gr.2014.07.009

Park, M., & Jung, H. (2017). Microstructural evolution of the Yugu peridotites in the Gyeonggi Massif, Korea: Implications for olivine fabric transition in mantle shear zones. Tectonophysics, 709, 55–68. https://doi.org/10.1016/j.tecto.2017.04.017

Paterson, M. S. (1970). A high-pressure, high-temperature apparatus for rock deformation. International Journal of Rock Mechanics and Mining Sciences And, 7(5), 517–526. https://doi.org/10.1016/0148-9062(70)90004-5

Paterson, M. S., & Olgaard, D. L. (2000). Rock deformation tests to large shear strains in torsion. Journal of Structural Geology, 22(9), 1341–1358. https://doi.org/10.1016/S0191-8141(00)00042-0

Pearce, M. A., Wheeler, J., & Prior, D. J. (2011). Relative strength of mafic and felsic rocks during amphibolite facies metamorphism and deformation. Journal of Structural Geology, 33(4), 662-675. https://doi.org/10.1016/j.jsg.2011.01.002

Pieri, M., Burlini, L., Kunze, K., Stretton, I., & Olgaard, D. L. (2001). Rheological and microstructural evolution of Carrara marble with high shear strain: results from high temperature torsion experiments. Journal of Structural Geology, 23(9), 1393–1413. https://doi.org/10.1016/S0191-8141(01)00006-2

Pieri, M., Kunze, K., Burlini, L., Stretton, I., Olgaard, D. L., Burg, J.-P., & Wenk, H.-R. (2001). Texture development of calcite by deformation and dynamic recrystallization at 1000 K during torsion experiments of marble to large strains. Tectonophysics, 330(1–2), 119–140. https://doi.org/10.1016/S0040-1951(00)00225-0

Popov, A. A., & Sobolev, S. V. (2008). SLIM3D: A tool for three-dimensional thermomechanical modeling of lithospheric deformation with elasto-visco-plastic rheology. Physics of the Earth and Planetary Interiors, 171((1-4)), 55–75. https://doi.org/10.1016/j.pepi.2008.03.007

Popov, A. A., Sobolev, S. V., & Zoback, M. D. (2012). Modeling evolution of the San Andreas Fault system in northern and central California. Geochemistry, Geophysics, Geosystems, 13(8). https://doi.org/10.1029/2012GC004086

Quinteros, J., & Sobolev, S. V. (2013). Why has the Nazca plate slowed since the Neogene? Geology, 41(1), 31–34. https://doi.org/10.1130/G33497.1

Quinteros, J., Sobolev, S. V., & Popov, A. A. (2010). Viscosity in transition zone and lower mantle: Implications for slab penetration. Geophysical Research Letters, 37(9). https://doi.org/10.1029/2010GL043140

Rybacki, E., Morales, L. F. G., Naumann, M., & Dresen, G. (2014). Strain localization during high temperature creep of marble: The effect of inclusions. Tectonophysics, 634, 182–197. https://doi.org/10.1016/j.tecto.2014.07.032

Schmeling, H., Marquart, G., & Grebe, M. (2018). A porous flow approach to model thermal non-equilibrium applicable to melt migration. Geophysical Journal International, 212(1), 119–138. https://doi.org/10.1093/gji/ggx406

Schmid, S. M., Boland, J. N., & Paterson, M. S. (1977). Superplastic flow in finegrained limestone. Tectonophysics, 43(3–4), 257–291. https://doi.org/10.1016/0040-1951(77)90120-2

Schmid, S. M., Paterson, M. S., & Boland, J. N. (1980). High temperature flow and dynamic recrystallization in Carrara marble. Tectonophysics, 65(3–4), 245–280. https://doi.org/10.1016/0040-1951(80)90077-3

Simo, J. C., & Hughes, T. J. (2006). Computational inelasticity (Vol. 7). Springer Science & Business Media.

Tasaka, M., Zimmerman, M. E., Kohlstedt, D. L., Stünitz, H., & Heilbronner, R. (2017). Rheological Weakening of Olivine + Orthopyroxene Aggregates Due To Phase Mixing: Part 2. Microstructural Development. Journal of Geophysical Research: Solid Earth, 122(10), 7597–7612. https://doi.org/10.1002/2017JB014311

Ter Heege, J. H., De Bresser, J. H. P., & Spiers, C. J. (2001). The influence of dynamic recrystallization on the grain size distribution and rheological behaviour of Carrara marble deformed in axial compression. Geological Society, London, Special Publications, 200(1), 331–353. https://doi.org/10.1144/GSL.SP.2001.200.01.19

Thielmann, M., & Kaus, B. J. P. (2012). Shear heating induced lithospheric-scale localization: Does it result in subduction? Earth and Planetary Science Letters, 359, 1–13. https://doi.org/10.1016/j.epsl.2012.10.002

Treagus, S. H., & Lan, L. (2004). Deformation of square objects and boudins. Journal of Structural Geology, 26(8), 1361–1376. https://doi.org/10.1016/j.jsg.2003.12.002

Valoroso, L., Chiaraluce, L., Piccinini, D., Di Stefano, R., Schaff, D., & Waldhauser, F. (2013). Radiography of a normal fault system by 64,000 high-precision earthquake locations: The 2009 L'Aquila (central Italy) case study. Journal of Geophysical Research: Solid Earth, 118(3), 1156–1176. https://doi.org/10.1002/jgrb.50130

Warren, J. M., & Hirth, G. (2006). Grain size sensitive deformation mechanisms in naturally deformed peridotites. Earth and Planetary Science Letters, 248(1–2), 423–435. https://doi.org/10.1016/j.epsl.2006.06.006

Webber, S., Ellis, S., & Fagereng, Å. (2018). "Virtual shear box" experiments of stress and slip cycling within a subduction interface mélange. Earth and Planetary Science Letters, 488, 27–35. https://doi.org/10.1016/j.epsl.2018.01.035

White, S. (1976). A Discussion on natural strain and geological structure - The effects of strain on the microstructures, fabrics, and deformation mechanisms in quartzites. Philosophical Transactions for the Royal Society of London A., 283(1312), 69–86. https://doi.org/10.1098/rsta.1976.0070

Zang, A., Wagner, F. C., Stanchits, S., Janssen, C., & Dresen, G. (2000). Fracture process zone in granite. Journal of Geophysical Research: Solid Earth, 105(B10), 23651–23661. https://doi.org/10.1029/2000JB900239

4 Controls on Asymmetric Rift Dynamics: Numerical Modeling of Strain Localization and Fault Evolution in the Kenya Rift

Richter, M. J. E. A., Brune, S., Riedl, S., Glerum, A., Neuharth, D., & Strecker, M. R.

2021

Tectonics, *40*(5)

https://doi.org/10.1029/2020TC006553

Key Points

- 2D numerical models elucidate evolution of asymmetric Kenya Rift segments
- Intrabasinal faulting is caused by bending of the central block and does not reach the brittle-ductile transition
- Small-scale crustal inheritance can exert decisive control on first-order rift architecture

Abstract

Complex, time-dependent, and asymmetric rift geometries are observed throughout the East African Rift System (EARS) and are well documented, for instance, in the Kenya Rift. To unravel asymmetric rifting processes in this region, we conduct 2D geodynamic models. We use the finite element software ASPECT employing visco-plastic rheologies, mesh-refinement, distributed random noise seeding, and a free surface. In contrast to many previous numerical modeling studies that aimed at understanding final rifted margin symmetry, we explicitly focus on initial rifting stages to assess geodynamic controls on strain localization and fault evolution. We thereby link to geological and geophysical observations from the Southern and Central Kenya Rift. Our models suggest a three-stage early rift evolution that dynamically bridges previously inferred fault-configuration phases of the eastern EARS branch: (1) accommodation of initial strain localization by a single border fault and flexure of the hanging-wall crust, (2) faulting in the hanging-wall and increasing upper-crustal faulting in the rift-basin center, and (3) loss of pronounced early stage asymmetry prior to basinward localization of deformation. This evolution may provide a template for understanding early extensional faulting in other branches of the East African Rift and in asymmetric rifts worldwide. By modifying the initial random noise distribution that approximates small-scale tectonic inheritance, we show that a spectrum of first-order fault configurations with variable symmetry can be produced in models with an otherwise identical setup. This approach sheds new light on along-strike rift variability controls in active asymmetric rifts and proximal rifted margins.

4.1 Introduction

Asymmetric rifting, which is characterized by a dominant single border fault, is known to have played a major role in the evolution of many past rift systems (e.g., Schlische et al., 2003; Withjack et al., 2013). It can also be observed in many presently active extensional tectonic settings (e.g., Gawthorpe & Leeder, 2008; Ebinger & Scholz, 2011), where it governs basin geometry, topography evolution, erosion, and sedimentation patterns. One such setting is the largest continental rift system in existence today: the East African Rift System (EARS). It exhibits a wide array of developmental stages from youthful extension with incipient faulting to final continental breakup (Corti, 2009; Ebinger & Scholz, 2011; Ring, 2014) and is thus an ideal location for studying the stages of early rifting that involve asymmetric normal fault activity followed by hanging-wall segmentation. In this study, we focus on the southern and central sectors of the Kenya Rift, which are in an early phase of active continental rifting (Ebinger et al., 2017) characterized by the transition from waning border fault activity to enhanced intra-basinal faulting and subsidence (Muirhead et al., 2016).

The first-order tectonic characteristics of continental rifts are known to be influenced by a large range of structural, petrological, and thermal parameters, which have been

investigated in previous numerical modeling studies (e.g., Armitage et al., 2018; Duretz et al., 2016; Huismans & Beaumont, 2011; Jammes & Lavier, 2019; Naliboff et al., 2017; Petersen & Schiffer, 2016). It is evident that, in addition to the rheological characteristics of crust and mantle (thickness, composition and intrinsic heterogeneity), the thermal structure, which includes the effects of radiogenic heating, plays a major role in rift evolution (e.g., Burov & Schubert, 2007). Depending on these parameters, either wide or narrow (e.g., Brun, 1999; Buck et al., 1999) and either symmetric or asymmetric rifts (Buiter et al., 2008; Huismans and Beaumont, 2003) may form. Although the above processes dictate the principal rift setting, the location, orientation, and geometry of the initial fault systems may be strongly affected by pre-existing structures and fabrics associated with suture zones (e.g., Corti, 2009; Corti et al., 2007; Delvaux et al., 2012; Hodge et al., 2018; Phillips et al., 2016; Shackleton, 1993; Smith & Mosley, 1993).

The structural evolution of continental rifts is controlled to a large degree by the influence of tectonic and magmatic processes (e.g., Buck et al., 2005) whose impact can be sketched by considering two end-members: (1) In magma-assisted rifts, such as in the Afar region (Kendall et al., 2005), dikes and other magmatic intrusions accommodate the majority of overall extensional deformation (Bastow & Keir, 2011) and play a vital role in achieving continental breakup (Wright et al., 2006). (2) Conversely, in tectonically dominated rifts, deformation is accommodated by faults while only a minor part of the extensional deformation is related to magmatic processes (e.g., Petit & Deverchere, 2006; Schumacher, 2002; Schwarz & Henk, 2005;). The eastern branch of the EARS, however, does not clearly belong to one of these end-member cases as upper crustal extension is accommodated by a combination of normal faulting and diking (Calais et al., 2008; Muirhead et al. 2015; Oliva et al., 2019). Voluminous lava flows that testify to widespread thermal processes and volcanic activity are documented throughout the history of the eastern branch (Rooney, 2020). Nevertheless, the details of how magmatic contributions influence the development of first-order tectonic structures in this area are not well understood.

Many numerical modeling studies have focused on continental margins (e.g., Bassi, 1991; Brune et al., 2014; Huismans & Beaumont, 2011; Salazar-Mora et al., 2018; Svartman Dias et al., 2015; Tetreault & Buiter, 2018), while analogue modeling techniques have largely been used to study the structural evolution of active continental rifts and their geodynamic causes (e.g., Corti, 2012; Khalil et al., 2020; Sokoutis et al., 2007; Zwaan et al. 2019). The reason why analogue techniques are often preferred in these settings is the comparably high spatial resolution that allows the details of the evolution of normal-fault networks to be captured, especially during early rifting where crustal thinning is limited. In contrast, the advantage of numerical models lies in their ability to reproduce the temperature- and strain-rate-dependent rheological evolution of the lithosphere, which is particularly important during the necking and crustal hyper-extension phases that have shaped many rifted margins worldwide (Jeanniot & Buiter, 2018; Péron-Pinvidic et al., 2019). Hence, only a small number of numerical geodynamic modeling studies have

focused on active continental rifts (e.g., Beutel et al., 2010; Corti et al; 2019; Muluneh et al., 2020), and many of those studies have addressed either large-scale processes of rifting and the driving forces responsible (Kendall & Lithgow-Bertelloni, 2016; Stamps et al., 2015; Ulvrova et al., 2019) or the interaction between volcanism and mantle dynamics (Armitage et al., 2018; Civiero et al, 2019; Koptev et al., 2018). Nevertheless, significant insights into the early stages of the structural evolution of rifts may be gained from studying individual sectors of active rifts and comparing geological information and interpretations of tectonic evolution with numerical models. This holds especially true for the effects of rheology, thermal structure, and inheritance on localization patterns, geometry, and timing of faults, and the resulting interaction between magmatic and structural processes.

In this study, we employ numerical 2D forward models to analyze the evolution of early rift stages. We establish a reference model that reproduces major aspects of the Southern and Central Kenya Rifts, where a good coverage of geological and geophysical data is available. Our aim is to understand how and why an asymmetric, narrow rift forms in this particular geological setting and to discuss its tectonic evolution.

4.2 Geological Background

The Kenya Rift (36°E, 3°N to 2°S), where asymmetric and symmetric rift geometries are observed, exhibits many key aspects of rift evolution (Figure 1). It is a slowly spreading, active continental rift, with a present-day extension rate of ~2 mm a^{-1} (e.g., Saria et al., 2014). The Kenya Rift is part of the eastern branch of the EARS and is located within the nascent plate boundary between the Somalia and Victoria plates (Stamps et al., 2008; Figure 1a). Major east-dipping normal faults on the western side of the rift and normal faults with lesser throws that cut the eastern flanks of the rift led to the formation of a pronounced basin with an average width of 60–70 km (Figure 1b). The interior of this basin, however, became increasingly dissected by arrays of closely spaced, low-offset normal faults that delimit a tectonically active depression (Baker et al., 1988), which constitutes an inner graben.

Based on the overall fault geometry, our study region (Figure 1b) can be divided into two sectors. The first consists of the asymmetric north-northeast-oriented Southern Kenya Rift with one major border fault along the Nguruman Escarpment in the west, and a ~50 km wide and densely faulted inner rift sector, which slopes gently toward the west. The eastern side of the Southern Kenya Rift is bordered by the prominent Ngong-Turoka Escarpment, which constitutes an antithetically faulted flank (Baker et al., 1988; Smith, 1994). The second sector consists of the asymmetric northwest-oriented Central Kenya Rift (Figure 1b) with the Mau Escarpment on the west and the antithetic Sattima and Kinangop faults on the east (Baker et al., 1988; Shackleton, 1945). Overall, fewer secondary faults are exposed in this region due to the masking effect of ubiquitous Quaternary pyroclastic deposits.

Across the Nguruman Fault at the western flank of the Southern Kenya Rift, elevation decreases from ~1800 m at the rift shoulder to ~600 m at the rift floor (e.g., Baker, 1958; Crossley, 1979). The fault has an approximate dip of 60°–65° E at the surface and appears to be shallowing slightly at depth as suggested by local seismicity (Lee et al., 2016; Weinstein et al., 2017). In contrast, the eastern rift flank has a less pronounced relief and exposes westward-dipping Neogene volcanics (Pliocene Trachytes; Baker et al., 1988; Randel & Johnson, 1970) of the Ngong-Turoka Escarpment, with a height of at least 350 m above the downfaulted equivalents of the Pliocene Trachytes within the rift that are exposed at the surface (Baker & Mitchell, 1976). Farther basinward of these outcrops, elevation decreases along densely spaced, rift-parallel horst-and-graben structures, which characterize the entire area from the eastern side of the rift to the basin floor in the Magadi area. The current depocenter and sediment sink of the Southern Kenya Rift is the Magadi-Natron lake basin at ~600 m elevation, situated between the rift center and the western border fault (Figure 1).

4.2.1 Timing of Rifting

The present-day configuration of the Southern and Central Kenya Rift is associated with extensional processes that began during the Miocene (e.g., Shackleton, 1978; Tiercelin & Lezzar, 2002). However, thermochronological, geophysical, and sedimentary evidence for a preceding rifting episode during the Paleocene–Eocene exists immediately north of the equator in the transition between the Central and the Northern Kenya Rift (e.g., Ego, 1994; Hautot et al., 2000; Mugisha et al., 1997; Torres Acosta et al., 2015).

The onset of Miocene extensional faulting in the Central Kenya Rift was closely linked with the emplacement of extensive phonolite flows (Shackleton, 1945; Baker et al., 1971; 1988; Lippard, 1973) that were deposited in a shallow, wide depression (Lippard 1973; Figure 1c, blue Miocene units). This depression existed at 14.5 Ma, as it unconformably encloses flood phonolites of that age that overspilled these areas and flowed away from the future rift area (Lippard 1973; Williams, 1972; Wichura et al., 2010; 2015). These areally extensive flood phonolites are widespread on the shoulders of the Central Kenya Rift (mainly mapped as Middle Miocene Plateau Phonolites), where they serve as important strain markers. The earliest faults cutting these Middle Miocene Plateau Phonolites were active at the western side of the present-day rift in the transition to the Northern Kenya Rift, documenting the onset of down-to-the-east normal faulting and the formation of a halfgraben between 14.5 Ma and 12 Ma at ~1° N (Chapman & Brook, 1978; Hetzel and Strecker, 1994; Morley et al., 1992; Mugisha et al., 1997), which is also reflected by thermochronological records showing a rapid cooling phase beginning at that time (Torres Acosta et al., 2015). These fault scarps prevented subsequent lavas flows of the Upper Miocene Flood Phonolites and Trachytes from overflowing the rift toward the west (Baker et al., 1971; Crossley, 1979). In the Central Kenya Rift this halfgraben geometry is associated with the east-dipping normal faults that constitute the Mau Escarpment (Clarke et al., 1990; Figure 1). An asymmetric geometry can be

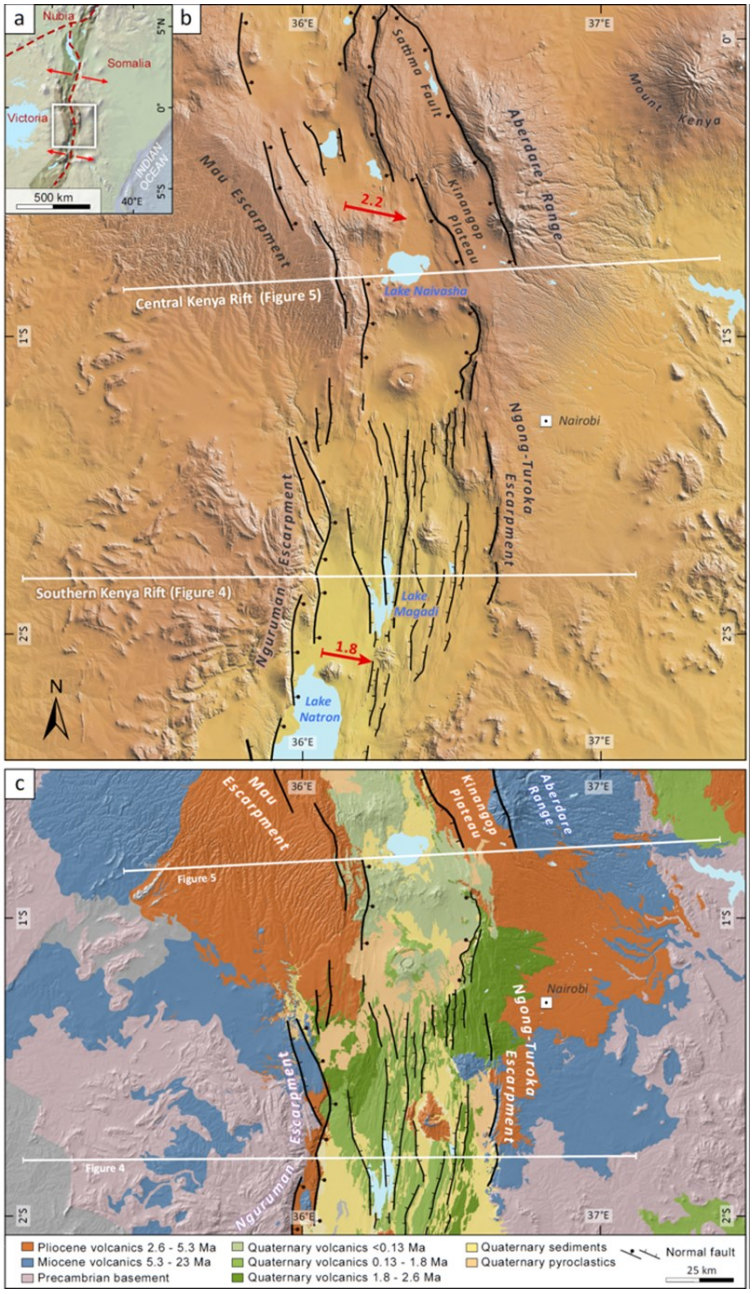

Figure 4. *(a) Plate-tectonic overview and (b) simplified map of the Southern and Central Kenya Rift with normal faults (black), location of cross sections (white), and present-day full extension velocities (red arrows) in mm a^{-1} (based on Saria et al., 2014). The Southern Kenya Rift extends from ~2.5° to ~1°S and is bounded by the Nguruman Escarpment to the west. The Central Kenya Rift is bounded by the Mau Escarpment and extends from ~1°S to ~2.5°N (not shown on this map). Ball-and-bar symbol denotes important faults with throws > 500 m, mainly along the western rift-bounding border faults and the Sattima Fault of the central segment. The local extension direction is nearly rift-perpendicular in the area of the analyzed cross sections, justifying a 2D modeling approach, although evidence for oblique extension exists in the Central Kenya Rift (Zielke & Strecker, 2009). (c) Geological overview of the study area (based on the Geological map of Kenya, 1987, and Guth, 2014). The geology of the rift shoulders is shown without Quaternary sedimentary and volcanic air-fall covers.*

unambiguously documented using the ubiquitous occurrence of the Mio-Pliocene Plateau Trachytes that are exposed at 2,700 m elevation on the eastern (Saggerson, 1970) and western (Williams, 1969a) rift shoulders and at ~2500 m on the fault-bounded intrarift Kinangop Plateau (Figure 1; Baker et al., 1971; 1988); in contrast, this unit has been downfaulted by 1000 m along the Mau Escarpment with a pronounced westward dip that indicates the dominance of the western border fault during asymmetric rifting (Clarke et al., 1990).

At the present-day eastern side of the Central Kenya Rift, Early Pliocene faulting generated throws between 500 and 700 m along the west-dipping Sattima Fault (Figure 1) testifying the transition to a morphologic full-graben stage (e.g., Shackleton, 1945). This was followed by normal faulting farther west prior to 2.6 Ma that form the array of faults bounding the Kinagop Plateau to the west and delimiting the ~40-km-wide inner graben (Baker et al., 1988; Clarke et al. 1990). Due to the sustained subsidence along faults that bound the inner graben, the areal extent of volcanic and sedimentary units became increasingly limited with decreasing age. As such, Quaternary volcano-sedimentary units are areally restricted to the inner graben, which has been the focus of densely spaced normal normal faulting that has resulted in a horst-and-graben landscape (Hackman, 1988; McCall, 1967; Thompson & Dodson, 1963). Furthermore, the inner graben has been characterized by volcanic, seismic, and hydrothermal activity during the last 2 Ma (Clarke et al., 1990; Riedl et al., 2020; Tongue et al., 1992).

The first manifestations of extensional tectonism in the Southern Kenya Rift are documented at <10 Ma (Crossley, 1979) along the western Nguruman Escarpment, whereas the eastern rift border along the Ngong-Turoka Escarpment was faulted only during the Pliocene (Baker & Mitchell, 1976; Saggerson, 1991). Over time, fault activity migrated from the Nguruman Escarpment eastward to the Lake Magadi basin in the center of the rift (Baker, 1958; Crossley, 1979). Here, the youngest volcanic units are the 0.95 to 1.37 million-year-old Magadi Trachytes that are confined to the inner graben (Baker et al. 1971), and stratigraphically equivalent trachyte flows occur throughout the Kenya Rift in similar, fault-bounded structural settings. All of these units are affected by densely spaced normal faults (e.g., Baker et al., 1988; Muirhead et al., 2016) that define the seismically active volcano-tectonic axis of the rift. In the Magadi area young tectonic activity is documented by small-offset normal-faults (e.g., Hillaire-Marcel et al., 1986; Muirhead et al., 2016) and numerous extensional cracks that strike parallel to the Quaternary normal faults. Extensional cracks generated during recent earthquakes at the rift floor (Atmaoui & Hollnack, 2003; Muirhead and Kattenhorn, 2018) and pronounced seismic activity (Ibs-von Seht et al., 2001; Weinstein et al., 2017) in the Magadi area document that extensional processes are active today.

4.3 Numerical Model Setup

Here, we employ numerical forward models to investigate the early-stage evolution of asymmetric continental rifting. In doing so, the finite element software ASPECT (Advanced Solver for Problems in Earth's ConvecTion) (Bangerth et al., 2018, 2019; Heister et al., 2017; Kronbichler et al., 2012) is used to solve the thermomechanically coupled conservation equations of momentum (Equation 1), mass (Equation 2), energy (Equation 3), combined with additional advection equations for each Eulerian compositional field c_i, (Equation 4):

$$-\nabla \cdot (2\eta\dot{\varepsilon}) + \nabla P = \rho \mathbf{g} \tag{1}$$

$$\nabla \cdot (\mathbf{v}) = 0 \tag{2}$$

$$\begin{aligned} \bar{\rho} c_P \left(\frac{\partial T}{\partial t} + \mathbf{v} \cdot \nabla T\right) - \nabla \cdot \kappa \nabla T = \bar{\rho} H & \quad \text{radioactive heating} \\ + (2\eta\dot{\varepsilon}) : \dot{\varepsilon} & \quad \text{shear heating} \\ + \alpha T (\mathbf{v} \cdot \nabla P) & \quad \text{adiabatic heating} \end{aligned} \tag{3}$$

$$\frac{\partial c_i}{\partial t} + \mathbf{v} \cdot \nabla c_i = 0 \tag{4}$$

where $\dot{\varepsilon}$ is the deviator of the strain rate tensor $\frac{1}{2}(\nabla \mathbf{v} + (\nabla \mathbf{v})^T)$ with $\mathbf{v}$ the velocity vector. Density is defined as $\rho = \rho_0(1 - \alpha(T - T_0))$ with the thermal expansivity α and the reference temperature T_0, while P is the pressure, $\mathbf{g}$ is the gravity vector, $\bar{\rho}$ is the adiabatic reference density, T is the temperature, κ is the thermal diffusivity and H is radioactive heating. The visco-plastic effective viscosity η_{eff} is computed from either a composite of diffusion and dislocation creep (Equation 5) or Drucker-Prager plasticity (Equation 6; Glerum et al., 2018) depending on whether viscous stresses stay below the yield stress or not.

$$\eta_{eff}^{diff|disl} = \frac{1}{2}\left(\frac{1}{A}\right)^{1/n} \dot{\varepsilon}_e^{(1-n)/n} \exp\left(\frac{Q+PV}{nRT}\right) \tag{5}$$

where $n = 1$ for diffusion creep and $n > 1$ for dislocation creep, and the effective deviatoric strain rate is defined as $\dot{\varepsilon_e} = \sqrt{\frac{1}{2}\dot{\varepsilon_{ij}'}\dot{\varepsilon_{ij}'}}$. Values for prefactor A, activation energy Q, activation volume V, and gas-constant R are given in Table 1. Plastic effective viscosity is given by:

$$\eta_{eff}^{pl} = \frac{C\cos(\phi) + P\sin(\phi)}{2\,\dot{\varepsilon}_e} \tag{6}$$

where C is the cohesion and ϕ the friction angle.

For this study, plastic strain is stored on particles (Gassmöller et al., 2018) to reduce fault width and to avoid numerical diffusion of the strain variable. Parameters are listed in Table 1. Here, we build on previous ASPECT setups that were designed to capture rift

dynamics on a wide range of scales (Corti et al., 2019; Glerum et al., 2020; Heckenbach et al., 2021; Muluneh et al., 2020; Neuharth et al., 2021; Sandiford et al., 2021).

Our 2D models comprise a 500 × 200 km box with up to 500 m elemental resolution. The initial, prerift structure consists of a 22-km-thick upper crustal layer with a wet quartzite rheology, a 16-km-thick lower crustal layer of wet anorthite, an 82-km-thick lithospheric mantle of dry olivine and an 80-km-thick section of asthenospheric mantle comprised of wet olivine (see Table 1 and Figure 2a). Hence, the initial Moho depth is 38 km and lithospheric thickness is 120 km. This particular crustal and mantle geometry is inspired by the gravity and thermal models of Sippel et al. (2017), but chosen such that it reflects estimated pre-rift thicknesses.

We chose a model setup that represents two well-known aspects of East African rifting in a simplified representation:

(1) Structural inheritance. Continental deformation often localizes within zones of past tectonic activity (e.g., Schuhmacher, 2002; Schlische et al., 2003; Withjack et al., 2013), as is also observed within the EARS (Corti et al., 2007; Katumwehe et al., 2015; Macgregor, 2015; Shackleton, 1993; Smith and Mosley, 1993). Especially basement foliations and reactivation of pre-existing structures or fault geometries are involved in defining the deformation patterns (e.g., Corti, 2009; Delvaux et al., 2012; Hetzel and Strecker, 1994; Morley, 2010). In numerical models, these are either incorporated as prescribed, local features (Corti et al., 2003; Brune et al., 2017a; Salazar-Mora et al., 2018) or with some form of random noise (Duclaux et al., 2020; Naliboff et al., 2020) to focus localization of the model. Here, we adopt the latter approach by implementing a zone in the model center of randomized initial strains from 0 to 0.2 (see Figure 2a) using a Gaussian distribution with a width of $2\sigma = 200$ km that is comparable to that of mobile belts (Lenardic et al., 2000; Katumwehe et al., 2015). All differences between the models of this study result from a random seed pattern affecting the distribution of the initial strain within this Gaussian envelope (Figure 2a). Note that the employed random number generator *srand* can yield variable patterns for different library configurations, hence individual model details are currently not reproducable on other computers, only the overall ensemble behaviour. To facilitate localization, we use softening laws for (i) brittle layers (e.g., Brune, 2014; Jourdon et al., 2021; Persaud et al., 2017; Petersen & Schiffer, 2016; Salazar-Mora et al., 2018) and (ii) ductile parts of the crust (e.g., Döhmann et al., 2019; Gerbi et al., 2010; Pérez-Gussinyé et al., 2020) (Table 1). Brittle softening is implemented as a linear decrease of the friction coefficient by up to 90% between accumulated strain values of 0–0.5. It is applied to the upper and lower crust and the lithospheric mantle. Viscous softening on the other hand is implemented as a factor that reduces the effective viscous viscosity by up to 90%, again between accumulated strain values of 0–0.5. It is only applied to the crustal layers.

Table 3. Model parameters.

Parameter	Units	Upper crust	Lower crust	Lithospheric mantle	Asthenospheric mantle
Reference temperature	K	293	293	293	293
Reference density	kg m^{-3}	2700	2850	3280	3300
Adiabatic surface temperature	K	1623	1623	1623	1623
Thermal expansivity	10^{-5} K^{-1}	2.7	2.7	3.0	3.0
Thermal diffusivity	10^{-7} m^2 s^{-1}	7.7160	7.3099	8.3841	8.3333
Heat capacity	J kg^{-1} K^{-1}	1200	1200	1200	1200
Radiogenic heat production	μW m^{-3}	0.5	0.1	0	0
Unweakened friction coefficient		0.5	0.5	0.5	0.5
Cohesion	MPa	20	20	20	20
Rheology		***Wet Quartzite***[a]	***Wet Anorthite***[b]	***Dry Olivine***[c]	***Wet Olivine***[c]
Unweakened pre-exponential constant for diffusion creep	Pa^{-1} s^{-1}	5.97×10^{-19}	2.99×10^{-25}	2.25×10^{-9}	1.5×10^{-9}
Grain size	mm	1.0	1.0	1.0	1.0
Grain size exponent		2.0	3.0	0	0
Activation energy for diffusion creep	kJ mol^{-1}	223	159	375	335
Activation volume for diffusion creep	cm^3 mol^{-1}	0	38.0	6.0	4.0
Unweakened pre-exponential constant for dislocation creep	Pa^{-n} s^{-1}	8.57×10^{-28}	7.13×10^{-18}	6.52×10^{-16}	2.12×10^{-15}
Power law exponent for dislocation creep		4.0	3.0	3.5	3.5
Activation energy for dislocation creep	kJ mol^{-1}	223	345	530	480
Activation volume for dislocation creep	cm^3 mol^{-1}	0	38.0	18.0	11.0
Softening laws					
Maximum friction softening[d]		90%	90%	90%	none
Maximum viscous softening[e]		90%	90%	none	none

[a]Rutter & Brodie (2004), [b]Rybacki et al. (2006), [c]Hirth & Kohlstedt (2003), [d]Linear decrease of friction coefficient by 90% between strain values of 0 and 0.5. [e]Linear decrease of effective viscosity by 90% between strain values of 0 and 0.5.

(2) Changes in thermal regime related to the large-scale impingement of a mantle plume. Evidence for the involvement and timing of a mantle plume in East African extension comes from a wide range of geochemical (Halldórsson et al., 2014; Pik et al., 2006), seismological (Civiero et al., 2015; Green et al., 1991; Mulibo & Nyblade, 201), paleo-topographical (Wichura et al., 2010, 2015), and modeling studies (Koptev et al., 2018; Moucha & Forte, 2011). We account for the plume-affected lithospheric temperature

distribution at the onset of extension through the following scheme: Phase I *(pre-plume*) represents stable, equilibrated conditions using a potential mantle temperature of 1350°C (Rooney et al., 2012) and the lithospheric structure described above starting from a steady-state conductive continental geotherm and an adiabatic temperature increase in the sublithospheric mantle. A temperature increase of the asthenospheric layer due to the arrival of the East-African mantle plume (Hofmann et al., 1997) is simulated in phase II (*pre-rift*) by increasing the bottom temperature boundary condition by 200°C, a generally inferred excess plume temperature (Bunge 2005; Schilling, 1991), which is somewhat higher than values calculated for potential mantle temperatures based on volcanic rocks of the area (Rooney et al., 2012). After 20 Ma of small-scale convection in the asthenosphere, phase III (*syn-rift*) starts by imposing extensional velocities at the model boundaries. During this phase, a narrow rift initiates and evolves. Due to the simplified setup, we did not account for other processes that result from plume impingement like diking or lithospheric erosion from below (e.g., Beniest et al., 2017; Celli et al., 2020; Koptev et al., 2015; Sobolev et al., 2011).

The time-dependent velocity and temperature specifications at the model boundaries are complemented by the following thermal and mechanical boundary conditions: a free surface (Rose et al., 2017) with a constant temperature, and thermal isolation at the model sides. Outflux is prescribed on the left and right boundary and adjusted for each of the model's three phases (see Figure 2); no flow in phase I, strong outflow of up to 10 mm a^{-1} through the left and right sides of the asthenosphere in phase II and 1 mm a^{-1} of outflow through the entire the left and right boundaries in phase III, which reflects estimates of the present-day extension rate in our study region (Saria et al., 2014). In order to conserve model volume, lateral outflow is compensated by prescribed inflow through the bottom boundary.

There are several model limitations that have to be kept in mind when interpreting our results. Our models neither represent magmatic processes like diking and underplating, nor surface processes, dynamic topography, plume-related lithosphere erosion, or 3D effects. Since deeply sourced dynamic topography is excluded from the model, about 1–2 km elevation has to be added when comparing the model results to topography in nature (Faccenna et al., 2019; Moucha & Forte, 2011; Osei Tutu et al., 2018). Another limitation is the uncertainty in radiogenic heat, that has a big impact on deformation patterns and wide or narrow rifting styles (Jaupart et al., 2016), mainly because it affects the thicknesses of the viscous and brittle layers in the upper and lower crust. For the setup of our study we chose the following values for radiogenic heat production: 0.5 µW m^{-3} for the upper crust and 0.1 µW m^{-3} for the lower crust (Jaupart et al., 2016).

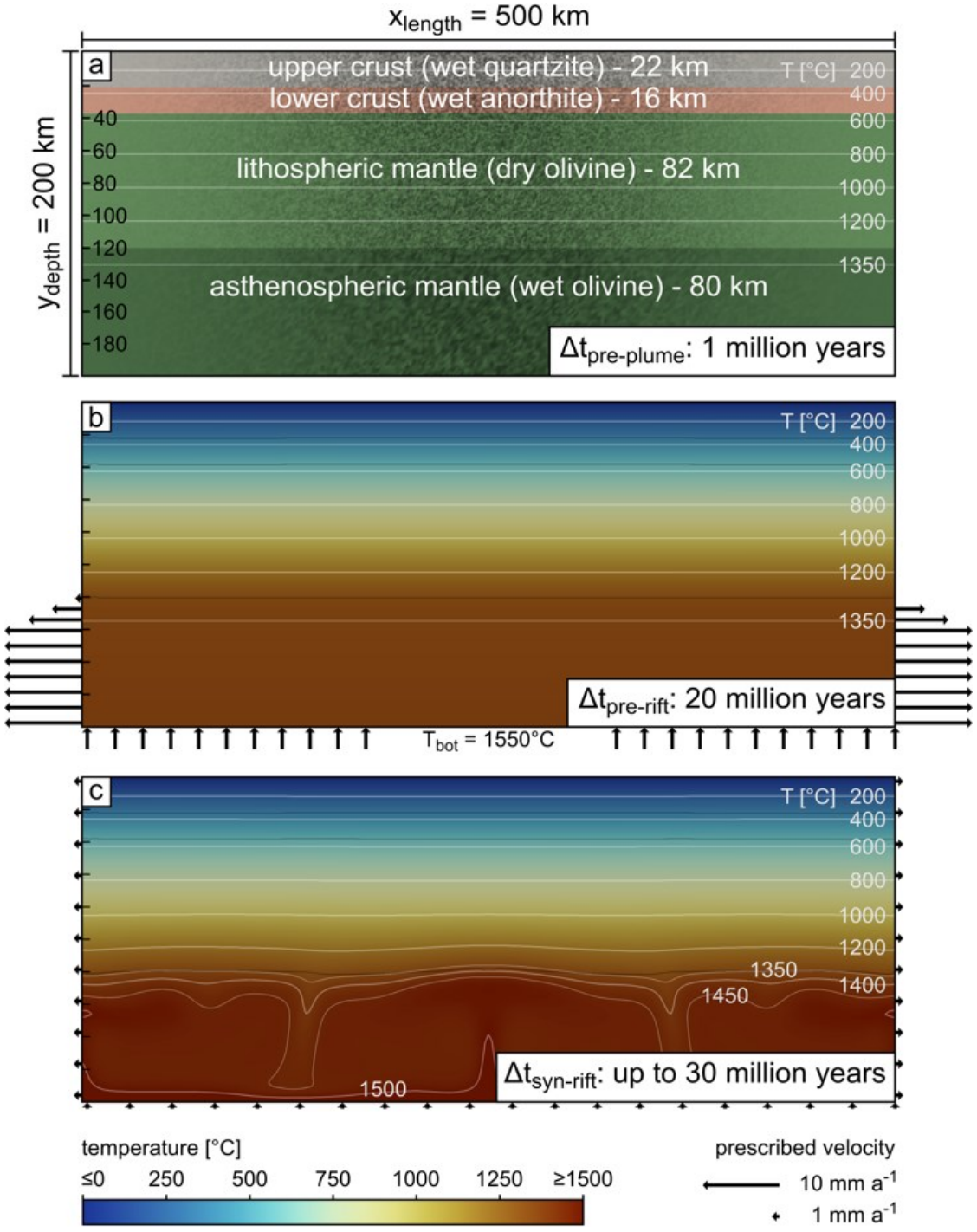

Figure 5. *Setup of the numerical model at the start of each of the three model phases. (a) Phase I (pre-plume): Thermally equilibrated setup with prescribed boundary velocities of zero, modeled time: 1 million years. Strain is seeded using a Gaussian distribution of amplitude 0.2 at random locations (dark areas in model center) simulating structural inheritance and breaking model symmetry, to facilitate and focus localization. (b) Phase II (pre-rift): Arrival of a hot mantle plume simulated by prescribing an excess temperature of 200 °C as bottom boundary condition and a fast divergent asthenospheric flow field. Velocity boundary conditions lead to small scale convection and a temperature increase in the asthenospheric mantle. (c) Phase III (syn-rift): Start of lithospheric extension with velocity boundary conditions prescribing a full extension velocity of 2 mm a^{-1} (Saria et al., 2014). Note how the mantle temperatures increased due to the previous plume arrival stage, while due to the low conductivity of rocks the shallow temperatures are not affected at all.*

4.4 Modeling Results

4.4.1 Evolution of the Numerical Reference Models

After the brief pre-plume phase, small-scale convection is observed in the asthenosphere during the pre-rift phase (Figure 2c). The lithosphere–asthenosphere boundary (LAB), which is defined here as the compositional interface between lithospheric and asthenospheric mantle, rose by up to 7 km in the model center due to the small-scale convection. At the end of the pre-rift phase, at a total modeled time of 21 million years, the temperature at the LAB has increased by ~100°C to 1350°C. Interestingly, temperatures in the shallower lithospheric mantle and the crustal layers are barely affected by this temperature increase (Figure 2c), since conductive equilibration in the lithosphere operates over hundreds of millions of years (Cacace & Scheck-Wenderoth, 2016). We also find that significantly longer plume-residence times do not heat the lithosphere enough to induce a shift from narrow to wide rifting. This could only be achieved by higher radiogenic heating or crustal thicknesses, which indicates that brittle localization has more control on resulting structures than conductive heating from below.

In the first 15 million years of the syn-rift phase, strain does not localize efficiently, and deformation is distributed throughout the entire crustal layer. As faults compete for strain, they successively coalesce until one of the border faults accommodates almost all extension (Figure 3). Meanwhile, the LAB rises by about 10 km and isotherms are advected upwards. At Moho depths, advection transfers heat faster than conduction, even at these slow extension rates. Finally, a narrow rift is established in the model center and the lithospheric layer is thinned further during continued extension. In our reference model for the Southern Kenya Rift, the narrow, asymmetric rift initiates at t_{10} = 10 Ma (Figure 3c). Timings are referenced to a state of the numerical model that compares well to the present-day rift (Figure 4). With ongoing deformation, the eastern border fault is established around 5 Ma (Figure 3d). Due to rotation of the major faults in the west, shallow, minor faults develop in the uppermost layer of the hanging-wall in the basin interior. A similar tectonic evolution is observed in our reference model for the Central Kenya rift (Figure 5). The main difference is that the secondary border fault is slightly more active. Hence, the difference in elevation of the rift shoulders is lower.

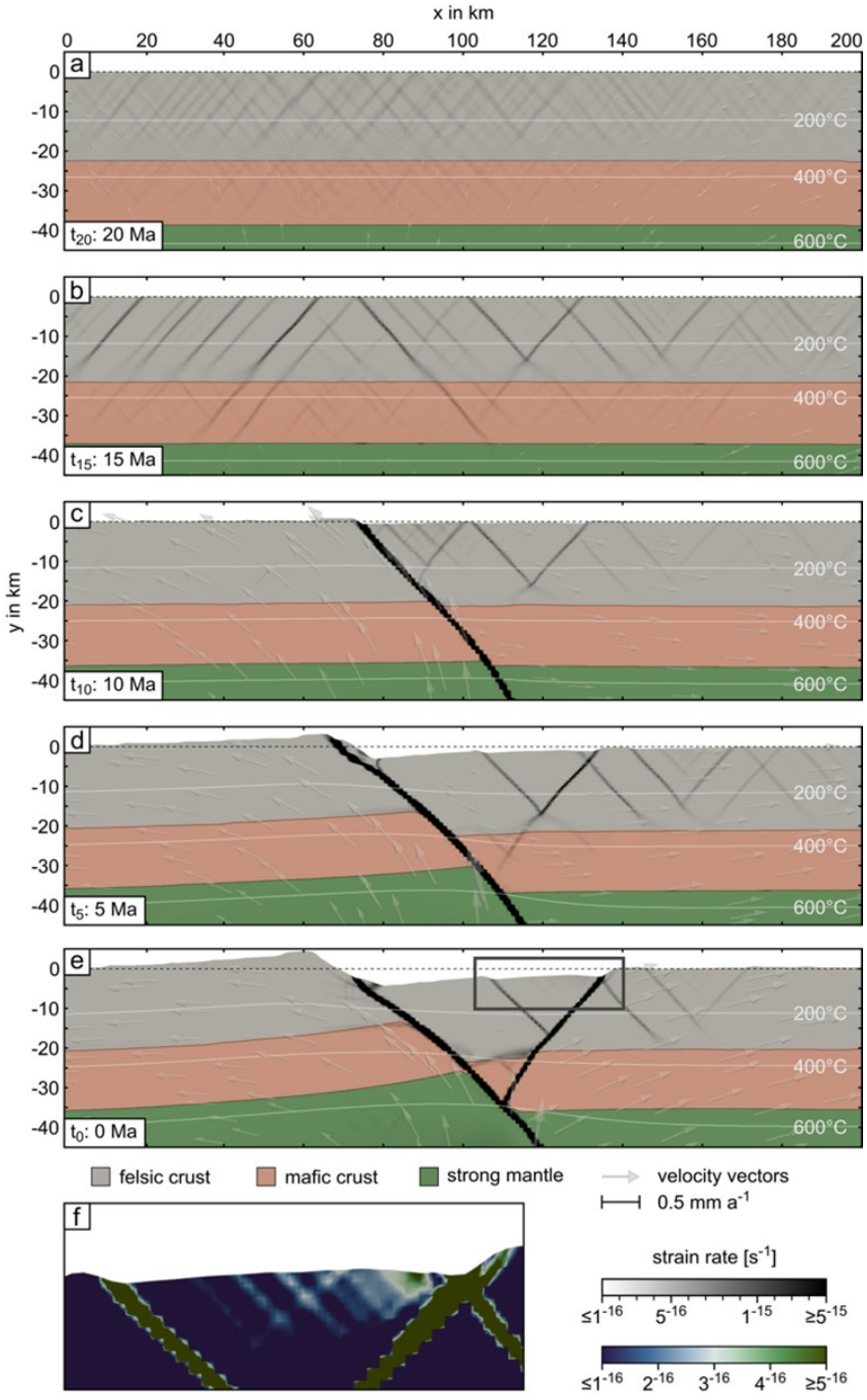

Figure 6. *Evolution of the reference model. (a) Syn-rift phase immediately after prescribing the extension velocity of 2 mma^{-1} at the boundaries. The strain rate pattern originates from the seeded strain and the implemented friction softening. Model time identical to* Figure *2c. (b) Localization of deformation slowly increases in the competing fault network before onset of rifting. (c) Asymmetric onset of rifting, initial uplift of the main rift shoulder at 10 Ma. (d) Border fault localisation at 5 Ma. (e) State of the rift that serves as our reference model for a comparison with the present-day Southern Kenya Rift. A westward dipping border fault has formed in the east, and shallow, crustal fault activity is observed in the eastern half of the graben. (f) Zoom of the upper crustal fault network.*

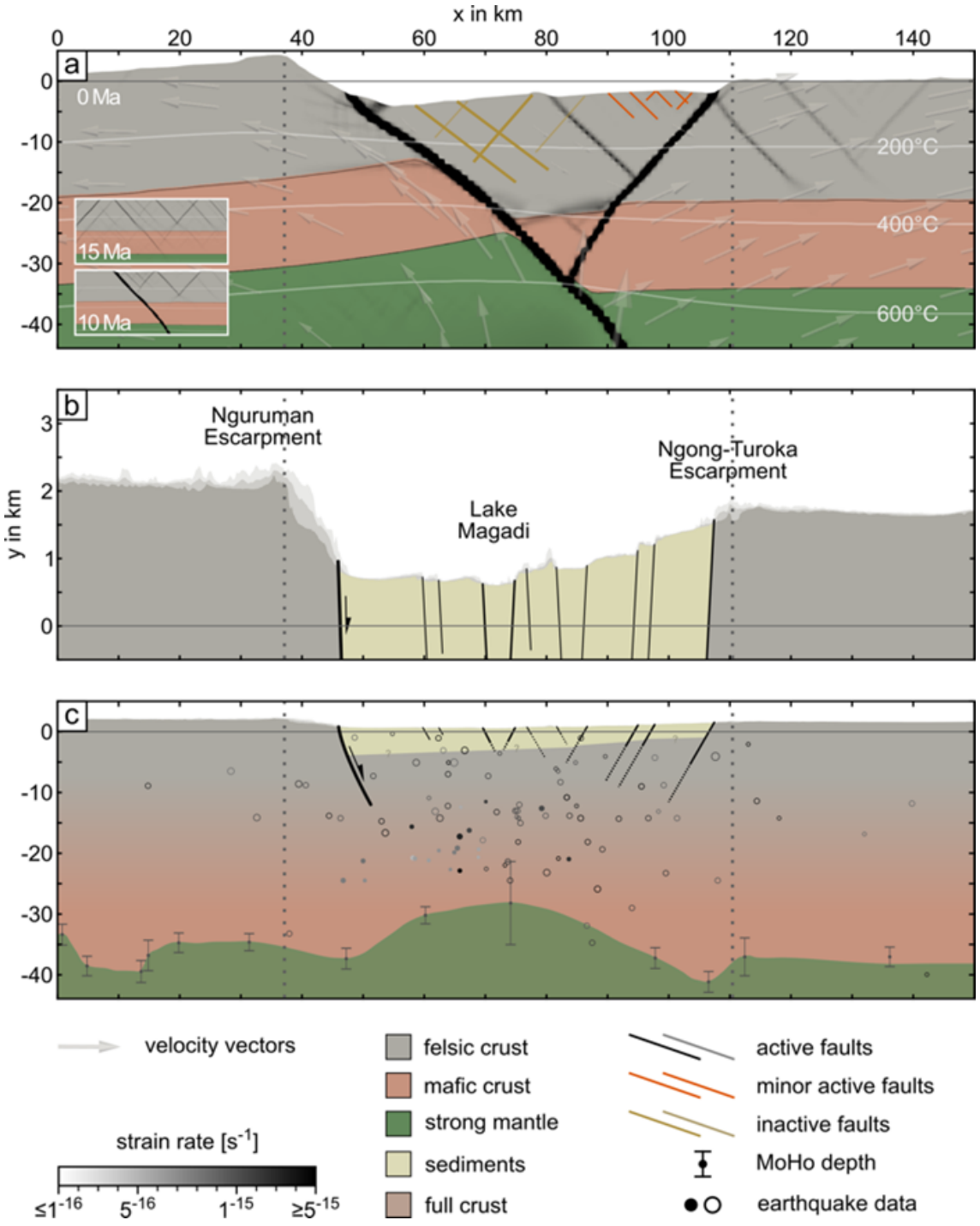

Figure 7. *Comparison of the numerical model and an observational cross section of the Southern Kenya Rift. (a) Snapshot of the numerical model with active (black and red) and inactive (dark yellow) faults. (b) Topographic swath across the Southern Kenya Rift, based on the TanDEM-X digital elevation model (10 times vertical exaggeration). Dark, medium and light gray indicate minimum, mean and maximum topography along 5 km wide swath; profile location indicated in Figure 1b. Mapped faults based on Baker (1958). (c) Cross section with earthquake data (filled circles: Weinstein et al., 2017; open circles: Hollnack & Stangl, 1998), Moho-depth measurements (small dots with error bars: Plasman et al., 2017) and estimated sediment thicknesses (yellow: Birt et al., 1997).*

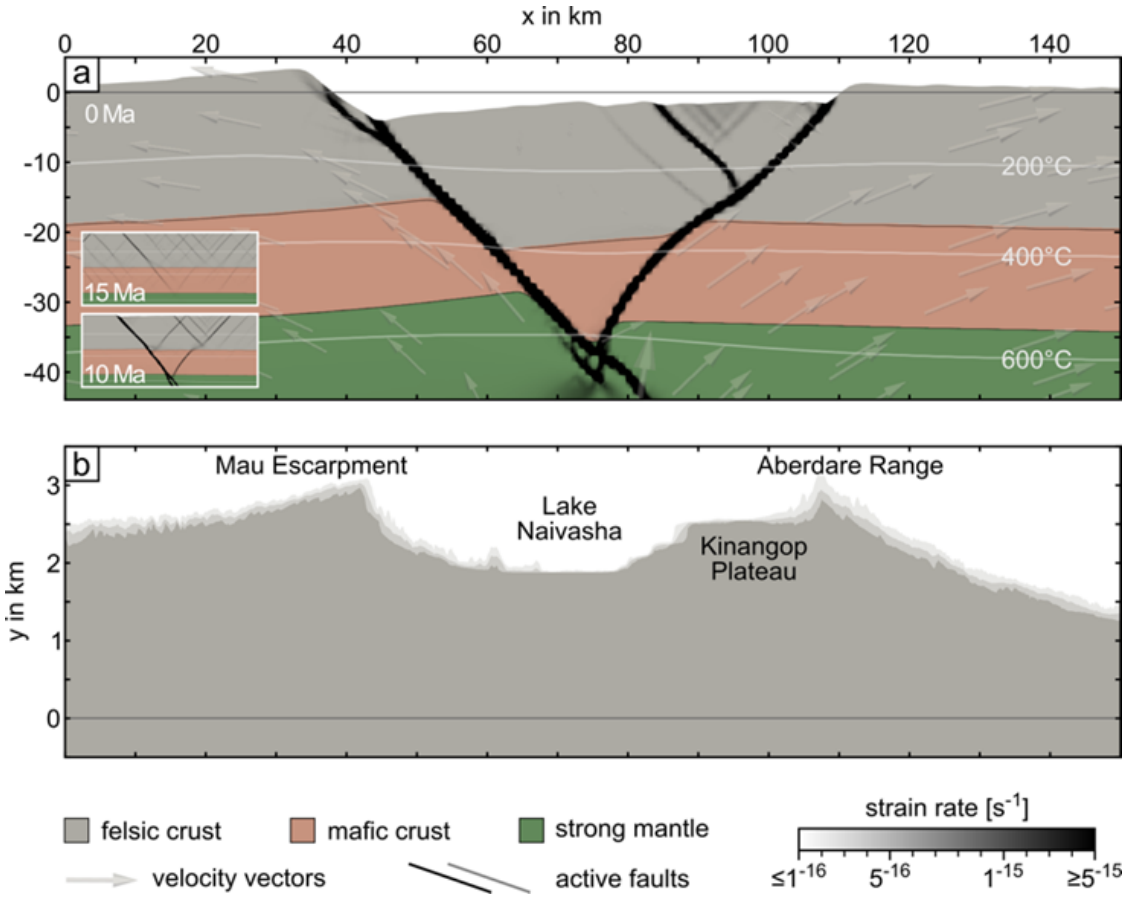

Figure 8. *Comparison of a numerical model with the same setup as the reference model, but different random noise, and a cross section of the Central Kenya Rift. (a) Snapshot of the numerical model results. (b) Topographic swath profile of the Central Kenya Rift, based on the TanDEM-X digital elevation model (10 times vertical exaggeration). Dark, medium and light gray indicate minimum, mean and maximum topography along 5-km-wide swath; profile location indicated in Figure 1b.*

4.4.2 Impact of inheritance

We investigate the impact of small-scale inheritance by introducing element-sized strength perturbation in our models. In nature, these heterogeneities may be represented by foliations, lithological heterogeneities or pore-pressure variations. Here, we approximate this complexity by means of randomly distributed strength variations that are implemented through the combination of frictional strain softening and an initial, random strain distribution. We conduct 26 model runs that are identical to the reference model except for a different random strain pattern at model start. Thereby, we self-consistently generate a range of possible crustal-scale fault configurations, but we also isolate the dominant deformation style of a specific numerical setup by monitoring its frequency across a range of initial noise configurations (Figure 6). Instead of comparing the models at the same modeled time, the results are compared after 10 million years of active rifting with the time of onset defined as the first occurrence of significant displacement along the main border fault(s). This way, the amount of deformation that is accommodated within the fault systems is more comparable. Note that the polarity of

asymmetric faulting is random, but for the ease of visual inspection and comparison we mirrored model figures if necessary, such that the main border fault dips to the right (Figure 6).

In this numerical setup, we find that about 50% of the models are strongly asymmetric with one main border fault active after 10 million years of active rifting (*one-sided*, e.g., Figure 6 M1–3). Flexural hanging-wall deformation is distributed over several secondary faults, with varying quantity and dip directions. We classify 40% of the models as *intermediate* such as our reference model (e.g., Figure 6 M4, MRef, M5). These models feature one dominant border fault, but secondary deformation in the hanging-wall is more pronounced than in the *one-sides* models. Only 10% of the models fall into the third, *two-sided* category (Figure 6 M6–M8), of which only one model (M6) features a symmetric border-fault geometry. All examples of this category feature a westward dipping border fault on the eastern rift side that reaches into the lithospheric mantle and limits the depth of the main fault in comparison to the more asymmetric models. Although models may be categorized at certain snapshots as in Figure 6, fault geometries actually develop over time. Strongly asymmetric models, for example, tend to become more symmetric due to coalescence of secondary faulting. In general, we find that the principal rift style (narrow) is unaffected by small-scale inheritance, but the tectonic history of each model may differ significantly. Deformation patterns are strongly influenced by the initial random noise distribution, especially in case of the hanging-wall segmentation and in the central area of normal fault blocks affecting the upper crust.

4.5 Discussion

Rifting in our models initiates across a distributed and complex network of low-deformation faults. Over time, the early developed fault network of individual faults coalesces into a system with a reduced number of faults that each accommodate larger displacements. This model evolution reproduces results of Cowie et al. (2005), who found that faults and shear zones that are characterized by a low maximum strain rate are active for a shorter time than faults with higher maximum strain rates. In agreement with our results, these authors explained the migration of fault activity into a narrower zone by a combination of crustal strain localization due to brittle failure and a co-evolving thermal structure. Our experimental results are in line with the observations from the Southern Kenya Rift, where after the formation of the first western border fault, hanging-wall flexure and a second phase of fault coalescence led to border-fault localization on the eastern rift side. The involved major crustal shear zones enable lithosphere-scale necking that strongly decreases the thickness of the lithosphere (Lavier & Manatschal, 2006).

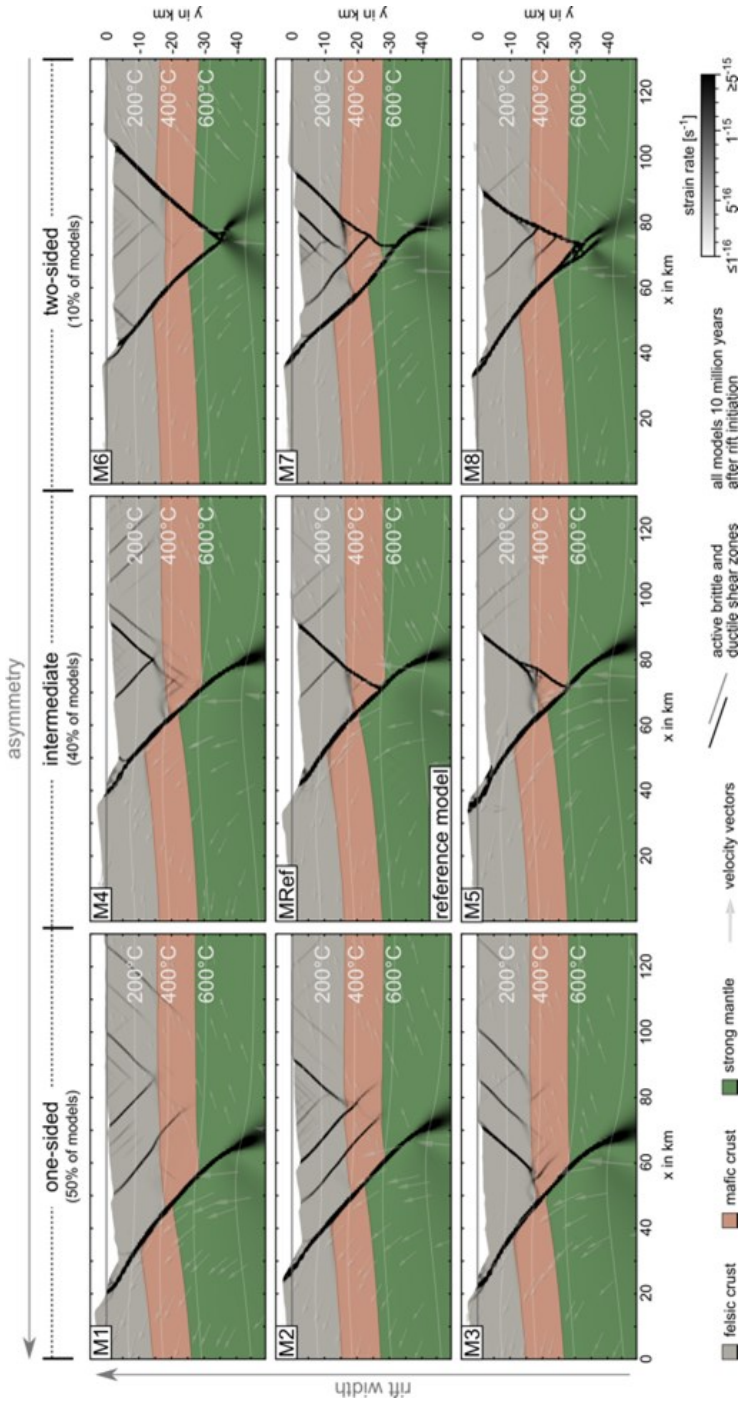

Figure 9. *Impact of different random noise patterns on rift style. The only difference in the setup of the models is the randomized initial strain distribution. Combined with strain-dependent friction and viscous softening, individual fault networks develop in each model. About half of the models are strongly asymmetric (one-sided) with a dominant main border fault and distributed hanging-wal deformation with varying fault-dip directions (M1–3). The second largest group (intermediate, ~40% of models) also features a main border fault, but deformation on the eastern rift border is more localized (M4, MRef, M5). Two-sided models (M6–M8) constitute the smallest group (~10%). While M7 and M8 still feature an asymmetric fault geometry, M6 has symmetric border faults with similar displacements. Models M6–M8 are different from the other two groups and both have a pronounced eastern border fault that extends into the lithospheric mantle and connects to the main fault at depth.*

Sustained and pronounced volcanic activity has been a major feature in all sectors of the Kenya Rift (Baker et al., 1971; Macdonald et al., 2001; Rooney, 2020; Williams, 1969b); however, we model rift evolution with a purely tectonic setup that does not account for diking or magmatic underplating. This apparent contradiction is nevertheless justified when considering first-order features: the existence of important border faults, the Nguruman, Mau or Sattima faults, clearly illustrates that a large part of the extension is accommodated by faulting. Intra-basin faults however, are likely affected by stress changes related to dike intrusion at depth (Behn et al., 2006; Rowland et al., 2007), providing a possible explanation for the second-order differences between our model and observations. Below we discuss these issues in more detail for the central and southern sectors of the Kenya Rift.

4.5.1 Southern Kenya Rift

First, we compare our numerical model to the available structural and stratigraphic data of the Southern Kenya Rift before we discuss the temporal evolution of the system in a second step. The first-order model geometry consisting of the main western border fault and a pronounced westward dipping fault in the east is in very good agreement with field and seismological observations (Figure 4). While the eastward-dipping border fault in our reference model features a high rift shoulder associated with a greater throw, the major fault on the eastern side of the rift valley records less displacement. From shoulder to shoulder, the rift is approximately 70 km wide, both in our experiment and in the Southern Kenya Rift. As in our model, a subdued area of high topography is observed in the basin center in nature and defined in both cases by a gentle westward-directed topographic gradient. In the model, the internal part of the eastern half of the rift is characterized by a shallow fault network in the top third of the upper crustal layer that may be responsible for producing the observed rift-parallel densely faulted rift center (Figure 3d). In nature, the thickness of the crystalline crust (i.e. excluding sedimentary cover) ranges between 25 and 30 km in the thinned rift center and up to 40 km in rift shoulder areas, and respective Moho depths range between 31 km and 43 km relative to sea level (Birt, 1996; Birt et al, 1997; Dugda et al., 2005; Ebinger et al., 2017; Green et al., 1991; Tugume et al., 2012; Sippel et al., 2017). These values agree very well with the crustal thicknesses of 25–30 km beneath the rift center and 40 km beneath the rift shoulders observed in the numerical model (see Figure 3e), particularly when considering that ~4–5 km of magmatic underplating can be expected in the Kenya rift (Thybo et al., 2000).

The evolution of the numerical model reproduces the asymmetric pattern of the overall rift evolution in southern Kenya. The first large-scale and unambiguous evidence for extensional tectonic activity is the formation of the eastward-dipping main border fault along the Nguruman Escarpment in South Kenya. The Nguruman fault is a major rift-bounding structure that is associated with an up to 40-m-wide cataclastic zone that follows the gneissic foliation in the basement rocks of the Mozambique Belt (Baker, 1958; Hetzel and Strecker, 1994). Stratigraphic relationships between Miocene nephelinites with an age range between approximately 15 and 9 Ma, the Nguruman fault scarp, and 6.9-m.y.-

old flood phonolites and trachytes that are banked against the fault scarp document that major faulting must have occurred here after 9 Ma and prior to 6.9 Ma (Baker, 1958; Baker and Mitchell, 1976; Crossley, 1979).

Conversely, on the eastern side of the rift our numerical model predicts a delay of 5 Ma (at t_5) in activity of the border-fault system due to the flexure of the central block (Figure 3d). This agrees with regional stratigraphic and structural relationships across the Ngong-Turoka escarpment on the eastern rift border, which also record a much later onset of the segmentation of a monocline that had formed in the ubiquitous Mio-Pliocene Trachytes (here, the 3.3-m.y.-old Nairobi Trachyte), which ultimately formed a pronounced set of escarpments that now define the eastern rift flank (Baker et al., 1988). In addition, our model predicts continued tectonic subsidence along the Nguruman Escarpment during the hanging-wall segmentation at the eastern rift border. These model results are supported by geological observations at the Nguruman Escarpment, where lateral pinchouts and direct contacts of Pliocene flood basalts (3.1–2.3 Ma) with faults at the Nguruman Escarpment (i.e. Kirikiti Basalts, Crossley; 1979) document protracted faulting and the generation of topographic conditions that prevented the spillover of these lavas on the western rift-shoulder areas. Thus, as predicted in the model, Pliocene tectonic activity at both sides of the Southern Kenya Rift ultimately generated a full-graben stage with two conjugate border faults where all tectonic and volcanic activity has been confined until the present day (t_{now} = 0 Ma; Figure 3e and 4).

The valley floor of the Southern Kenya Rift is dissected by a densely spaced, N-S-to-NNE-striking fault array (Baker, 1958; Ibs-von Seht et al., 2001; Weinstein et al., 2017). These faults are characterized by an average density of 1.6 surface faults per kilometer, each showing a throw of at least 35 m (e.g., Baker 1958). In general, it has been suggested that the spacing between adjacent normal faults is proportional to the thickness of the faulted layer (Dyksterhuis et al., 2007; Sharples et al., 2015). The dense fault spacing in the Southern Kenya Rift, however, cannot be related to the comparably thick brittle crust in this region (Albaric et al., 2009). In the model, the maximum depth of brittle faulting beneath the central basin is 5 km while the brittle-ductile transition is located at ~15 km depth (Figure 3f and 4a). These values correspond to earthquake-hypocenter depths and sectors of brittle deformation documented by an earthquake-recording network in the greater Lake Magadi region (Ibs-von-Seht et al., 2001). Our model results explain the predicted high fault density through hanging-wall bending, which leads to significantly closer-spaced fault arrays than expected from brittle layer thickness (Figure 3f). This can be understood when considering that hanging-wall flexure causes tensional stresses and normal faulting (Bott, 1996) above the neutral plane of bending, which is much shallower than the brittle-ductile transistion. Our model also shows that flexure takes place even after localization of the eastern border fault (Figure 3). This flexure of a hanging-wall block could explain the distributed intra-basin fault of the Magadi-Natron basin (Baker, 1958; Muirhead et al., 2016). An additional way to discriminate between normal faulting related to bending stresses in the hanging-wall block and regionally controlled extension

may be achieved by analyzing fault-length distributions, since bending-related normal faults tend to deviate from the commonly observed power-law distribution of pure-shear normal faults (e.g., Supak et al., 2006). In this context it is interesting that Muirhead et al. (2016) found that cumulative frequency plots of fault lengths within the Magadi-Natron basin are slightly more compatible with an exponential fit rather than a power-law fit, which suggests that the faults in the Magadi-Natron basin may reflect flexure-induced, shallow normal faulting. However, we caution that these densely-spaced normal faults could alternatively be related to locally elevated tensional stresses due to shallow dike emplacement (Behn et al., 2006; Muirhead et al., 2016; Rowland et al., 2007), a process that we cannot reproduce with our current modeling capabilities. While a certain fraction of normal faults in the Kenya Rift may be associated with dike emplacement (e.g., Ibs-van-Seht et al., 2001; Tongue et al., 1992), we speculate that such a process should have a greater impact in more advanced regions of extension, such as Afar, where the magmatic input is significantly larger than in our study region (Kendall et al., 2005; Stab et al., 2015; Wright et al., 2006).

The spatial distribution of extension within the Southern Kenya Rift has been recently quantified by means of analyzing fault systems, GPS-based motion vectors, and the chronology of lava-flow emplacement (Muirhead et al., 2016). The authors infer that 0.4–0.6 mm a^{-1} are accommodated by slip along the Nguruman border fault on the western rift side while 1.34~1.60 mm a^{-1} are taken up by the intra-rift faults. Our reference model for the Southern Kenya Rift exibits 1.0 mm a^{-1} for the western border fault, 0.44 mm a^{-1} across the eastern border fault and 0.1 mm a^{-1} for intra-basin faults. The remaining 0.46 mm a^{-1} are accommodated by deformation outside the rift, mostly along faults east of the eastern border faults. In particular, deformation in the modeled rift center does not match the extension values across the small-scale intra-rift fault network of Muirhead et al. (2016). We speculate that this might be due to insufficient numerical representation of magmatic weakening processes acting in the rift. These processes include (1) thermal weakening of the crust due to magmatic addition (Thybo et al., 2000), (2) dike injections that drive extension (Buck, 2006, Oliva et al., 2019) and near-surface faulting (Behn et al., 2006), and (3) fluid flow along rift-internal faults (Muirhead et al., 2016), which reduces the effective friction on faults. By forcing deformation to the rift center, these weakening processes would ultimately reduce activity of the border faults. Future comparative modeling studies should therefore set out to consider magmatic processes associated with diking and fluid migration in order to investigate their role in localization processes within young continental rift settings at lithospheric-scale.

4.5.2 Central Kenya Rift

Our model predicts asymmetric rift initiation with an east-dipping normal fault along the future western side of the rift. This is supported by the geological observations and the distribution of regionally extensive Middle Miocene Plateau Phonolite flows emplaced prior to the onset of faulting on the western side of the rift (Baker et al., 1971; 1988; Strecker et al., 1990). The numerical model chosen for comparison with the Central

Kenya Rift (Figure 5a) is similar to the reference model of the Southern Kenya Rift (Section 4.2), but it differs in the displacement along the secondary (eastern) border fault that develops ~5 Ma after rift initiation a difference that is solely caused by an alternative random noise pattern in initial strain. This is compares very well with geological interpretations where spatially more restricted emplacement of lava flows within the developing rift basin and the overspilling of flows toward the east in the area of the present-day rift shoulders support the notion of an initial halfgraben, followed by segmentation of the hanging-wall block between 5.5 and 4 Ma (Baker et al., 1988; Clarke et al., 1990; Shackleton, 1945).

Further similarities exist between our Central Kenya Rift Model (Figure 5a) and interpretations drawn from stratigraphic relationships and faulting on the western side of the central segment, where our model predicts a 4-km-offset of the crystalline basement surface. This can also be inferred from field-based observations and data from geothermal drilling in the Naivasha area (Clarke et al., 1990; Strecker, 1991) indicating that the throw involving the Mio-Pliocene Plateau Trachytes is on the order of 2 km since ~3 Ma. In addition, the total offset of the basement rocks based on exposures on the western rift shoulder and their depth position obtained from seismic refraction data (KRISP working group, 1987) is approximately 4 km (Strecker, 1991). However, the formation of the Kinangop Plateau (Figure 5), limited by the westward-dipping Sattima fault in the east and the westward-dipping Kinangop fault to the west, is not represented in the numerical model. Instead, a synthetic normal fault has developed in our model that segments the hanging-wall block.

4.5.3 Influence of inheritance and crustal anisotropies

Our analysis shows that the initial fault pattern may strongly control the first-order structure of a rift. In some cases, the initial fault configuration may even override the rheologically expected symmetry (Huismans et al., 2005) and induce a symmetric rift in a setup that otherwise generates predominantly asymmetric geometries (Figure 6). This means that any process affecting the initial fault configuration, such as rupture propagation along structures inherited from earlier deformation phases (Muirhead & Kattenhorn, 2018), strain softening (Huismans & Beaumont, 2003) or initial diking (Buck, 2006) may affect the first-order structural evolution of a rift and possibly of the future rifted margin.

In the lithosphere below the Kenya Rift, the Late Proterozoic Mozambique Belt is a known major crustal heterogeneity that once constituted a collisional orogen in the suture zone between East and West Gondwana, (Smith & Mosley, 1993) and it is hypothesized to have influenced the geometry of the Kenya Rift during all stages of its evolution (e.g., Hetzel and Strecker, 1994; Muirhead & Kattenhorn, 2018; Robertson et al. 2015; Shackleton, 1976; Shackleton & Ries, 1984; Smith, 1994; Smith & Mosley 1993). Our model sheds new light on the influence of such crustal heterogeneities: while most numerical models change rheological setup and strain softening parameters (e.g.

Armitage et al., 2018; Brune et al., 2017b; Duclaux et al., 2020; Ros et al., 2017), we varied the initial random strain pattern and kept rheology and strain softening the same. By using this approach, we are able to show that low-degree variability of crustal strength may decisively influence rift geometry. While predominantly asymmetric rift configurations can be generated in this way, in some cases, variability in crustal strength may even lead to symmetric rift patterns in a cold and brittle lithosphere (Figure 6).

4.6 Conclusions

In this study, we employed a 2D numerical model to integrate geological and geophysical data into a framework that enables us to explain the tectonically characteristic evolution of the Southern and Central Kenya Rift. This encompasses the following processes and steps: (1) a broad zone of low deformation and competing faults develops until coalescence of faults takes place and a single border fault localizes. before (2) a conjugate border fault develops and (3) an anomalously shallow fault network emerges due to bending of the central hanging-wall block. Even though volcanic activity is ubiquitous in the Kenya Rift, our purely tectonic model is capable of reproducing first-order characteristics of the rift. By utilizing a random noise implementation of initial strain, we highlight that the 2D setup is capable of addressing along-strike variations of the rift, but also that small-scale crustal inheritance strongly affects first-order faults and overall rift geometry.

Data Availability Statement

All data that this numerical study is based on can be found in Table 1 and Figure 2 and is referenced in corresponding captions. Figures were created using Paraview and Matlab and color maps were taken from Crameri (2018). Elevation data shown in Figures 1, 4 and 5 is based on the TanDEM-X science DEM, granted by the German Space Agency (© DLR 2017).

Acknowledgments

This study was conducted within the Helmholtz Young Investigators Group CRYSTALS (VH-NG-1132). We thank the Computational Infrastructure for Geodynamics (geodynamics.org) which is funded by the National Science Foundation under award EAR-0949446 and EAR-1550901 for supporting the development of ASPECT. MR and SR acknowledge field support by R. Potts, Smithsonian Institution, Washington DC and Geothermal Development Company, Kenya, and discussions with L. Olaka, University of Nairobi. The work was supported by the North-German Supercomputing Alliance (HLRN). We thank reviewers James Muirhead, Jolante van Wijk, and Anthony Jourdon as well as Associate Editor Luc Lavier for detailed and very constructive comments that significantly helped to improve this manuscript. Open access funding enabled and organized by Projekt DEAL.

References

Albaric, J., Déverchère, J., Petit, C., Perrot, J., & Le Gall, B. (2009). Crustal rheology and depth distribution of earthquakes: Insights from the central and southern East African Rift System. *Tectonophysics*, *468*(1–4), 28–41.

Armitage, J. J., Petersen, K. D., & Pérez-Gussinyé, M. (2018). The Role of Crustal Strength in Controlling Magmatism and Melt Chemistry During Rifting and Breakup. *Geochemistry, Geophysics, Geosystems*, *19*(2), 534–550. https://doi.org/10.1002/2017GC007326

Atmaoui, N., & Hollnack, D. (2003). Neotectonics and extension direction of the Southern Kenya Rift, Lake Magadi area. *Tectonophysics*, *364*(1–2), 71–83. https://doi.org/10.1016/S0040-1951(03)00051-9

Baker, B. H. (1958). Geology of the Magadi area, degree sheet 51, SW Quarter (No. 42), Geological Survey of Kenya Report. *Geological Survey of Kenya*.

Baker, B. H., & Mitchell, J. G. (1976). Volcanic stratigraphy and geochronology of the Kedong–Olorgesailie area and the evolution of the South Kenya rift valley. *Journal of the Geological Society, 132*(5), 467–484. https://doi.org/10.1144/gsjgs.132.5.0467

Baker, B. H., Mitchell, J. G., & Williams, L. A. J. (1988). Stratigraphy, geochronology and volcano-tectonic evolution of the Kedong-Naivasha-Kinangop region, Gregory Rift Valley, Kenya. *Journal of Geological Society*, *145*(1), 107–116. https://doi.org/10.1144/gsjgs.145.1.0107

Baker, B. H., Williams, L. A. J., Miller, J. A., & Fitch, F. J. (1971). Sequence and geochronology of the Kenya rift volcanics. *Tectonophysics*, *11*(3), 191–215. https://doi.org/10.1016/0040-1951(71)90030-8

Bangerth, W., Austermann, J., Bürg, M., Cox, S., Durkin, W., Euen, G., … Zhang, S. (2019). ASPECT: Advanced Solver for Problems in Earth's ConvecTion, User Manual. *Figshare.* https://doi.org/10.6084/m9.figshare.4865333

Bangerth, W., Dannberg, J., Gassmoeller, R., & Heister, T. (2018). Aspect V2.0.1. *Zenodo*. https://doi.org/10.5281/zenodo.1297145

Bassi, G. (1991). Factors controlling the style of continental rifting: insights from numerical modelling. *Earth and Planetary Science Letters*, *105*(4), 430–452. https://doi.org/10.1016/0012-821X(91)90183-I

Bastow, I. D., & Keir, D. (2011). The protracted development of the continent-ocean transition in Afar. *Nature Geoscience*, *4*(4), 248–250. https://doi.org/10.1038/ngeo1095

Behn, M. D., Buck, W. R., & Sacks, I. S. (2006). Topographic controls on dike injection in volcanic rift zones. *Earth and Planetary Science Letters, 246*(3), 188–196. https://doi.org/10.1016/j.epsl.2006.04.005

Beniest, A., Koptev, A., & Burov, E. (2017). Numerical models for continental break-up: Implications for the South Atlantic. *Earth and Planetary Science Letters*, *461*, 176–189. https://doi.org/10.1016/j.epsl.2016.12.034

Beutel, E., van Wijk, J., Ebinger, C., Keir, D., & Agostini, A. (2010). Formation and stability of magmatic segments in the Main Ethiopian and Afar rifts. *Earth and Planetary Science Letters, 293*(3–4), 225–235. https://doi.org/10.1016/j.epsl.2010.02.006

Birt, C. S. (1996). *Geophysical investigation of active continental rifting in southern Kenya* (Doctoral dissertation). University of Leicester. https://hdl.handle.net/2381/34979

Birt, C. S., Maguire, P. K. H., Khan, M. A., Thybo, H., Keller, G. R., & Patel, J. (1997). The influence of pre-existing structures on the evolution of the southern Kenya Rift Valley—

evidence from seismic and gravity studies. *Tectonophysics, 278*(1-4), 211-242. https://doi.org/10.1016/S0040-1951(97)00105-4

Bott, M. H. P. (1996). Flexure associated with planar faulting. *Geophysical Journal International, 126*(3), F21–F24. https://doi.org/10.1111/j.1365-246X.1996.tb04692.x

Brun, J. P. (1999). Narrow rifts versus wide rifts: inferences for the mechanics of rifting from laboratory experiments. *Philosophical Transactions of the Royal Society of London. Series A: Mathematical, Physical and Engineering Sciences*, *357*(1753), 695–712. https://doi.org/10.1098/rsta.1999.0349

Brune, S. (2014). Evolution of stress and fault patterns in oblique rift systems: 3-D numerical lithospheric-scale experiments from rift to breakup. *Geochemistry, Geophysics, Geosystems*, *15*(8), 3392–3415. https://doi.org/10.1002/2014GC005446

Brune, S., Heine, C., Perez-Gussinye, M., & Sobolev, S. V. (2014). Rift migration explains continental margin asymmetry and crustal hyper-extension. *Nature Communications*, *5*(4014). https://doi.org/10.1038/ncomms5014

Brune, S., Corti, G., & Ranalli, G. (2017a). Controls of inherited lithospheric heterogeneity on rift linkage: Numerical and analog models of interaction between the Kenyan and Ethiopian rifts across the Turkana depression. *Tectonics*, *36*(9), 2017TC004739. https://doi.org/10.1002/2017TC004739

Brune, S., Heine, C., Clift, P. D., & Pérez-Gussinyé, M. (2017b). Rifted margin architecture and crustal rheology: Reviewing Iberia-Newfoundland, Central South Atlantic, and South China Sea. *Marine and Petroleum Geology*, *79*, 257–281. https://doi.org/10.1016/j.marpetgeo.2016.10.018

Buck, W. R., Lavier, L. L., & Poliakov, A. N. B. (1999). How to make a rift wide. *Philosophical Transactions of the Royal Society of London. Series A: Mathematical, Physical and Engineering Sciences*, *357*(1753), 671–693. https://doi.org/10.1098/rsta.1999.0348

Buck, W. R., Lavier, L. L., & Poliakov, A. N. (2005). Modes of faulting at mid-ocean ridges. *Nature*, 434(7034), 719-723. https://doi.org/10.1038/nature03358

Buck, W. R. (2006). The role of magma in the development of the Afro-Arabian Rift System. *Geological Society, London, Special Publications*, *259*(1), 43–54. https://doi.org/10.1144/GSL.SP.2006.259.01.05

Buiter, S. J. H., Huismans, R. S., & Beaumont, C. (2008). Dissipation analysis as a guide to mode selection during crustal extension and implications for the styles of sedimentary basins. *Journal of Geophysical Research-Solid Earth*, *113*(B6). https://doi.org/doi:10.1029/2007JB005272

Bunge, H.-P. (2005). Low plume excess temperature and high core heat flux inferred from non-adiabatic geotherms in internally heated mantle circulation models. *Physics of the Earth and Planetary Interiors*, *153*(1–3), 3–10. https://doi.org/10.1016/j.pepi.2005.03.017

Burov, E. B., & Schubert, G. (2007). Plate Rheology and Mechanics. In *Treatise on Geophysics Vol 6-Crust and Lithosphere Dynamics* (pp. 99–151).

Cacace, M., & Scheck-Wenderoth, M. (2016). Why intracontinental basins subside longer: 3-D feedback effects of lithospheric cooling and sedimentation on the flexural strength of the lithosphere. *Journal of Geophysical Research: Solid Earth*, *121*(5), 3742–3761. https://doi.org/10.1002/2015JB012682

Calais, E., D'Oreye, N., Albaric, J., Deschamps, A., Delvaux, D., Déverchère, J., … Wauthier, C. (2008). Strain accommodation by slow slip and dyking in a youthful continental rift, East Africa. *Nature*, *456*(7223), 783–787. https://doi.org/10.1038/nature07478

Celli, N. L., Lebedev, S., Schaeffer, A. J., & Gaina, C. (2020). African cratonic lithosphere carved by mantle plumes. *Nature Communications*, *11*(1), 92. https://doi.org/10.1038/s41467-019-13871-2

Chapman, G. R., & Brook, M. (1978). Chronostratigraphy of the Baringo Basin, Kenya. *Geological Society Special Publication*, *6*, 207–223. https://doi.org/10.1144/GSL.SP.1978.006.01.16

Civiero, C., Armitage, J. J., Goes, S., & Hammond, J. O. S. (2019). The Seismic Signature of Upper-Mantle Plumes: Application to the Northern East African Rift. *Geochemistry, Geophysics, Geosystems*, *20*(12), 6106–6122. https://doi.org/10.1029/2019GC008636

Civiero, C., Hammond, J. O. S., Goes, S., Fishwick, S., Ahmed, A., Ayele, A., et al. (2015). Multiple mantle upwellings in the transition zone beneath the northern East-African Rift system from relative P-wave travel-time tomography. *Geochemistry, Geophysics, Geosystems*, *16*(9), 2949–2968. https://doi.org/10.1002/2015GC005948

Clarke, M. C. G., Woodhall, D. G., Allen, D., & Darling, G. (1990). *Geological, volcanological and hydrological controls on the occurrence of geothermal activity in the area surrounding Lake Naivasha, Kenya*. Kenya, Ministry of Energy Report, Nairobi, Kenya.

Corti, G. (2009). Continental rift evolution: From rift initiation to incipient break-up in the Main Ethiopian Rift, East Africa. *Earth-Science Reviews*, *96*(1–2), 1–53. https://doi.org/10.1016/j.earscirev.2009.06.005

Corti, G. (2012). Evolution and characteristics of continental rifting: Analog modeling-inspired view and comparison with examples from the East African Rift System. *Tectonophysics*, *522–523*, 1–33. https://doi.org/10.1016/j.tecto.2011.06.010

Corti, G., Cioni, R., Franceschini, Z., Sani, F., Scaillet, S., Molin, P., et al. (2019). Aborted propagation of the Ethiopian rift caused by linkage with the Kenyan rift. *Nature Communications*, *10*(1), 1309. https://doi.org/10.1038/s41467-019-09335-2

Corti, G., van Wijk, J., Bonini, M., Sokoutis, D., Cloetingh, S., Innocenti, F., & Manetti, P. (2003). Transition from continental break-up to punctiform seafloor spreading: How fast, symmetric and magmatic. *Geophysical Research Letters, 30*(12), 1604. https://doi.org/10.1029/2003GL017374

Corti, G., van Wijk, J., Cloetingh, S., & Morley, C. K. (2007). Tectonic inheritance and continental rift architecture: Numerical and analogue models of the East African Rift system. *Tectonics, 26*(6). https://doi.org/10.1029/2006TC002086

Cowie, P. A., Underhill, J. R., Behn, M. D., Lin, J., & Gill, C. E. (2005). Spatio-temporal evolution of strain accumulation derived from multi-scale observations of Late Jurassic rifting in the northern North Sea: A critical test of models for lithospheric extension. *Earth and Planetary Science Letters*, *234*(3–4), 401–419. https://doi.org/10.1016/j.epsl.2005.01.039

Crameri, F. (2018). Geodynamic diagnostics, scientific visualisation and StagLab 3.0. *Geoscientific Model Development Discussions*, (February), 1–41. https://doi.org/10.5194/gmd-2017-328

Crossley, R. (1979). The Cenozoic stratigraphy and structure of the western part of the Rift Valley in southern Kenya. *Journal of the Geological Society*, *136*(4), 393–405. https://doi.org/10.1144/gsjgs.136.4.0393

Delvaux, D., Kervyn, F., Macheyeki, A. S., & Temu, E. B. (2012). Geodynamic significance of the TRM segment in the East African Rift (W-Tanzania): Active tectonics and paleostress in the Ufipa plateau and Rukwa basin. *Journal of Structural Geology*, *37*, 161–180. https://doi.org/10.1016/j.jsg.2012.01.008

Döhmann, M. J. E. A., Brune, S., Nardini, L., Rybacki, E., & Dresen, G. (2019). Strain Localization and Weakening Processes in Viscously Deforming Rocks: Numerical Modeling Based on Laboratory Torsion Experiments. *Journal of Geophysical Research: Solid Earth*, *124*(1), 1120–1137. https://doi.org/10.1029/2018JB016917

Duclaux, G., Huismans, R. S., & May, D. A. (2020). Rotation, narrowing, and preferential reactivation of brittle structures during oblique rifting. *Earth and Planetary Science Letters*, *531*, 115952. https://doi.org/10.1016/j.epsl.2019.115952

Dugda, M. T., Nyblade, A. A., Julia, J., Langston, C. A., Ammon, C. J., & Simiyu, S. (2005). Crustal structure in Ethiopia and Kenya from receiver function analysis: Implications for rift development in eastern Africa. *Journal of Geophysical Research: Solid Earth*, *110*(B1). https://doi.org/10.1029/2004JB003065

Duretz, T., Petri, B., Mohn, G., Schmalholz, S. M., Schenker, F. L., & Müntener, O. (2016). The importance of structural softening for the evolution and architecture of passive margins. *Scientific Reports*, *6*, 38704.

Dyksterhuis, S., Rey, P., Müller, R. D., Moresi, L., Ebinger, C., & Scholz, C. A. (2007). Effects of initial weakness on rift architecture continental rift basins: The East African perspective. *Geological Society, London, Special Publications, Tectonics of sedimentary basins: Recent advances*, *282*(1), 443–455. https://doi.org/10.1002/9781444347166.ch9

Ebinger, C., & Scholz, C. A. (2011). Continental rift basins: the East African perspective. *Tectonics of sedimentary basins: Recent advances*, 183-208. https://doi.org/10.1002/9781444347166.ch9

Ebinger, C. J., Keir, D., Bastow, I. D., Whaler, K., Hammond, J. O. S., Ayele, A., et al. (2017). Crustal Structure of Active Deformation Zones in Africa: Implications for Global Crustal Processes. *Tectonics*, *36*(12), 3298–3332. https://doi.org/10.1002/2017TC004526

Ego, J. K. (1994), Sedimentology and diagenesis of Neogene sediments in the Central Kenya Rift Valley, MSc thesis, Univ. of Saskatchewan, Saskatoon, 1–148. http://hdl.handle.net/10388/etd-01082010-110639

Faccenna, C., Glišović, P., Forte, A., Becker, T. W., Garzanti, E., Sembroni, A., & Gvirtzman, Z. (2019). Role of dynamic topography in sustaining the Nile River over 30 million years. *Nature Geoscience*, *12*(12), 1012–1017. https://doi.org/10.1038/s41561-019-0472-x

Gassmöller, R., Lokavarapu, H., Heien, E., Puckett, E. G., & Bangerth, W. (2018). Flexible and Scalable Particle-in-Cell Methods With Adaptive Mesh Refinement for Geodynamic Computations. *Geochemistry, Geophysics, Geosystems*, *19*(9), 3596–3604. https://doi.org/10.1029/2018GC007508

Gawthorpe, R. L., & Leeder, M. R. (2008). Tectono-sedimentary evolution of active extensional basins. *Basin Research*, *12*(3-4), 195-218. https://doi.org/10.1111/j.1365-2117.2000.00121.x

Geological map of Kenya, with structural contours. Nairobi: Ministry of Energy and Regional Development of Kenya.

Gerbi, C., Culshaw, N., & Marsh, J. (2010). Magnitude of weakening during crustal-scale shear zone development. *Journal of Structural Geology, 32*(1), 107–117. https://doi.org/10.1016/j.jsg.2009.10.002

Glerum, A., Thieulot, C., Fraters, M., Blom, C., & Spakman, W. (2018). Nonlinear viscoplasticity in ASPECT: benchmarking and applications to subduction. *Solid Earth*, *9*(2), 267–294. https://doi.org/10.5194/se-9-267-2018

Glerum, A., Brune, S., Stamps, D. S., & Strecker, M. R. (2020). Victoria continental microplate dynamics controlled by the lithospheric strength distribution of the East African Rift. *Nature Communications*, 11(1), 2881. https://doi.org/10.1038/s41467-020-16176-x

Green, W. V., Achauer, U., & Meyer, R. P. (1991). A three-dimensional seismic image of the crust and upper mantle beneath the Kenya rift. *Nature*, *354*(6350), 199–203. https://doi.org/10.1038/354199a0

Guth, A. (2014). Maps of the Southern Kenya Rift. Geological Society of America. https://doi.org/10.1130/2014.DMCH016

Hackman, B. D. (1988). Geology of the Baringo-Laikipia area, Republic of Kenya. *Ministry of Environmental and Natural Resources, Geology and Mines Department, Rep. 104.*

Halldórsson, S. A., Hilton, D. R., Scarsi, P., Abebe, T., & Hopp, J. (2014). A common mantle plume source beneath the entire East African Rift System revealed by coupled helium-neon systematics. *Geophysical Research Letters*, *41*(7), 2304–2311. https://doi.org/10.1002/2014GL059424

Hautot, S., Tarits, P., Whaler, K., Le Gall, B., Tiercelin, J. J., & Le Turdu, C. (2000). Deep structure of the Baringo Rift Basin (central Kenya) from three-dimensional magnetotelluric imaging: Implications for rift evolution. *Journal of Geophysical Research: Solid Earth, 105*(B10), 23493-23518. https://doi.org/10.1029/2000JB900213

Heckenbach, E. L., Brune, S., Glerum, A. C., & Bott, J. (2021). Is There a Speed Limit for the Thermal Steady-State Assumption in Continental Rifts? *Geochemistry, Geophysics, Geosystems*, *22*(3), e2020GC009577. https://doi.org/10.1029/2020GC009577

Heister, T., Dannberg, J., Gassmöller, R., & Bangerth, W. (2017). High accuracy mantle convection simulation through modern numerical methods - II: Realistic models and problems. *Geophysical Journal International*, *210*(2), 833–851. https://doi.org/10.1093/gji/ggx195

Hetzel, R., & Strecker, M. R. (1994). Late Mozambique Belt structures in western Kenya and their influence on the evolution of the Cenozoic Kenya Rift. *Journal of Structural Geology, 16*(2), 189–201.

Hillaire-Marcel, C., Carro, O., & Casanova, J. (1986). 14 C and Th/U Dating of Pleistocene and Holocene Stromatolites from East African Paleolakes. *Quaternary Research*, *25*(3), 312–239. https://doi.org/10.1016/0033-5894(86)90004-9

Hirth, G., & Kohlstedt, D. L. (2003). Rheology of the Upper Mantle and the Mantle Wedge : A View from the Experimentalists upper mantle . We first analyze experimental data to provide a critical review of flow. *Geophysical Monograph Series*, *138*, 83–105. https://doi.org/10.1029/138GM06

Hodge, M., Fagereng, Å., Biggs, J., & Mdala, H. (2018). Controls on Early-Rift Geometry: New Perspectives From the Bilila-Mtakataka Fault, Malawi. *Geophysical Research Letters*, *45*(9), 3896–3905. https://doi.org/10.1029/2018GL077343

Hofmann, C., Courtillot, V., Féraud, G., Rochette, P., Yirgu, G., Ketefo, E., & Pik, R. (1997). Timing of the Ethiopian flood basalt event and implications for plume birth and global change. *Nature*, *389*(6653), 838–841. https://doi.org/10.1038/39853

Hollnack, D., & Stangl, R. (1998). The seismicity related to the southern part of the Kenya Rift. *Journal of African Earth Sciences*, *26*(3), 477–495. https://doi.org/10.1016/S0899-5362(98)00027-X

Huismans, R. S., & Beaumont, C. (2003). Symmetric and asymmetric lithospheric extension: Relative effects of frictional-plastic and viscous strain softening. *Journal of Geophysical Research: Solid Earth*, *108*(B10). https://doi.org/10.1029/2002JB002026

Huismans, R. S., Buiter, S. J. H., & Beaumont, C. (2005). Effect of plastic-viscous layering and strain softening on mode selection during lithospheric extension. *Journal of Geophysical Research-Solid Earth*, *110*(B2). https://doi.org/10.1029/2004JB003114

Huismans, R. S., & Beaumont, C. (2011). Depth-dependent extension, two-stage breakup and cratonic underplating at rifted margins. *Nature*, *473*(7345), 74–78. https://doi.org/10.1038/nature09988

Ibs-von Seht, M., Blumenstein, S., Wagner, R., Hollnack, D., & Wohlenberg, J. (2001). Seismicity, seismotectonics and crustal structure of the southern Kenya Rift-new data from the Lake Magadi area. *Geophysical Journal International*, *146*(2), 439–453. https://doi.org/10.1046/j.0956-540x.2001.01464.x

Jammes, S., & Lavier, L. L. (2019). Effect of contrasting strength from inherited crustal fabrics on the development of rifting margins. *Geosphere*. https://doi.org/10.1130/GES01686.1

Jaupart, C., Mareschal, J.-C., & Iarotsky, L. (2016). Radiogenic heat production in the continental crust. *Lithos*, *262*, 398–427. https://doi.org/10.1016/j.lithos.2016.07.017

Jeanniot, L., & Buiter, S. J. H. (2018). A quantitative analysis of transtensional margin width. *Earth and Planetary Science Letters*, *491*, 95–108. https://doi.org/10.1016/j.epsl.2018.03.003

Jourdon, A., Kergaravat, C., Duclaux, G., & Huguen, C. (2021). Looking beyond kinematics: 3D thermo-mechanical modelling reveals the dynamic of transform margins. *Solid Earth Discussions*, 1–34. https://doi.org/10.5194/se-2021-18

Katumwehe, A. B., Abdelsalam, M. G., & Atekwana, E. A. (2015). The role of pre-existing Precambrian structures in rift evolution: The Albertine and Rhino grabens, Uganda. *Tectonophysics*, *646*, 117–129. https://doi.org/10.1016/j.tecto.2015.01.022

Kendall, J.-M., & Lithgow-Bertelloni, C. (2016). Why is Africa rifting? *Geological Society, London, Special Publications*, *420*(1), 11–30. https://doi.org/10.1144/SP420.17

Kendall, J.-M., Stuart, G. W., Ebinger, C. J., Bastow, I. D., & Keir, D. (2005). Magma-assisted rifting in Ethiopia. *Nature*, *433*(7022), 146–148. https://doi.org/10.1038/nature03161

Khalil, H. M., Capitanio, F. A., Betts, P. G., & Cruden, A. R. (2020). 3-D Analog Modeling Constraints on Rifting in the Afar Region. *Tectonics*, *39*(10), e2020TC006339. https://doi.org/10.1029/2020TC006339

Koptev, A., Burov, E., Gerya, T., Le Pourhiet, L., Leroy, S., Calais, E., & Jolivet, L. (2018). Plume-induced continental rifting and break-up in ultra-slow extension context: Insights from 3D numerical modeling. *Tectonophysics*, *746*, 121–137. https://doi.org/10.1016/j.tecto.2017.03.025

Koptev, A., Calais, E., Burov, E., Leroy, S., & Gerya, T. (2015). Dual continental rift systems generated by plume–lithosphere interaction. *Nature Geoscience*, *8*(5), 388–392. https://doi.org/10.1038/ngeo2401

KRISP working Group. (1987). Structure of the Kenya rift from seismic refraction. *Nature*, *325*(6101), 239–242. https://doi.org/10.1038/325239a0

Kronbichler, M., Heister, T., & Bangerth, W. (2012). High accuracy mantle convection simulation through modern numerical methods. *Geophysical Journal International*, *191*(1), 12–29. https://doi.org/10.1111/j.1365-246X.2012.05609.x

Lavier, L. L., & Manatschal, G. (2006). A mechanism to thin the continental lithosphere at magma-poor margins. *Nature*, *440*(March), 324–328. https://doi.org/10.1038/nature04608

Lee, H., Muirhead, J. D., Fischer, T. P., Ebinger, C. J., Kattenhorn, S. A., Sharp, Z. D., & Kianji, G. (2016). Massive and prolonged deep carbon emissions associated with continental rifting. *Nature Geoscience*, *9*(2), 145–149. https://doi.org/10.1038/ngeo2622

Lenardic, A., Moresi, L., & Mühlhaus, H. (2000). The role of mobile belts for the longevity of deep cratonic lithosphere: The Crumple Zone Model. *Geophysical Research Letters*, *27*(8), 1235–1238. https://doi.org/10.1029/1999GL008410

Lippard, S. J. (1973). The petrology of phonolites from the Kenya Rift. Lithos, 6(3), 217–234. https://doi.org/10.1016/0024-4937(73)90083-2

Macdonald, R., Rogers, N. W., Fitton, J. G., Black, S., & Smith, M. (2001). Plume–lithosphere interactions in the generation of the basalts of the Kenya Rift, East Africa. *Journal of* Petrology, *42*(5), 877–900. https://doi.org/10.1093/petrology/42.5.877

Macgregor, D. (2015). History of the development of the East African Rift System: A series of interpreted maps through time. *Journal of African Earth Sciences*, *101*, 232–252. https://doi.org/10.1016/j.jafrearsci.2014.09.016

McCall, G J.H. *Geology of the Nakuru-Thomson's Falls-Lake Hannington area degree sheet No. 35, S. W. quarter, and 43, N. W. quarter*. Survey, Min., Republic of Kenya.

Morley, C. K. (2010). Stress re-orientation along zones of weak fabrics in rifts: An explanation for pure extension in 'oblique' rift segments? *Earth and Planetary Science Letters*, *297*(3–4), 667–673. https://doi.org/10.1016/j.epsl.2010.07.022

Morley, C. K., Wescott, W. A., Stone, D. M., Harper, R. M., Wigger, S. T., & Karanja, F. M. (1992). Tectonic evolution of the northern Kenyan Rift. *Journal of the Geological Society*, *149*(3), 333–348. https://doi.org/10.1144/gsjgs.149.3.0333

Moucha, R., & Forte, A. M. (2011). Changes in African topography driven by mantle convection. *Nature Geoscience*, *4*(10), 707–712. https://doi.org/10.1038/ngeo1235

Mugisha, F., Ebinger, C. J., Strecker, M., & Pope, D. (1997). Two-stage rifting in the Kenya rift: implications for half-graben models. *Tectonophysics*, *278*(1–4), 63–81. https://doi.org/10.1016/S0040-1951(97)00095-4

Muirhead, J. D., & Kattenhorn, S. A. (2018). Activation of preexisting transverse structures in an evolving magmatic rift in East Africa. *Journal of Structural Geology, 106*, 1–18. https://doi.org/10.1016/j.jsg.2017.11.004

Muirhead, J. D., Kattenhorn, S. A., & Le Corvec, N. (2015). Varying styles of magmatic strain accommodation across the East African Rift. *Geochemistry, Geophysics, Geosystems*, *16*(8), 2775–2795. https://doi.org/10.1002/2015GC005918

Muirhead, J. D., Kattenhorn, S. A., Lee, H., Mana, S., Turrin, B. D., Fischer, T. P., et al. (2016). Evolution of upper crustal faulting assisted by magmatic volatile release during early-stage continental rift development in the East African Rift. *Geosphere*, *12*(6), 1670–1700. https://doi.org/10.1130/GES01375.1

Mulibo, G. D., & Nyblade, A. A. (2013). The P and S wave velocity structure of the mantle beneath eastern Africa and the African superplume anomaly. *Geochemistry, Geophysics, Geosystems*, *14*(8), 2696–2715. https://doi.org/10.1002/ggge.20150

Muluneh, A. A., Brune, S., Illsley-Kemp, F., Corti, G., Keir, D., Glerum, A., et al. (2020). Mechanism for deep crustal seismicity: Insight from modeling of deformation process at the Main Ethiopian Rift. *Geochemistry, Geophysics, Geosystems*, *21*(7), e2020GC008935. https://doi.org/10.1029/2020GC008935

Naliboff, J. B., Buiter, S. J. H., Péron-Pinvidic, G., Osmundsen, P. T., & Tetreault, J. (2017). Complex fault interaction controls continental rifting. *Nature Communications*, *8*(1), 1179. https://doi.org/10.1038/s41467-017-00904-x

Naliboff, J. B., Glerum, A., Brune, S., Péron-Pinvidic, G., & Wrona, T. (2020). Development of 3D rift heterogeneity through fault network evolution. *Geophysical Research Letters*, e2019GL086611. https://doi.org/10.1029/2019GL086611

Neuharth, D., Brune, S., Glerum, A., Heine, C., & Welford, J. K. (2021). Formation of continental microplates through rift linkage: Numerical modelling and its application to the Flemish Cap and Sao Paulo Plateau. *Geochemistry, Geophysics, Geosystems*, *n/a*(n/a), e2020GC009615. https://doi.org/10.1029/2020GC009615

Oliva, S. J., Ebinger, C. J., Wauthier, C., Muirhead, J. D., Roecker, S. W., Rivalta, E., et al. (2019). Insights Into Fault-Magma Interactions in an Early-Stage Continental Rift From Source Mechanisms and Correlated Volcano-Tectonic Earthquakes. *Geophysical Research Letters, 46*(4), 2065–2074. https://doi.org/10.1029/2018GL080866

Osei Tutu, A., Steinberger, B., Sobolev, S. V., Rogozhina, I., & Popov, A. A. (2018). Effects of upper mantle heterogeneities on the lithospheric stress field and dynamic topography. *Solid Earth*, *9*(3), 649–668. https://doi.org/10.5194/se-9-649-2018

Pérez-Gussinyé, M., Andrés-Martínez, M., Araújo, M., Xin, Y., Armitage, J., & Morgan, J. P. (2020). Lithospheric strength and rift migration controls on synrift stratigraphy and breakup unconformities at rifted margins: Examples from numerical models, the Atlantic and South China Sea mar-gins. *Tectonics, 39*, e2020TC006255.

Peron-Pinvidic, G., Manatschal, G., & the "IMAGinING RIFTING" Workshop Participants (2019). Rifted Margins: State of the Art and Future Challenges. *Frontiers in Earth Science*, *7*. https://doi.org/10.3389/feart.2019.00218

Persaud, P., Tan, E., Contreras, J., & Lavier, L. L. (2017). A bottom-driven mechanism for distributed faulting in the Gulf of California rift. *Tectonophysics*, *719–720*, 51–65. https://doi.org/10.1016/j.tecto.2016.11.024

Petersen, K. D., & Schiffer, C. (2016). Wilson cycle passive margins: Control of orogenic inheritance on continental breakup. *Gondwana Research*, *39*, 131–144. https://doi.org/10.1016/j.gr.2016.06.012

Petit, C., & Deverchere, J. (2006). Structure and evolution of the Baikal rift: a synthesis. *Geochemistry, Geophysics, Geosystems*, *7*(11). https://doi.org/10.1029/2006GC001265

Phillips, T. B., Jackson, C. A.-L., Bell, R. E., Duffy, O. B., & Fossen, H. (2016). Reactivation of intrabasement structures during rifting: A case study from offshore southern Norway. *Journal of Structural Geology*, *91*, 54–73. https://doi.org/10.1016/j.jsg.2016.08.008

Pik, R., Marty, B., & Hilton, D. R. (2006). How many mantle plumes in Africa? The geochemical point of view. *Chemical Geology*, *226*(3–4), 100–114. https://doi.org/10.1016/j.chemgeo.2005.09.016

Plasman, M., Tiberi, C., Ebinger, C., Gautier, S., Albaric, J., Peyrat, S., et al. (2017). Lithospheric low-velocity zones associated with a magmatic segment of the Tanzanian Rift, East Africa. *Geophysical Journal International*, *210*(1), 465–481. https://doi.org/10.1093/gji/ggx177

Randel, R. P., & Johnson, R. W. (1970). *Geological map of the Suswa area.* Ministry of Natural Resources, Mines & Geological Department, Kenya.

Riedl, S., Melnick, D., Mibei, G. K., Njue, L., & Strecker, M. R. (2020). Continental rifting at magmatic centres: structural implications from the Late Quaternary Menengai Caldera, central Kenya Rift. *Journal of the Geological Society, 177*(1), 153-169.

Ring, U. (2014). The East African Rift System. *Austrian Journal of Earth Sciences*, *107*(1).

Robertson, E. a. M., Biggs, J., Cashman, K. V., Floyd, M. A., & Vye-Brown, C. (2015). Influence of regional tectonics and pre-existing structures on the formation of elliptical calderas in the Kenyan Rift. *Geological Society, London, Special Publications, 420*(1), 43–67. https://doi.org/10.1144/SP420.12

Rooney, T. O. (2020). The Cenozoic magmatism of East Africa: Part II – Rifting of the mobile belt. *Lithos*, *360–361*, 105291. https://doi.org/10.1016/j.lithos.2019.105291

Rooney, T. O., Herzberg, C., & Bastow, I. D. (2012). Elevated mantle temperature beneath East Africa. *Geology*, *40*(1), 27–30. https://doi.org/10.1130/G32382.1

Ros, E., Pérez-Gussinyé, M., Araújo, M., Thoaldo Romeiro, M., Andrés-Martínez, M., & Morgan, J. P. (2017). Lower Crustal Strength Controls on Melting and Serpentinization at Magma-Poor Margins: Potential Implications for the South Atlantic. *Geochemistry, Geophysics, Geosystems*, *18*(12), 4538–4557. https://doi.org/10.1002/2017GC007212

Rose, I., Buffett, B., & Heister, T. (2017). Stability and accuracy of free surface time integration in viscous flows. *Physics of the Earth and Planetary Interiors*, *262*, 90–100. https://doi.org/10.1016/j.pepi.2016.11.007

Rowland, J. V., Baker, E., Ebinger, C. J., Keir, D., Kidane, T., Biggs, J., et al. (2007). Fault growth at a nascent slow-spreading ridge: 2005 Dabbahu rifting episode, Afar. *Geophysical Journal International, 171*(3), 1226–1246. https://doi.org/10.1111/j.1365-246X.2007.03584.x

Rutter, E. H., & Brodie, K. H. (2004). Experimental grain size-sensitive flow of hot-pressed Brazilian quartz aggregates. *Journal of Structural Geology*, *26*(11), 2011–2023. https://doi.org/10.1016/j.jsg.2004.04.006

Rybacki, E., Gottschalk, M., Wirth, R., & Dresen, G. (2006). Influence of water fugacity and activation volume on the flow properties of fine-grained anorthite aggregates. *Journal of Geophysical Research: Solid Earth*, *111*(B3). https://doi.org/10.1029/2005JB003663

Saggerson, E. P. (1970). The structural control and genesis of alkaline rocks in central Kenya. *Bulletin Volcanologique*, *34*(1), 38–76. https://doi.org/10.1007/BF02597779

Saggerson, E. P. (1991). *Geology of the Nairobi area, degree sheet 51, NE Quarter (Geological Survey of Kenya Report No. 98*. Nairobi, Kenya: Ministry of Environment and Natural Resources, Mines and Geological Department.

Salazar-Mora, C. A., Huismans, R. S., Fossen, H., & Egydio-Silva, M. (2018). The Wilson Cycle and Effects of Tectonic Structural Inheritance on Rifted Passive Margin Formation. *Tectonics*, *37*(9), 3085–3101. https://doi.org/10.1029/2018TC004962

Sandiford, D., Brune, S., Glerum, A., Naliboff, J., & Whittaker, J. M. (2021). Kinematics of footwall exhumation at oceanic detachment faults:solid-block rotation and apparent unbending. *Geochemistry, Geophysics, Geosystems*, e2021GC009681. https://doi.org/10.1029/2021GC009681

Saria, E., Calais, E., Stamps, D. S., Delvaux, D., & Hartnady, C. J. H. (2014). Present-day kinematics of the East African Rift. *Journal of Geophysical Research: Solid Earth*, *119*(4), 3584–3600. https://doi.org/10.1002/2013JB010901

Schilling, J.-G. (1991). Fluxes and excess temperatures of mantle plumes inferred from their interaction with migrating mid-ocean ridges. *Nature*, *352*(6334), 397–403.

Schlische, R. W. (2003). Progress in understanding the structural geology, basin evolution, and tectonic history of the eastern North American rift system. *The great rift valleys of Pangea in eastern North America, 1*, 21–64. https://doi.org/10.7312/leto11162-003

Schumacher, M. E. (2002). Upper Rhine Graben: role of preexisting structures during rift evolution. *Tectonics*, *21*(1). https://doi.org/10.1029/2001TC900022

Schwarz, M., & Henk, A. (2005). Evolution and structure of the Upper Rhine Graben: insights from three-dimensional thermomechanical modelling. *International Journal of Earth Sciences*, *94*(4), 732–750. https://doi.org/10.1007/s00531-004-0451-2

Shackleton, R. M. (1945). Geology of the Nyeri area. *Geological Survey of Kenya Report, 12*.

Shackleton, R. M. (1976). A Discussion on global tectonics in Proterozoic times-Pan-African Structures. *Philosophical Transactions of the Royal Society of London. Series A, Mathematical and Physical Sciences*, *280*(1298), 491–497. https://doi.org/10.1098/rsta.1976.0008

Shackleton, R. M. (1978). Structural development of the East African Rift system. *Geological Society, London, Special Publications, 6*(1), 19–28. https://doi.org/10.1144/GSL.SP.1978.006.01.04

Shackleton, R. M. (1993). Tectonics of the Mozambique Belt in East Africa. *Geological Society, London, Special Publications*, *76*(1), 345–362. http://dx.doi.org/10.1144/GSL.SP.1993.076.01.17

Shackleton, R. M., & Ries, A. C. (1984). The relation between regionally consistent stretching lineations and plate motions. *Journal of Structural Geology*, *6*(1-2), 111–117. https://doi.org/10.1016/0191-8141(84)90089-0

Sippel, J., Meeßen, C., Cacace, M., Mechie, J., Fishwick, S., Heine, C., et al. (2017). The Kenya rift revisited: Insights into lithospheric strength through data-driven 3-D gravity and thermal modelling. *Solid Earth*, *8*(1), 45–81. https://doi.org/10.5194/se-8-45-2017

Smith, M. (1994). Stratigraphic and structural constraints on mechanisms of active rifting in the Gregory Rift, Kenya. *Tectonophysics, 236*(1–4), 3–22. https://doi.org/10.1016/0040-1951(94)90166-X

Smith, M., & Mosley, P. (1993). Crustal heterogeneity and basement influence on the development of the Kenya Rift, East Africa. *Tectonics, 12*(2), 591–606. https://doi.org/10.1029/92TC01710

Sobolev, S. V., Sobolev, A. V., Kuzmin, D. V., Krivolutskaya, N. A., Petrunin, A. G., Arndt, N. T., et al. (2011). Linking mantle plumes, large igneous provinces and environmental catastrophes. *Nature*, *477*(7364), 312–316. https://doi.org/10.1038/nature10385

Sokoutis, D., Corti, G., Bonini, M., Brun, J. P., Cloetingh, S., Mauduit, T., & Manetti, P. (2007). Modeling the extension of heterogeneous hot lithosphere. *Tectonophysics*, *444*(1–4), 63–79. https://doi.org/10.1016/j.tecto.2007.08.012

Stab, M., Bellahsen, N., Pik, R., Quidelleur, X., Ayalew, D., & Leroy, S. (2015). Modes of rifting in magma-rich settings: Tectono-magmatic evolution of Central Afar. *Tectonics, 35*(1), 2–38. https://doi.org/10.1002/2015TC003893

Stamps, D. S., Calais, E., Saria, E., Hartnady, C., Nocquet, J. M., Ebinger, C. J., & Fernandes, R. M. (2008). A kinematic model for the East African Rift. *Geophysical Research Letters*, *35*(5). https://doi.org/10.1029/2007GL032781

Stamps, D. S., Iaffaldano, G., & Calais, E. (2015). Role of mantle flow in Nubia-Somalia plate divergence. *Geophysical Research Letters*, *42*(2), 290–296. https://doi.org/10.1002/2014GL062515

Strecker, M. R., Blisniuk, P. M., & Eisbacher, G. H. (1990). Rotation of extension direction in the central Kenya Rift. *Geology*, *18*(4), 299. https://doi.org/10.1130/0091-7613(1990)018<0299:ROEDIT>2.3.CO;2

Strecker, M. R. (1991). *Das zentrale und südliche Kenia-Rift unter besonderer Berücksichtigung der neotektonischen Entwicklung* (Habilitation thesis). University of Karlsruhe.

Supak, S., Bohnenstiehl, D. R., & Buck, W. R. (2006). Flexing is not stretching: An analogue study of flexure-induced fault populations. *Earth and Planetary Science Letters, 246*(1), 125–137. https://doi.org/10.1016/j.epsl.2006.03.028

Svartman Dias, A. E., Lavier, L. L., & Hayman, N. W. (2015). Conjugate rifted margins width and asymmetry: The interplay between lithospheric strength and thermomechanical processes. *Journal of Geophysical Research: Solid Earth*, *120*(12), 8672–8700. https://doi.org/10.1002/2015JB012074

Tetreault, J. L., & Buiter, S. J. H. (2018). The influence of extension rate and crustal rheology on the evolution of passive margins from rifting to break-up. *Tectonophysics*, *746*, 155–172. https://doi.org/10.1016/j.tecto.2017.08.029

Thompson, A. O., & Dodson, R. G. (1963). Geology of the Naivasha area. *Geological Survey of Kenya Report, 55*, 1-80.

Thybo, H., Maguire, P. K. H., Birt, C., & Perchuć, E. (2000). Seismic reflectivity and magmatic underplating beneath the Kenya Rift. *Geophysical Research Letters, 27*(17), 2745–2748. https://doi.org/10.1029/1999GL011294

Tiercelin, J.-J., & Lezzar, K.-E. (2002). A 300 Million Years History of Rift Lakes in Central and East Africa: An Updated Broad Review In *The East African great lakes: limnology, palaeolimnology and biodiversity* (pp. 3-60). Springer, Dordrecht. https://doi.org/10.1007/0-306-48201-0_1

Tongue, J. A., Maguire, P. K. H., & Young, P. A. V. (1992). Seismicity distribution from temporary earthquake recording networks in Kenya. *Tectonophysics, 204*(1–2), 71–79. https://doi.org/10.1016/0040-1951(92)90270-G

Torres Acosta, V. V., Bande, A., Sobel, E. R., Parra, M., Schildgen, T. F., Stuart, F., & Strecker, M. R. (2015). Cenozoic extension in the Kenya Rift from low-temperature thermochronology: Links to diachronous spatiotemporal evolution of rifting in East Africa. *Tectonics*, *34*(12), 2367–2386. https://doi.org/10.1002/2015TC003949

Tugume, F., Nyblade, A., & Julià, J. (2012). Moho depths and Poisson's ratios of Precambrian crust in East Africa: Evidence for similarities in Archean and Proterozoic crustal structure. *Earth and Planetary Science Letters*, *355–356*, 73–81. https://doi.org/10.1016/j.epsl.2012.08.041

Ulvrova, M. M., Brune, S., & Williams, S. (2019). Breakup Without Borders: How Continents Speed Up and Slow Down During Rifting. *Geophysical Research Letters*, *46*(3), 1338–1347. https://doi.org/10.1029/2018GL080387

Weinstein, A., Oliva, S. J., Ebinger, C. J., Roecker, S., Tiberi, C., Aman, M., et al. (2017). Fault-magma interactions during early continental rifting: Seismicity of the Magadi-Natron-Manyara basins, Africa. *Geochemistry, Geophysics, Geosystems*, *18*(10), 3662–3686. https://doi.org/10.1002/2017GC007027

Wichura, H., Bousquet, R., Oberhänsli, R., Strecker, M. R., & Trauth, M. H. (2010). Evidence for middle Miocene uplift of the East African Plateau. *Geology*, *38*(6), 543–546. https://doi.org/10.1130/G31022.1

Wichura, H., Jacobs, L. L., Lin, A., Polcyn, M. J., Manthi, F. K., Winkler, D. A., et al. (2015). A 17-My-old whale constrains onset of uplift and climate change in east Africa. *Proceedings of the National Academy of Sciences*, *112*(13), 3910–3915. https://doi.org/10.1073/pnas.1421502112

Williams, L. A. J. (1969a). Geochemistry and petrogenesis of the Kilimanjaro volcanic rocks of the Amboseli area, Kenya. *Bulletin Volcanologique*, *33*(3), 862-888. https://doi.org/10.1007/BF02596754

Williams, L. A. J. (1969b). Volcanic associations in the Gregory rift valley, east Africa. *Nature, 224*(5214), 61-64. https://doi.org/10.1038/224061a0

Williams, L. A. J. (1972). The Kenya rift volcanics: a note on volumes and chemical composition. *Tectonophysics, 15*(1-2), 83-96. https://doi.org/10.1016/0040-1951(72)90054-6

Withjack, M. O., Schlische, R. W., Malinconico, M. L., & Olsen, P. E. (2013). Rift-basin development: lessons from the Triassic–Jurassic Newark Basin of eastern North America. *Geological Society, London, Special Publications, 369*(1), 301–321. https://doi.org/10.1144/SP369.13

Wright, T. J., Ebinger, C., Biggs, J., Ayele, A., Yirgu, G., Keir, D., & Stork, A. (2006). Magma-maintained rift segmentation at continental rupture in the 2005 Afar dyking episode. *Nature*, *442*(7100), 291–294. https://doi.org/10.1038/nature04978

Zielke, O., & Strecker, M. R. (2009). Recurrence of large earthquakes in magmatic continental rifts: insights from a paleoseismic study along the Laikipia–Marmanet Fault, Subukia Valley, Kenya Rift. *Bulletin of the Seismological Society of America, 99*(1), 61-70. https://doi.org/10.1785/0120080015

Zwaan, F., Schreurs, G., & Rosenau, M. (2019). Rift propagation in rotational versus orthogonal extension: Insights from 4D analogue models. *Journal of Structural Geology*, *135*, 103946. https://doi.org/10.1016/j.jsg.2019.103946

5 Conclusions

In this thesis, the overarching subject of localisation of deformation was split into the two major topics *strain localisation in ductile shear zones* and *localisation of deformation during continental rifting* and presented in the form of three published papers. Chapter 2 and 3 addressed localisation in ductile shear zones by conducting rock experiments and numerical models, while chapter 4 encompassed a numerical study investigating the tectonic evolution of the Southern Kenya Rift. These studies contribute to the discussion about governing mechanisms, parameters, and boundary conditions in geodynamics on different spatial and time scales.

The experimental study aimed at investigating the initial and transient stages of strain localization of a ductile shear zone and test whether and how the imposed loading conditions affect the localisation process for a setup that is known to feature strain localisation. Therefore, Carrara marble cylinders with single inclusions of Solnhofen limestone were twisted in a Paterson apparatus at high temperature (900 °C) and confining pressure (400 MPa). During the experiment, a shear zone forms from a propagating process zone, which is induced by stress concentrations in the strong matrix around the weak inclusion. The areally limited weakening of the marble matrix is accommodated by CPO development, plastic grain deformation and dynamic recrystallisation. Besides the prevailing high temperature creep of marble, evidence for minor amounts of brittle deformation is found. This combination is commonly observed in nature, where the fractures are interpreted as a precursor to localization (e.g. Mancktelow & Pennacchioni, 2005) or as a hint to coexisting brittle and ductile deformation (e.g. Poulet et al., 2014). In a previous study, constant torque boundary conditions were found to enable strain localization for an olivine aggregate, while constant strain rate failed to produce the same result (Hansen et al., 2012). Varying between constant twist and constant torque yields similar results in our experiments, suggesting that loading conditions do not significantly affect the localisation process and initiation of a rheological shear zone. The heterogeneous initial stress distribution due to the setup configuration has a greater impact on the evolution of deformation than the boundary condition. Hence on this spatial scale, effects of the boundary loading conditions are probably neglectable for multiphase material assemblages that feature high viscosity contrasts. However, variables like confining pressure or a second mineral phase in the matrix may affect the localisation process and an assessment requires further research. For larger scales on the other hand, like a divergent rift scenario, large differences exist between constant force and constant velocity boundary conditions. For example, in numerical models of divergent rifts, constant force boundary conditions alone would lead to a runaway effect once the lithospheric strength undercuts a threshold (Brune et al., 2016).

Building on the laboratory experiments, numerical models were conducted where a piece-wise linear softening law was developed, that describes the weakening of Carrara marble during deformation at 900°C. This simple law reduces the effective viscosity of the material by a factor which depends on the local strain and can reproduce the rheological weakening observed in the laboratory experiments. The developed numerical model is a virtual way of analysing the process zone evolution by extending the observable and variable parameters as compared to laboratory experiments. The four phases of process zone and shear zone evolution (P1) *pre-weakening*, (P2) *onset and acceleration of weakening*, (P3) *deceleration of weakening* and (P4) *steady-state* can be distinguished. Local stress peaks at the inclusion tips induced by viscosity contrasts are crucial for matrix strain localisation. With increasing strain, the process zone expands into the matrix until a full shear band is established. Stress strain curves from laboratory experiments for different (geo-)materials often feature stress drops in the same order of magnitude as with the studied marble. This stress drop can also be described as an effect of rheological weakening which is necessary to establish a shear zone in the given setting with limestone and marble. The amount of rheological weakening controls the shear zone width and the localisation rate. This also holds for the development of the anastomosing and nested structure of ultramylonites, reinforcing the importance of accounting for rheological weakening in numerical models. The usage of simple softening laws is efficient and saves computational resources. Benchmarking them with laboratory experiments helps to produce reasonable numbers. This benchmarking procedure could be performed on already published studies of such rheological experiments to establish weakening laws for other materials and for a broader range of conditions. For the numerical modelling community this may be an opportunity to enhance the already used softening laws.

The scale was changed for the third paper of this thesis. In this study, a 2D numerical model was developed that integrated geophysical and geological data to study and explain the tectonic evolution of the Southern and Central Kenya Rift. The main processes and steps of this evolution involve (1) a broad zone of low deformation and competing faults and localisation of a single border fault, (2) development of a secondary, conjugate border fault and (3) the formation of a shallow fault network in rotating and bending hanging-wall block in the rift centre. The purely tectonic model can reproduce first-order characteristics of the rift, despite not featuring volcanic activity which is omnipresent in the Kenya Rift and known to affect tectonic evolution often strongly. A random noise implementation of initial strain can address along-strike variations of a rift in 2D setup. The bulk lithospheric behaviour during rifting is controlled by structural inheritance (Jammes & Lavier, 2019). With the initial strain implementation, the effect of small-scale crustal inheritance on the first-order faults and general rift geometry could be shown.

Regarding the current scientific knowledge about the effect of loading conditions on deformation and localisation of multiphase materials with high viscosity contrasts, the experiments of the first manuscript suggest that there is no substantial difference between loading by constant stress and constant strain rate. A new method of generating softening

laws based on laboratory experiments, was established within the second manuscript. This is a useful tool to generate reasonable values for strain softening implementations in numerical modelling software. Finally, with the third study, it was shown that a purely tectonic model can be sufficient to generate first-order characteristics of parts of the Kenya Rift and that a random noise implementation of initial strain elucidates the effect of small-scale inheritance. Due to the large range of spatial and temporal scales involved in rock deformation, this kind of multi-disciplinary approach that bridges laboratory experiments, natural observations, and physics-based process-modelling holds strong potential for future research.

References/Bibliography

Artemjev, M. E., & Artyushkov, E. V. (1971). Structure and isostasy of the Baikal Rift and the mechanism of rifting. *Journal of Geophysical Research*, *76*(5), 1197–1211. https://doi.org/10.1029/JB076i005p01197

Bangerth, W., Austermann, J., Bürg, M., Cox, S., Durkin, W., Euen, G., … Zhang, S. (2019). ASPECT: Advanced Solver for Problems in Earth's ConvecTion, User Manual. https://doi.org/10.6084/m9.figshare.4865333

Bangerth, W., Dannberg, J., Gassmoeller, R., & Heister, T. (2018). Aspect V2.0.1. https://doi.org/10.5281/zenodo.1297145

Barrionuevo, M., Liu, S., Mescua, J., Yagupsky, D., Quinteros, J., Giambiagi, L., … Strecker, M. R. (2021). The influence of variations in crustal composition and lithospheric strength on the evolution of deformation processes in the southern Central Andes: insights from geodynamic models. *International Journal of Earth Sciences*. https://doi.org/10.1007/s00531-021-01982-5

Bialas, R. W., Buck, W. R., & Qin, R. (2010). How much magma is required to rift a continent? *Earth and Planetary Science Letters*, *292*(1–2), 68–78. https://doi.org/10.1016/j.epsl.2010.01.021

Bredow, E., & Steinberger, B. (2021). Mantle Convection and Possible Mantle Plumes beneath Antarctica - Insights from Geodynamic Models and Implications for Topography. *Geological Society, London, Memoirs*, M56-2020–2. https://doi.org/10.1144/M56-2020-2

Brune, S. (2016). Rifts and Rifted Margins: A Review of Geodynamic Processes and Natural Hazards. *Plate Boundaries and Natural Hazards*, 11–37. https://doi.org/10.1002/9781119054146.ch2

Brune, S. (2019). *Modelling continental rift dynamics (habilitation thesis)*. Universität Potsdam, Potsdam, Germany. https://doi.org/10.25932/publishup-43236

Brune, S., Williams, S. E., Butterworth, N. P., & Müller, R. D. (2016). Abrupt plate accelerations shape rifted continental margins. *Nature*, *536*(7615), 201. https://doi.org/10.1038/nature18319

Buck, W. R. (1991). Modes of continental lithospheric extension. *Journal of Geophysical Research: Solid Earth*, *96*(B12), 20161–20178. https://doi.org/10.1029/91JB01485

Buck, W. R. (2004). Consequences of Asthenospheric Variability on Continental Rifting. In *Rheology and Deformation of the Lithosphere at Continental Margins* (pp. 1–30). New York: Columbia University Press. https://doi.org/10.7312/karn12738-002

Bürgmann, R., & Dresen, G. (2008). Rheology of the Lower Crust and Upper Mantle: Evidence from Rock Mechanics, Geodesy, and Field Observations. *Annual Review of Earth and Planetary Sciences*, *36*(1), 531–567. https://doi.org/10.1146/annurev.earth.36.031207.124326

Burlini, L., & Bruhn, D. (2005). High-strain zones: laboratory perspectives on strain softening during ductile deformation. *Geological Society, London, Special Publications*, *245*(1), 1–24. https://doi.org/10.1144/GSL.SP.2005.245.01.01

Bystricky, M., & Mackwell, S. (2001). Creep of dry clinopyroxene aggregates. *Journal of Geophysical Research: Solid Earth*, *106*(B7), 13443–13454. https://doi.org/10.1029/2001JB000333

Cloetingh, S., Wortel, R., & Vlaar, N. J. (1989). On the Initiation of Subduction Zones. In *Subduction Zones Part II* (pp. 7–25). Basel: Birkhäuser Basel. https://doi.org/10.1007/978-3-0348-9140-0_2

Coulomb, C. A. (1776). Essai sur une application des regles maximis et minimis a quelques problems de statique, relatives a l'architecture. *Mémoires de l'Académie Royale Des Sciences*, *7*, 343–382.

Cyprych, D., Brune, S., Piazolo, S., & Quinteros, J. (2016). Strain localization in polycrystalline material with second phase particles: Numerical modeling with application to ice mixtures. *Geochemistry, Geophysics, Geosystems*, *17*(9), 3608–3628. https://doi.org/10.1002/2016GC006471

Daniels, K. A., Bastow, I. D., Keir, D., Sparks, R. S. J., & Menand, T. (2014). Thermal models of dyke intrusion during development of continent–ocean transition. *Earth and Planetary Science Letters*, *385*, 145–153. https://doi.org/10.1016/j.epsl.2013.09.018

Dimanov, A., & Dresen, G. (2005). Rheology of synthetic anorthite-diopside aggregates: Implications for ductile shear zones. *Journal of Geophysical Research: Solid Earth*, *110*(B7). https://doi.org/10.1029/2004JB003431

Döhmann, M. J. E. A., Brune, S., Nardini, L., Rybacki, E., & Dresen, G. (2019). Strain Localization and Weakening Processes in Viscously Deforming Rocks: Numerical Modeling Based on Laboratory Torsion Experiments. *Journal of Geophysical Research: Solid Earth*, *124*(1). https://doi.org/10.1029/2018JB016917

Duclaux, G., Huismans, R. S., & May, D. A. (2020). Rotation, narrowing, and preferential reactivation of brittle structures during oblique rifting. *Earth and Planetary Science Letters*, *531*, 115952. https://doi.org/10.1016/j.epsl.2019.115952

Duretz, T., Petri, B., Mohn, G., Schmalholz, S. M., Schenker, F. L., & Müntener, O. (2016). The importance of structural softening for the evolution and architecture of passive margins. *Scientific Reports*, *6*(38704). https://doi.org/10.1038/srep38704

Faccenna, C., Becker, T. W., Holt, A. F., & Brun, J. P. (2021). Mountain building, mantle convection, and supercontinents: revisited. *Earth and Planetary Science Letters*, *564*, 116905. https://doi.org/10.1016/j.epsl.2021.116905

Fossen, H., & Cavalcante, G. C. G. (2017). Shear zones – A review. *Earth-Science Reviews*, *171*, 434–455. https://doi.org/10.1016/j.earscirev.2017.05.002

Gardner, R., Piazolo, S., Evans, L., & Daczko, N. (2017). Patterns of strain localization in heterogeneous, polycrystalline rocks – a numerical perspective. *Earth and Planetary Science Letters*, *463*, 253–265. https://doi.org/10.1016/j.epsl.2017.01.039

Goetze, C., & Evans, B. (1979). Stress and temperature in the bending lithosphere as constrained by experimental rock mechanics. *Geophysical Journal International*, *59*(3), 463–478. https://doi.org/10.1111/j.1365-246X.1979.tb02567.x

Grotzinger, J., & Jordan, T. (2010). *Understanding Earth* (6th ed.). New York: W. H. Freeman and Company.

Gueydan, F., Précigout, J., & Montési, L. G. J. (2014). Strain weakening enables continental plate tectonics. *Tectonophysics*, *631*, 189–196. https://doi.org/10.1016/j.tecto.2014.02.005

Hansen, L. N., Zimmerman, M. E., Dillman, A. M., & Kohlstedt, D. L. (2012). Strain localization in olivine aggregates at high temperature: A laboratory comparison of constant-strain-rate and constant-stress boundary conditions. *Earth and Planetary Science Letters*, *333*, 134–145. https://doi.org/10.1016/j.epsl.2012.04.016

Heckenbach, E. L., Brune, S., Glerum, A. C., & Bott, J. (2021). Is There a Speed Limit for the Thermal Steady-State Assumption in Continental Rifts? *Geochemistry, Geophysics, Geosystems*, *22*(3). https://doi.org/10.1029/2020GC009577

Heister, T., Dannberg, J., Gassmöller, R., & Bangerth, W. (2017). High accuracy mantle convection simulation through modern numerical methods - II: Realistic models and problems. *Geophysical Journal International*, *210*(2), 833–851. https://doi.org/10.1093/gji/ggx195

Hirth, G., & Kohlstedt, D. (2004). Rheology of the upper mantle and the mantle wedge: A view from the experimentalists. *Geophysical Monograph Series*, *138*, 83–105. https://doi.org/10.1029/138GM06

Hirth, G., & Tullis, J. (1992). Dislocation creep regimes in quartz aggregates. *Journal of Structural Geology*, *14*(2), 145–159. https://doi.org/10.1016/0191-8141(92)90053-Y

Hodge, M., Fagereng, Å., Biggs, J., & Mdala, H. (2018). Controls on Early-Rift Geometry: New Perspectives From the Bilila-Mtakataka Fault, Malawi. *Geophysical Research Letters*, *45*(9), 3896–3905. https://doi.org/10.1029/2018GL077343

Jammes, S., & Lavier, L. L. (2019). Effect of contrasting strength from inherited crustal fabrics on the development of rifting margins. *Geosphere*, *15*(2), 407–422. https://doi.org/10.1130/GES01686.1

Kiss, D., Podladchikov, Y., Duretz, T., & Schmalholz, S. M. (2019). Spontaneous generation of ductile shear zones by thermal softening: Localization criterion, 1D to 3D modelling and application to the lithosphere. *Earth and Planetary Science Letters*, *519*, 284–296. https://doi.org/10.1016/j.epsl.2019.05.026

Kronbichler, M., Heister, T., & Bangerth, W. (2012). High accuracy mantle convection simulation through modern numerical methods. *Geophysical Journal International*, *191*(1), 12–29. https://doi.org/10.1111/j.1365-246X.2012.05609.x

Mancktelow, N. S., & Pennacchioni, G. (2005). The control of precursor brittle fracture and fluid-rock interaction on the development of single and paired ductile shear zones. *Journal of Structural Geology*, *27*(4), 645–661. https://doi.org/10.1016/j.jsg.2004.12.001

Mazzotti, S., & Gueydan, F. (2018). Control of tectonic inheritance on continental intraplate strain rate and seismicity. *Tectonophysics*, *746*, 602–610. https://doi.org/10.1016/j.tecto.2017.12.014

Mohr, O. (1900). Welche Umstände bedingen die Elastizitätsgrenze und den Bruch eines Materials. *Zeitschrift Des Vereins Deutscher Ingenieure*, *46*(1524–1530), 1572–1577.

Mulyukova, E., & Bercovici, D. (2019). The Generation of Plate Tectonics From Grains to Global Scales: A Brief Review. *Tectonics*, *38*(12), 4058–4076. https://doi.org/10.1029/2018TC005447

Osei Tutu, A., Steinberger, B., Sobolev, S. V., Rogozhina, I., & Popov, A. A. (2018). Effects of upper mantle heterogeneities on the lithospheric stress field and dynamic topography. *Solid Earth*, *9*(3), 649–668. https://doi.org/10.5194/se-9-649-2018

Pennacchioni, G., & Mancktelow, N. S. (2007). Nucleation and initial growth of a shear zone network within compositionally and structurally heterogeneous granitoids under amphibolite facies conditions. *Journal of Structural Geology*, *29*(11), 1757–1780. https://doi.org/10.1016/j.jsg.2007.06.002

Pieri, M., Burlini, L., Kunze, K., Stretton, I., & Olgaard, D. L. (2001). Rheological and microstructural evolution of Carrara marble with high shear strain: results from high temperature torsion experiments. *Journal of Structural Geology*, *23*(9), 1393–1413. https://doi.org/10.1016/S0191-8141(01)00006-2

Platt, J. P., & Behr, W. M. (2011). Grainsize evolution in ductile shear zones: Implications for strain localization and the strength of the lithosphere. *Journal of Structural Geology*, *33*(4), 537–550. https://doi.org/10.1016/j.jsg.2011.01.018

Popov, A. A., & Sobolev, S. V. (2008). SLIM3D: A tool for three-dimensional thermomechanical modeling of lithospheric deformation with elasto-visco-plastic rheology. *Physics of the Earth and Planetary Interiors*, *171*(1-4), 55–75. https://doi.org/10.1016/j.pepi.2008.03.007

Poulet, T., Veveakis, M., Herwegh, M., Buckingham, T., & Regenauer-Lieb, K. (2014). Modeling episodic fluid-release events in the ductile carbonates of the Glarus thrust. *Geophysical Research Letters*, *41*(20), 7121–7128. https://doi.org/10.1002/2014GL061715

Rutter, E. H., & Brodie, K. H. (2004). Experimental grain size-sensitive flow of hot-pressed Brazilian quartz aggregates. *Journal of Structural Geology*, *26*(11), 2011–2023. https://doi.org/10.1016/j.jsg.2004.04.006

Rybacki, E., & Dresen, G. (2000). Dislocation and diffusion creep of synthetic anorthite aggregates. *Journal of Geophysical Research: Solid Earth*, *105*(B11), 26017–26036. https://doi.org/10.1029/2000JB900223

Rybacki, E., Gottschalk, M., Wirth, R., & Dresen, G. (2006). Influence of water fugacity and activation volume on the flow properties of fine-grained anorthite aggregates. *Journal of Geophysical Research: Solid Earth*, *111*(B3). https://doi.org/10.1029/2005JB003663

Rybacki, E., Morales, L. F. G., Naumann, M., & Dresen, G. (2014). Strain localization during high temperature creep of marble: The effect of inclusions. *Tectonophysics*, *634*, 182–197. https://doi.org/10.1016/j.tecto.2014.07.032

Salazar-Mora, C. A., Huismans, R. S., Fossen, H., & Egydio-Silva, M. (2018). The Wilson Cycle and Effects of Tectonic Structural Inheritance on Rifted Passive Margin Formation. *Tectonics*, *37*(9), 3085–3101. https://doi.org/10.1029/2018TC004962

Sandiford, D., Brune, S., Glerum, A., Naliboff, J., & Whittaker, J. M. (2021). Kinematics of footwall exhumation at oceanic detachment faults: solid-block rotation and apparent unbending. *Geochemistry, Geophysics, Geosystems*. https://doi.org/10.1002/essoar.10506103.1

Schmid, S. M., Paterson, M. S., & Boland, J. N. (1980). High temperature flow and dynamic recrystallization in Carrara marble. *Tectonophysics*, *65*(3–4), 245–280. https://doi.org/10.1016/0040-1951(80)90077-3

Schuck, B., Schleicher, A. M., Janssen, C., Toy, V. G., & Dresen, G. (2020). Fault zone architecture of a large plate-bounding strike-slip fault: a case study from the Alpine Fault, New Zealand. *Solid Earth*, *11*(1), 95–124. https://doi.org/10.5194/se-11-95-2020

Sobolev, S. V., & Brown, M. (2019). Surface erosion events controlled the evolution of plate tectonics on Earth. *Nature*, *570*(7759), 52–57. https://doi.org/10.1038/s41586-019-1258-4

Sobolev, S. V., Sobolev, A. V., Kuzmin, D. V., Krivolutskaya, N. A., Petrunin, A. G., Arndt, N. T., … Vasiliev, Y. R. (2011). Linking mantle plumes, large igneous provinces and environmental catastrophes. *Nature*, *477*(7364), 312–316. https://doi.org/10.1038/nature10385

Solomatov, V. S. (1995). Scaling of temperature- and stress-dependent viscosity convection. *Physics of Fluids*, *7*, 266–274. https://doi.org/10.1063/1.868624

Tasaka, M., Zimmerman, M. E., & Kohlstedt, D. L. (2017). Rheological Weakening of Olivine + Orthopyroxene Aggregates Due to Phase Mixing: 1. Mechanical Behavior. *Journal of Geophysical Research: Solid Earth*, *122*(10), 7584–7596. https://doi.org/10.1002/2017JB014333

Torsvik, T. H., Rousse, S., Labails, C., & Smethurst, M. A. (2009). A new scheme for the opening of the South Atlantic Ocean and the dissection of an Aptian salt basin. *Geophysical Journal International*, *177*(3), 1315–1333. https://doi.org/10.1111/j.1365-246X.2009.04137.x

van Zelst, I., Crameri, F., Pusok, A. E., Glerum, A., Dannberg, J., & Thieulot, C. (2021). 101 Geodynamic modelling: How to design, carry out, and interpret numerical studies. *Solid Earth Discussions*. [preprint], https://doi.org/10.5194/se-2021-14

Selbstständigkeitserklärung

Hiermit erkläre ich, dass ich die vorliegende Arbeit selbstständig angefertigt, nicht anderweitig zu Prüfungszwecken vorgelegt und keine anderen als die angegebenen Hilfsmittel verwendet habe. Sämtliche wissentlich verwendeten Textausschnitte, Zitate oder Inhalte anderer Verfasser wurden ausdrücklich als solche gekennzeichnet.

Südwinsen, den 21.11.2021

Maximilian J. E. A. Richter